A Search for a Diffuse Flux of Astrophysical Muon Neutrinos With the IceCube Neutrino Observatory in the 40-String Configuration

by

Sean Grullon

A dissertation submitted in partial fulfillment of the

requirements for the degree of

Doctor of Philosophy

(Physics)

at the

University of Wisconsin – Madison

2010

A Search for a Diffuse Flux of Astrophysical Muon Neutrinos With the IceCube Neutrino Observatory in the 40-String Configuration

Sean Grullon

Under the supervision of Professor Albrecht Karle

At the University of Wisconsin – Madison

Neutrinos have long been important in particle physics and are now practical tools for astronomy. Neutrino Astrophysics is expected to help answer longstanding astrophysical problems such as the origin of cosmic rays and the nature of cosmic accelerators. The IceCube Neutrino Observatory is a 1 km^3 detector currently under construction at the South Pole and will help answer some of these fundamental questions. Searching for high energy neutrinos from unresolved astrophysical sources is one of the main analysis techniques used in the search for astrophysical neutrinos with IceCube. A hard energy spectrum of neutrinos from isotropically distributed astrophysical sources could contribute to form a detectable signal above the atmospheric neutrino background. Since astrophysical neutrinos are expected to have a harder energy spectrum than atmospheric neutrinos, a reliable method of estimating the energy of the neutrino-induced lepton is crucial. This analysis uses data from the IceCube detector collected in its half completed configuration between April 2008 and May 2009 to search for a diffuse flux of astrophysical muon neutrinos across the entire northern sky.

Albrecht Karle (Adviser)

Acknowledgements

The collaborative nature of the IceCube project has been the most enjoyable aspect of graduate school research. I would like to thank many of my colleagues whose contributions made this work possible.

I owe a debt of gratitude to my advisor, Albrecht Karle, for the opportunity to contribute to the IceCube experiment and for the subsequent intellectual freedom. I am especially grateful for his confidence and support in encouraging me to represent the collaboration at international conferences, to participate in the testing and deployment of the IceCube photosensors at the south pole, and to collaborate with scientists from other institutions.

I would like to offer my appreciation to Gary Hill, whose ideas and inspiration has made much of this analysis possible. Our collaboration has empowered me to think like a physicist. I would like to thank Francis Halzen for our inspirational physics conversations and equally inspirational discussions about food and wine. I would also like to thank Teresa Montaruli for both her feedback and inquisitive approach.

Many thanks to Dimitry Chirkin whose tireless efforts to measure the optical properties of the South Pole ice has made a proper assessment of this important source of systematic uncertainty possible. I am particularly grateful for his support in incorporating these new measurements to the simulation of IceCube data. I can not

give enough thanks and praise to David Boersma, who is largely responsible for my understanding of reconstruction. I'd also like to thank Tom Fuesels for carrying the Photorec reconstruction baton to a new generation.

I would like to recognize the efforts of my colleagues in the Diffuse cosmic and atmospheric neutrino working group. I am very thankful for Tom Gaisser's unwavering support of this work and his help in establishing a context for these results. Kotoyo Hoshina deserves special recognition for providing a starting point for this analysis with her work on the challenging 22-string data set. The dialogue with Warren Huelsnitz has proved very helpful since there is a great synergy between our work.

I want to express my appreciation for my fellow graduate students in Madison. I'd like to recognize my fellow collider physics refugees, Karen Andeen and Erik Strahler, for many years of banding together for both course work and graduate research. Jon Dumm's feedback and help with data filtering, ROOT data conversion, and distributed computing scripts have been a life saver.

I am grateful to Hagar Landsman for instructing me in DOM testing. These skills allowed me to travel to the South Pole to work on the IceCube detector. I owe many thanks to my colleagues at the South Pole, but especially to Jake Speed who helped me out of a real tight spot. I would also like to express my appreciation for the support staff of the IceCube Research Center, who all do a wonderful job of supporting this large research project.

Finally, I would like to offer my deepest gratitude to my family for their encouragement and support. My parents, Francisco José and Teresa, have always fostered an environment that empowered me to follow my life long interest in science.

Contents

List of Tables

List of Figures

Chapter 1

Introduction

Man has pondered the mysteries of the universe for thousands of years by looking to the sky. Guided by visible light from stars and other cosmic objects, mankind has learned much about the universe and our place in it. During the last century, new windows into the universe were opened using different wavelengths of light revealing new and unexpected phenomena. A common theme with many of these discoveries is that the universe is often ferocious and energetic. The universe is still filled with light from the primordial explosion of the Big Bang, matter collides and spirals around supermassive black holes at the center of galaxies, heavy stars explode in supernova, and even heavier stars explode and binary systems collide resulting in violent explosions known as gamma ray bursts.

Under such extreme conditions, scientists use the cosmos as a laboratory to investigate the fundamental laws of physics from a vantage point that is inaccessible to even the highest energy particle accelerators on Earth. These new windows to the universe have not only revolutionized astronomy, but also has opened up a new cosmic frontier of particle physics that help answer questions in fundamental physics while also revealing new mysteries. Among these are cosmic rays; high energy protons and

nuclei that are acelerated to energies far beyond what can be achieved by any particle accelerator on Earth. Cosmic rays bombard Earth continuously and their ultimate origin is a currently an unsolved problem in astrophysics.

Neutrinos deepen the connection between particle physics and astronomy. Anywhere nuclear reactions or high energy collisions take place, neutrinos are a fingerprint of such interactions. Neutrinos were produced in large numbers right after the Big Bang [3], in the cores of stars (fig. 1.2), when heavy stars explode in supernova [4], and other potential celestial objects. The new window to the universe provided by the neutrino has already revolutionized our understanding of fundamental physics and the sun. The discovery that neutrinos have mass solved a longstanding problem in astronomy where fewer neutrinos were observed from the sun than were predicted [5].

Wolfgang Pauli proposed the neutrino in 1933 [6] to solve a known problem where radioactive beta decay appeared to violate energy conservation. The observation of the neutrino proved elusive for 20 years until Clyde Cowan and Frederick Reines [7] first detected the anti-social particle coming from the Hanford and Savannah River nuclear reactors. Neutrinos, having no electric charge and interacting only via the weak interaction, are ideal cosmic messengers to study the high-energy universe since they enable physicists to observe environments inaccessible to optical telescopes. (See fig. 1.3.)

Neutrino astronomy is still new field. The only confirmed sources of extraterrestrial neutrinos are from the sun and Supernova SN 1987a. The main goal of the IceCube Neutrino Observatory is the detection of new sources of high energy astrophysical neutrinos. The goal of this work is the search for high energy extraterrestrial
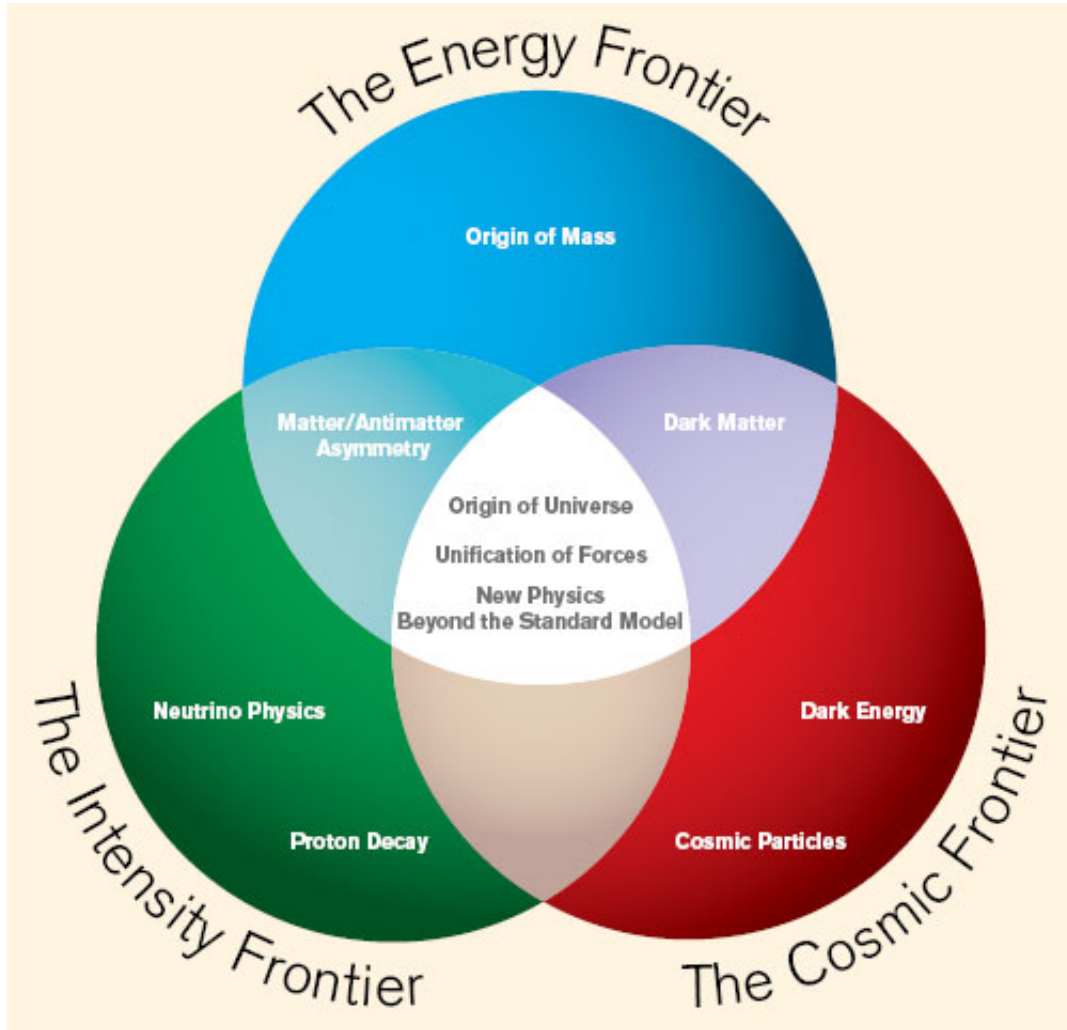
Figure 1.1: The three frontiers of particle physics. Research in fundamental physics progresses on three fronts: the energy frontier, the intensity frontier and the cosmic frontier. At the energy frontier, physicists build particle accelerators to collide particles at the highest possible energy in order to create new particles. Physicists at the intensity frontier use accelerators with intense beams and experiments with very large volumes to study processes that occur only rarely in nature. Physicists at the cosmic frontier take insight from the new windows to the universe provided by astronomers to explore physics inaccessible in a laboratory environment. Taken from [1].
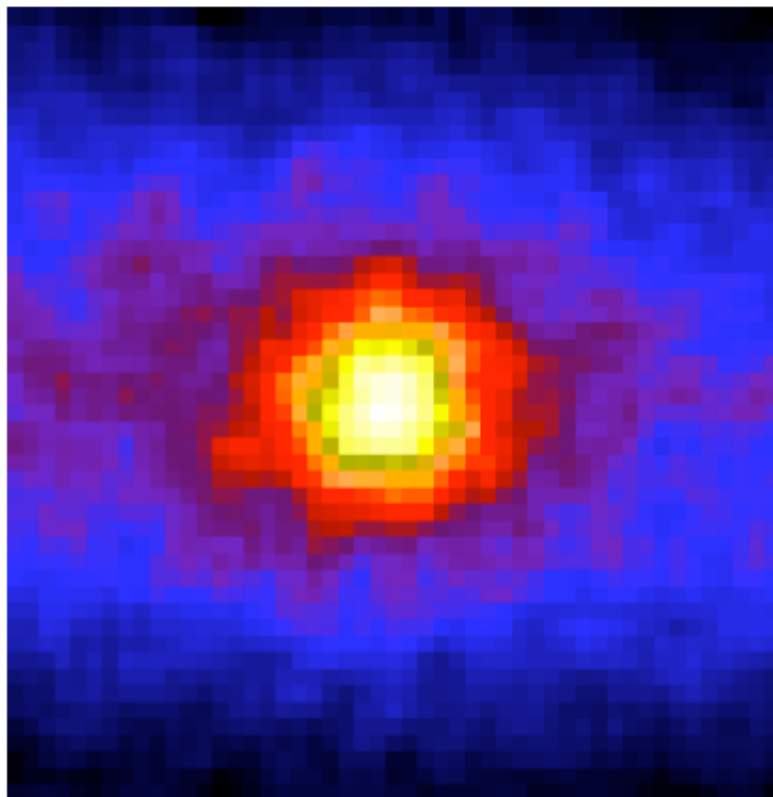
Figure 1.2: Image of the sun in neutrinos, taken by the Super-Kamiokande neutrino experiment [2]. Image Credit: R Svoboda and K. Gordan
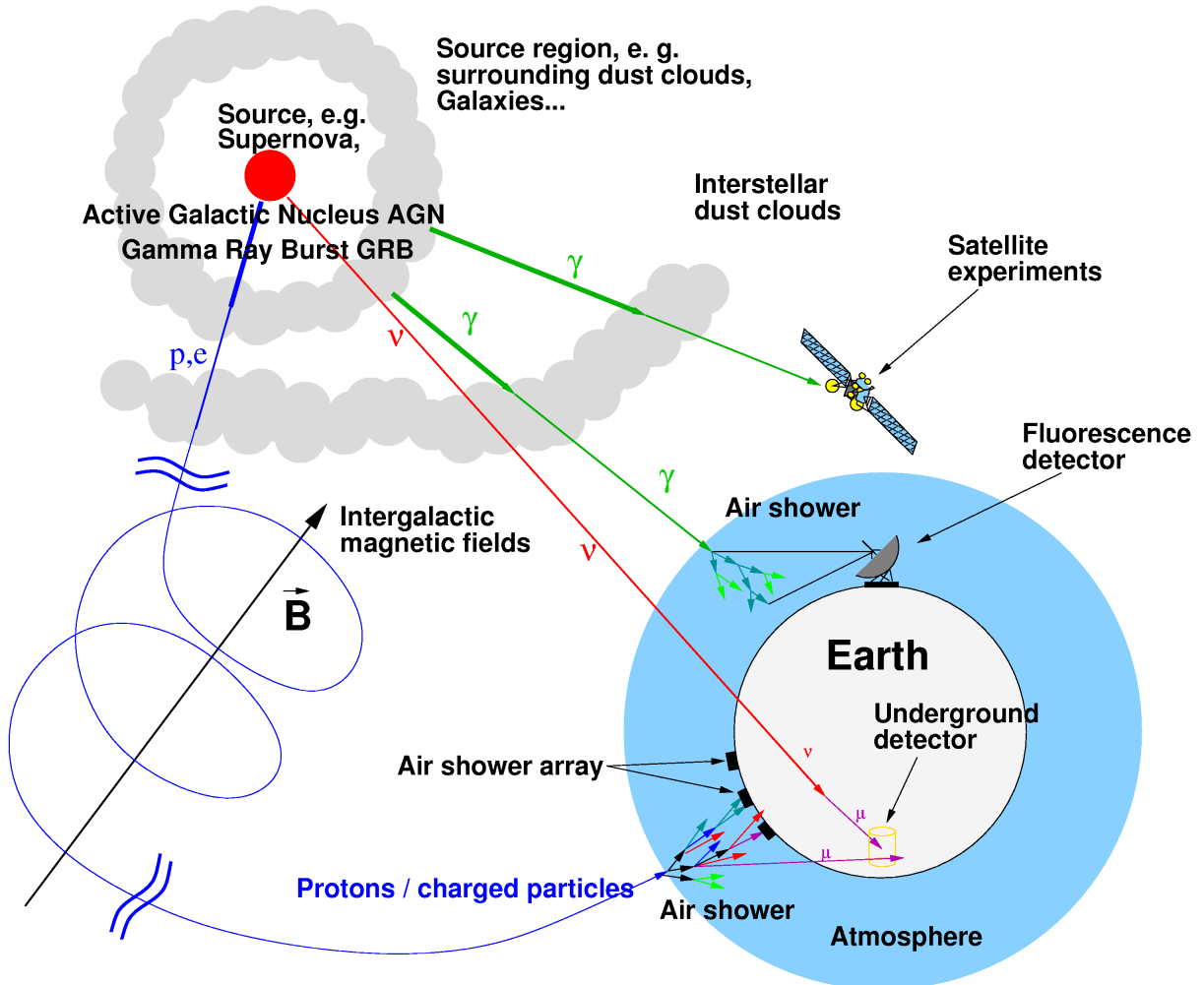
Figure 1.3: The neutrino's role in multi-messenger high energy astrophysics. Cosmic rays are charged and therefore lose their directional information by the time they arrive at Earth. Gamma-rays have a short horizon and easily absorbed by dust, the infrared background, and cosmic microwave background. Discrimination between the production mechanisms responsible for the gamma-rays is also difficult, since most gamma-ray sources are equally well described by electromagnetic or hadronic acceleration models. Neutrinos are uncharged and only interact via the weak interaction, making them ideal cosmic messengers for the high-energy universe. Image Credit: Wolfgang Rhode

neutrinos from unresolved astrophysical sources. The presence of such a diffuse flux of astrophysical neutrinos carries a lot of information about the distribution of cosmic accelerators in the universe, while the lack of such a signal enables us to set strong constraints on the distribution of such high energy sources.

Chapter 2

High Energy Neutrino Astrophysics

Although neutrino astronomy is still in its infancy, it has great potential to revolutionize our understanding of many astrophysical phenomena. It is in particular well positioned to elucidate the origin of the high energy cosmic rays whose ultimate origin remain a mystery since their discovery by Vector Hess's [8] balloon flights in 1912. We shall see that the production of high energy astrophysical neutrinos is closely linked to the acceleration of high energy cosmic rays in the universe.

2.1   Cosmic Rays

Cosmic rays are high energy charged particles traveling through the universe. The majority of cosmic rays (79% [9]) are protons while the other 21% of the cosmic ray composition consists of helium nuclei, (15%), electrons (2%), and elements heavier than helium (4%). Although the Large Hadron Collider at CERN will accelerate protons to a center of mass energy of 14 TeV, cosmic rays have been observed with energies as high as 10^{20} eV making them the highest energy particles ever observed. An important feature of the cosmic ray energy spectrum is that it follows a power law over many orders of magnitude in energy. This indicates that cosmic rays can not result

from thermal processes, but instead must come from non-thermal mechanisms which focus the energy outflow from a source onto a relatively small number of particles. The measured cosmic ray spectrum is shown in fig. 2.1, which shows the results of both direct measurements from satellite and balloon-based experiments and indirect measurements from air shower arrays.

The differential flux is $dN/dE \propto E^{-2.7}$ [9] over many decades in energy until a feature around 10^{15} eV known as "the knee" where the spectrum steepens to $dN/dE \propto E^{-3.2}$. The exact mechanism responsible for the knee has yet to be understood, but it has been hypothesized that a rigidity dependent cutoff [11] in the spectrum would be natural as cosmic rays diffuse out of the milky way galaxy at higher energies. The slope changes again with a feature called "the ankle" at $5 \times 10^{18} eV$ where the spectrum hardens back to $dN/dE \propto E^{-2.7}$. The cosmic ray spectrum gets suppressed above $5 \times 10^{19} eV$ [12] by the Greizen-Zatsepin-Kuzmin (GZK) mechanism, where cosmic ray protons are above the energy threshold to interact with the cosmic microwave background photons to produce pions.

For energies below the knee, shock waves produced by supernova remnants in the milky way galaxy [13] provide natural non-thermal candidates to accelerate cosmic rays. As the cosmic ray spectrum transitions from galactic to extra-galactic in origin at higher energies above the knee, larger acceleration sites and stronger magnetic fields are necessary to explain the observed energies. Natural extragalactic source candidates include active galactic nuclei and gamma ray bursts.
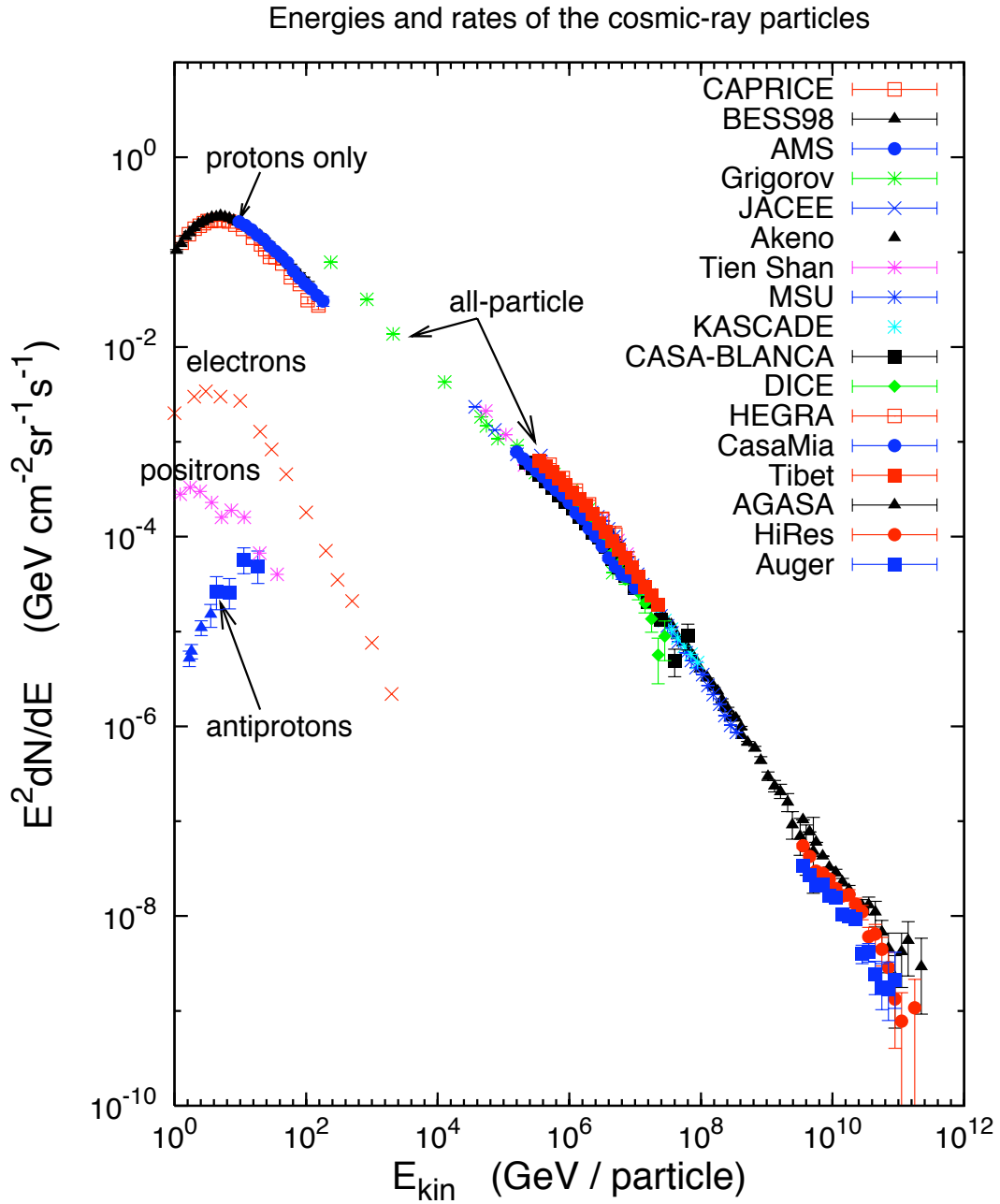
Figure 2.1: The cosmic ray energy spectrum as measured from different experiments. The cosmic ray flux has been multiplied by E^2 to enhance features. Taken from [10].

2.2 Astrophysical Neutrino Production

Active galactic nuclei (AGN), gamma ray bursts (GRBs), and supernova remnants (SNR) are among the leading candidate astronomical objects that could accelerate cosmic rays to high energies and produce neutrinos. As mentioned in the last section, the power law nature of the cosmic ray spectrum indicates a non-thermal mechanism is responsible for their acceleration. A widely held non-thermal acceleration mechanism due to magnetic shocks is first order Fermi acceleration [14]. Charged particles are confined to the shock region by magnetic inhomogeneities and are therefore continuously accelerated by repeated magnetic deflection through the shock front. First order Fermi acceleration predicts a primary cosmic ray spectrum of:

$$\frac{dN}{dE} \propto E^{-2} \tag{2.1}$$

With high densities of matter and radiation at the source, the accelerated cosmic ray primaries may interact and not escape. Neutrinos are produced from the hadronic nucleon-photon and nucleon-nucleon interactions in the astrophysical shock fronts which result in the production of pions. Pion production occurs via the delta resonance for nucleon-photon interactions and the dominant channels are:

$$p\gamma \rightarrow \Delta^+$$
$$\Delta^+ \rightarrow p + \pi^0 \tag{2.2}$$
$$\Delta^+ \rightarrow n + \pi^+$$

$$n\gamma \to \Delta^0$$

$$\Delta^0 \to n + \pi^0 \tag{2.3}$$

$$\Delta^0 \to p + \pi^-$$

The dominant pion-production channels for nucleon-nucleon scattering are:

$$pp \to p + p + \pi^0$$

$$p + n + \pi^+$$

$$pn \to p + n + \pi^0 \tag{2.4}$$

$$p + p + \pi^-$$
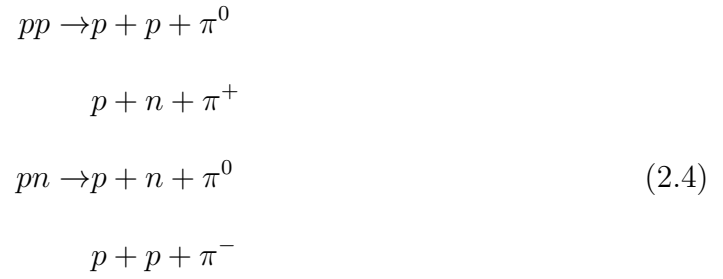
It can be seen that half of the pions produced are charged where as the other half are neutral. The charged pions decay to produce neutrinos and the neutral pions decay into gamma rays:

$$\pi^+ \to \mu^+ + \nu_\mu \tag{2.5}$$

$$\mu^+ \to e^+ + \nu_e + \bar{\nu}_\mu$$
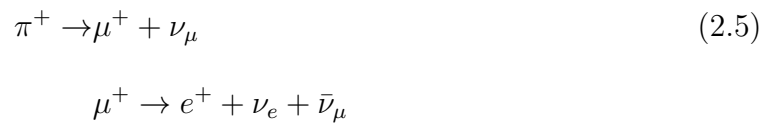
$$\pi^- \rightarrow \mu^- + \bar{\nu}_\mu \tag{2.6}$$

$$\mu^- \rightarrow e^- + \bar{\nu}_e + \nu_\mu$$

$$\pi^0 \rightarrow \gamma\gamma \tag{2.7}$$

At higher energies, kaons can also be produced [15] and contribute to the neutrino and gamma ray flux. The resulting neutrinos and gamma rays follow the energy spectrum of the primary cosmic rays. Astrophysical neutrinos and gamma rays from hadronic interactions are therefore predicted to have a $dN/dE \propto E^{-2}$ energy spectrum. The neutrino flux at the source has a flavor ratio of

$$\nu_e : \nu_\mu : \nu_\tau = 1 : 2 : 0 \tag{2.8}$$

Neutrinos have a small but non-zero mass, which causes them to oscillate and change flavors. The expected flavor ratio of astrophysical neutrinos at Earth is [16]:

$$\nu_e : \nu_\mu : \nu_\tau = 1 : 1 : 1 \tag{2.9}$$

Although the particle physics responsible for the production of neutrinos and gamma rays is well known, the underlying astrophysical details are poorly understood. We consider several models for astrophysical neutrinos in the next section.

2.3 Astrophysical Neutrino Models

Neutrino astrophysics is a young field. With the underlying astrophysics responsible for the hadronic acceleration of cosmic rays being so uncertain, a wide range of

models have been developed to calculate the neutrino flux from different astrophysical source classes. These models generally use a particular waveband (radio, cosmic rays, gamma rays) to determine the normalization of the neutrino flux. This work searches for an isotropic distribution of astrophysical muon neutrinos from unresolved sources. The models considered in this analysis calculate the total sum of astrophysical neutrinos from different extragalactic source classes that contribute to a diffuse ν_μ flux. These models are shown in fig. 2.2 and are described in this section.
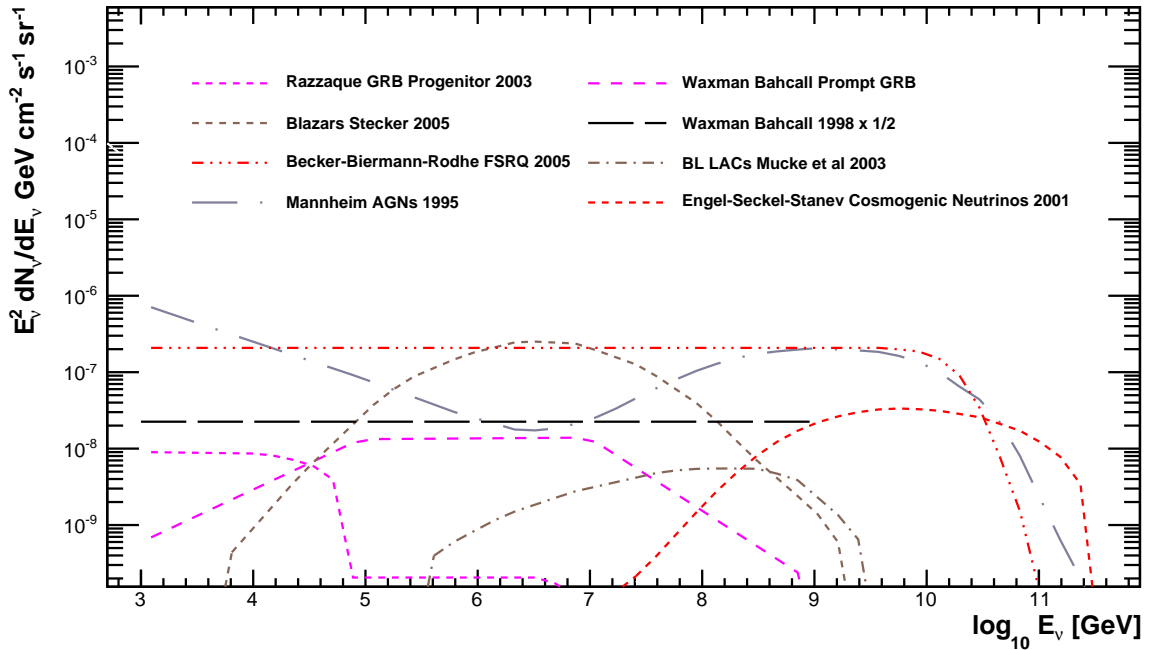
Figure 2.2: Diffuse astrophysical neutrino model predictions for different extraterrestrial source classes. The models for active galactic nuclei include predictions from Stecker [17], Mücke *et al.* [18], Becker-Biermann-Rodhe [19], and Mannheim [20]. The two models for gamma ray bursts shown are described by Razzaque and Meszaros in [21]. An upper bound on astrophysical neutrinos is calculated by Waxman and Bahcall in [22]. Finally, neutrinos produced by the GZK suppression of the cosmic ray flux is calculated by Engel, Seckel, and Stanev [23].

2.3.1 Waxman-Bahcall Upper Bound

The Waxman-Bahcall upper bound [22] assumes that the extragalactic cosmic ray flux has a $\Phi \propto E^{-2}$ spectrum. Consistent with the observed cosmic ray spectrum, an energy production rate for protons was assumed to be

$$E_{CR}^2 \frac{d\dot{N}_{CR}}{dE_{CR}} = 10^{44} \text{ erg Mpc}^{-3} \text{ yr}^{-1} \tag{2.10}$$

An upper bound on the astrophysical neutrino flux was derived for optically thin sources. Since half of the produced pions are charged and half the energy of the charged pions goes into the muon neutrinos, the upper bound on the diffuse astrophysical neutrino flux is given by

$$E_\nu^2 \frac{dN_\nu}{dE_\nu} = 0.25 \, t_h \times E_{CR}^2 \frac{d\dot{N}_{CR}}{dE_{CR}} \tag{2.11}$$

The Hubble time, $t_h = 10^{10}$ years, is given by the inverse of the Hubble constant which was assumed to be $H = 65 \, km \, s^{-1} \, Mpc^{-1}$ in the calculation. The upper bound on the flux was calculated to be $1.5 \times 10^{-8} \, GeV \, cm^{-2} \, s^{-1} \, sr^{-1}$. After correcting for redshift evolution and neutrino oscillations, the upper bound for muon neutrinos at Earth is $2.25 \times 10^{-8} \, GeV \, cm^{-2} \, s^{-1} \, sr^{-1}$.

2.3.2 Becker, Biermann, and Rhode Radio Galaxy Model

Becker, Biermann, and Rhode [19] calculated the diffuse astrophysical neutrino flux from active galactic nuclei using observations from FR-II radio galaxies. The jet of the AGN is a candidate site for $p + \gamma$ interactions and subsequent photo-pion production. The observations from FR-II radio galaxies was used to normalize the flux

of neutrinos by assuming a relationship between the disk luminosity, the luminosity in the observed radio band, and the calculated neutrino flux. $\Phi \propto E^{-2}$ was assumed for the proton energy spectrum in the model considered in this work.

2.3.3   Astrophysical Neutrinos from Blazars

For optically thick sources, TeV gamma rays that are produced from the decay of neutral pions cascade to lower energies resulting in the emission of sub-TeV photons. The observed diffuse extragalactic gamma ray flux from the experiments in the Compton Gamma Ray Observatory satellite can therefore be interpreted as hadronic gamma-rays avalanched to lower energies. The neutrino flux can therefore be normalized to the diffuse extragalactic gamma-ray background detected by the EGRET and COMPTEL experiments that were onboard the Compton Gamma Ray Observatory. These two experiments were sensitive in different energy ranges, with EGRET detecting a diffuse extragalactic gamma-ray flux at higher energies ($E_\gamma > 100$ MeV) and COMPTEL measuring the diffuse component at lower energies ($E_\gamma < 100$ MeV). A model of $p + \gamma$ interactions and $p + p$ collisions at the core of AGNs is derived by Mannheim [20] which uses the EGRET diffuse observation to normalize the neutrino flux calculation. The model calculated by Stecker [17] uses the results from COMPTEL to normalize the neutrino flux resulting from pp and $p\gamma$ interactions at the core of the blazar.

2.3.4   High-Frequency Peaked BL-LACs Model

BL-LACs that are observed to emit TeV gamma rays can be interpreted to be optically thin to photon-neutron interactions. The model calculated by Mücke *et*

al. [18] assumes that charged cosmic rays are produced in these sources through the decay of escaping neutrons. The resulting neutrino flux would be proportional to the observed extra-galactic cosmic ray flux at Earth. The calculation of the neutrino flux connects the observed cosmic ray flux to TeV emission from high frequency peaked BL-LACs. The flux is calculated to be quite small and peaks at high energies (10^8 GeV).

2.3.5   Neutrinos from Gamma-Ray Bursts

Gamma-Ray Bursts are the highest energy explosions known in the universe with energies greater than 10^{50} erg over an extremely short time scale of $10^{-3}s - 1000$ s. They are a prime candidates to accelerate the highest energy cosmic rays. The non-thermal emission occurs in three stages: the precursor phase hours before the GRB, the prompt phase coincident with the burst, and the afterglow phase. Although there is a wide variation in gamma-ray burst emission profiles, an average spectrum of neutrinos from the precursor and prompt phases of GRBs is calculated in [21] by correlating the gamma-ray emission to the observed flux of ultra high energy cosmic rays.

2.3.6   Cosmogenic Neutrinos

The observation of the GZK suppression in the cosmic ray flux above the ankle implies the existence of a high energy astrophysical neutrino flux. It is called one of the guaranteed sources of neutrinos induced by the cosmic ray flux, with the other two being neutrinos produced by the propagation of cosmic rays through plane of the milky way galaxy and atmospheric neutrinos which are described in the next chapter. The cosmogenic neutrino flux, which has yet to be observed, originates from the GZK mechanism of photo-pion production by protons interacting with the cosmic microwave

background. A calculation of the cosmogenic flux is done by Engel, Seckel, and Stanev in [23].

2.3.7 Other Sources of High Energy Astrophysical Neutrinos

Not considered in this work are other sources of high energy astrophysical neutrinos. Among these models are neutrinos from the decay of exotic relic particles [24] and neutrinos from the annihilation of neutralino dark matter [25].

Chapter 3

Atmospheric Neutrinos

3.1 Neutrino Production in Extensive Air Showers

The primary background in a search for high energy astrophysical neutrinos is the atmospheric neutrino and muon background produced in the Earth's atmosphere. High energy cosmic rays interact with air molecules in the Earth's atmosphere which results in a cascade of particle production and decay. This chain leads to an extensive air shower of electrons, positrons, pions, kaons, muons, and neutrinos. In quite an analogous manner to the astrophysical production of neutrinos discussed in the last chapter, atmospheric neutrinos are produced through the hadronic interactions of cosmic ray primaries with the atmosphere generating charged pions and kaons, which subsequently decay into muons and muon neutrinos:

$$\pi^+ \left(K^+\right) \rightarrow \mu^+ + \nu_\mu$$
$$\pi^- \left(K^-\right) \rightarrow \mu^- + \bar{\nu}_\mu$$

(3.1)

$$\pi^- \to \mu^- + \bar{\nu}_\mu$$

$$\mu^- \to e^- + \bar{\nu}_e + \nu_\mu$$

Cosmic
ray

$$\pi^+ \to \mu^+ + \nu_\mu$$

$$\mu^+ \to e^+ + \nu_e + \bar{\nu}_\mu$$

π^-

μ^-

e^-

$\bar{\nu}_\mu$

$\bar{\nu}_e$

ν_μ

π^0

γ γ

π^+

Decay

e^+ e^-

γ γ

μ^+

Hadronic
shower

Electromagnetic
shower

Decay

e^+

ν_μ

ν_e

$\bar{\nu}_\mu$
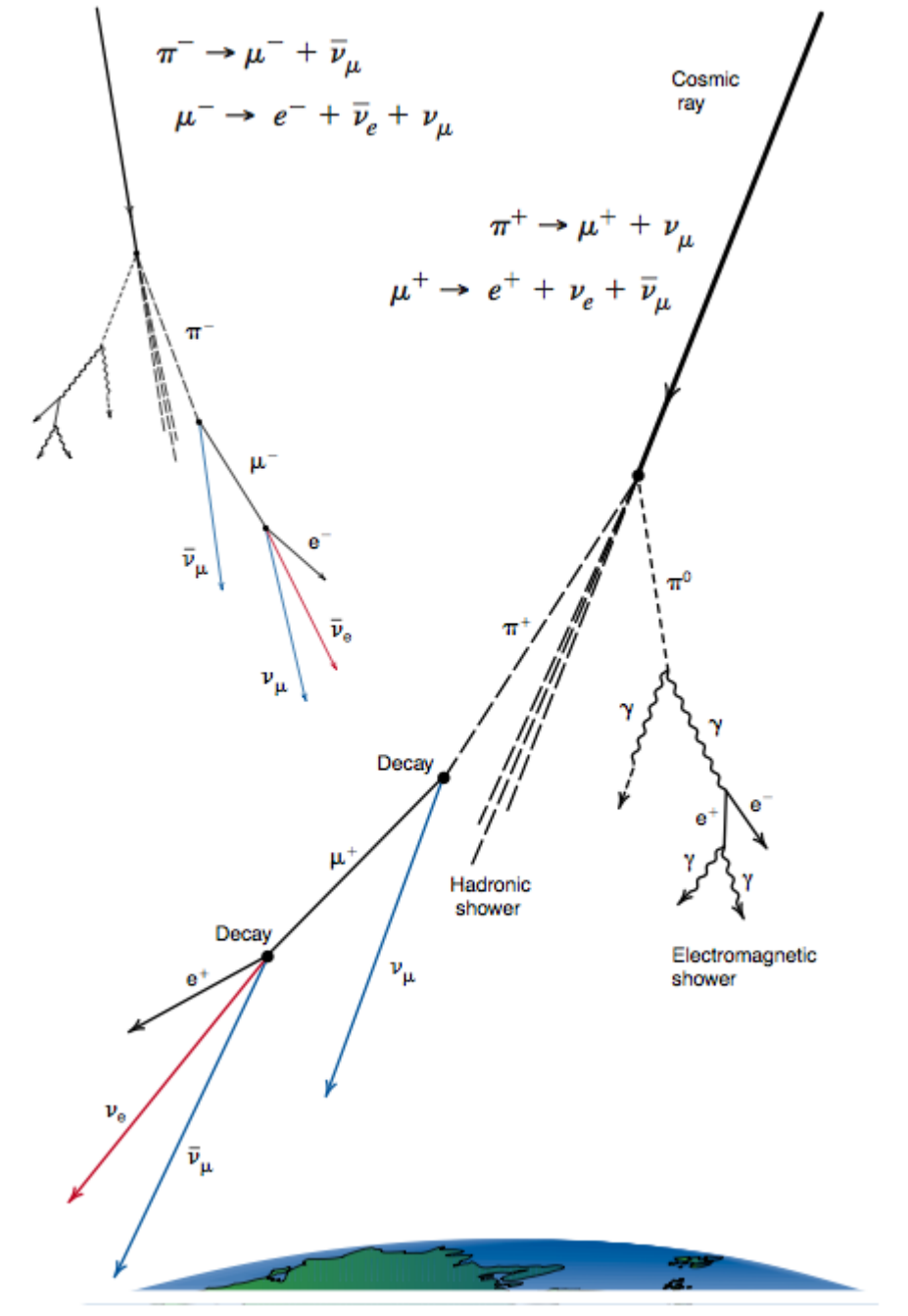
Figure 3.1: An extensive air shower leading to the production of atmospheric muons and neutrinos. Taken from [26]

An example of an extensive air shower is shown schematically in fig. 3.1. Some of the muons produced in the shower would decay producing both electron and muon neutrinos according to eq. 2.5 and eq. 2.6. The atmospheric neutrino flux due to the decay of pions and kaons are commonly referred to as the *conventional* atmospheric neutrino flux.

While the flux of the parent cosmic ray primaries is isotropic, the conventional atmospheric neutrino flux has a complicated zenith angle dependence due to the kinematics of meson interaction and decay in the atmosphere. The kinematics of meson interaction and decay also affects the energy spectrum of the atmospheric neutrino flux. An important parameter is the critical energy E_{crit} which is defined as the energy where the decay length and the interaction length are equal and is defined as:

$$E_{crit} = \frac{mc^2}{c\tau}h_0 \tag{3.2}$$

Table 3.1: Critical energies for various particles. Data from [27].

Particle	Constituent Quarks	mc^2 (GeV)	E_{crit} (GeV)
$\mu^\pm$	lepton	0.106	1.0
π^+, π^-	$u\bar{d}, \bar{u}d$	0.140	115
K^+, K^-	$u\bar{s}, \bar{u}s$	1.116	850

were τ is the live-time of the particle and h_0 comes from the assumption of an isothermal atmosphere [28]. A lepton or a meson with energies above the critical energy will more likely interact than decay. Table 3.1 summarizes the critical energies of the particle types that contribute to the conventional atmospheric neutrino flux. We note that the muon has a critical energy of 1.0 GeV, which is well below the energy threshold of the IceCube Neutrino Observatory and the sensitivity of this work.

Since the ν_e component of the conventional atmospheric neutrino flux arises from the decay of atmospheric muons, the atmospheric electron neutrino flux is an order of magnitude smaller than the ν_μ flux in the $GeV - TeV$ energy range [29]. For energies below E_{crit}, the atmospheric neutrino spectrum follows the primary cosmic ray energy spectrum. Above the critical energy, the energy spectrum of neutrinos decreases by one additional power of the energy [29]. Detailed three-dimensional calculations of the energy spectrum and angular distribution of the conventional atmospheric neutrino flux are summarized in [30] and [31].

3.2   Prompt Atmospheric Neutrinos

Table 3.2: Summary of Charm Particles. Data from [27].

Particle	Constituent Quarks	mc^2 (GeV)	E_{crit} (GeV)
D^+, D^-	$c\bar{d}, \bar{c}d$	1.87	3.8×10^7
$D^0, \bar{D}^0$	$c\bar{u}, \bar{c}u$	1.865	9.6×10^7
D_s^+, D_s^-	$c\bar{s}, \bar{c}s$	1.969	8.5×10^7
Λ_c^+	udc	2.285	2.4×10^8

If the energy of the primary cosmic ray is high enough, the extensive air shower will include the production and decay of charm baryons and mesons. Charm particles typically have very short live-times, so the atmospheric neutrino flux arising from the decay of charmed mesons is often called the *prompt* component of the atmospheric neutrino flux. The charm particles thought to be produced in extensive air showers are summarized in Table 3.2. The dominant contribution to the prompt flux is the semi-leptonic decay modes of D mesons decaying to Kaons and leptons:

$$D \rightarrow K + l + \nu_l \tag{3.3}$$

The most common semi-leptonic decay channels are from $D^\pm$ which have a branching ratio of 17.2% [32]:

$$D^+ \to \bar{K}^0 + \mu^+ + \nu_\mu \tag{3.4}$$
$$D^- \to K^0 + \mu^- + \bar{\nu}_\mu$$

$$D^+ \to \bar{K}^0 + e^+ + \nu_e \tag{3.5}$$
$$D^- \to K^0 + e^- + \bar{\nu}_e$$

Since the critical energies (Table 3.2) of charm particles are so high, they will decay before interacting and subsequently follow the primary cosmic ray energy spectrum and have an isotropic angular distribution. We note that the prompt component of the atmospheric neutrino flux has an equal contribution from ν_μ and ν_e. Full calculations of the prompt component of the atmospheric neutrino flux are given in [33], [34], and [35].

3.3   A Comment on Neutrino Oscillations

If neutrinos have a nonzero mass, their mass eigenstates do not correspond to the flavor eigenstates. This implies that neutrinos can change flavor as they propagate. A ν_μ produced in the atmosphere may appear in the detector as another flavor. For the case of two-flavor oscillations (ν_μ and ν_τ), the survival probability of a muon neutrino

in the atmosphere for the two-flavor oscillation case is [27]:

$$P_{\nu_\mu \to \nu_\mu} = 1 - \sin^2(2\theta_{atm}) \sin^2\left(\frac{\Delta m_{atm}^2 L}{4E}\right) \tag{3.6}$$

where Δm_{atm}^2 is the squared mass difference between the two mass eigenstates and the baseline L is in natural units of GeV^{-1}. For energies above 50 GeV, atmospheric neutrino oscillations cease for baselines equal to the diameter of the Earth. Atmospheric neutrino oscillations are therefore unimportant for the majority of analyses done with the IceCube Neutrino Observatory and this work in particular.

Chapter 4

Principles of Neutrino Detection

The small interaction cross section of the neutrino presented a major challenge to understanding their properties and to the development of neutrino astrophysics. Neutrino detectors in general and neutrino telescopes in particular must encompass an enormous volume to compensate for such low interaction cross sections. The design of a high energy neutrino telescope involves the use of natural bodies of water or transparent ice as target material and a detection medium for neutrinos to interact in. The medium is instrumented with photomultiplier tubes to detect the products of the neutrino interaction occurring in or near the instrumented detector volume.

4.1   Neutrino-Nucleon Interactions

Neutrinos only interact via the weak interaction. They interact via charged-current (CC) interactions which are mediated by $W^{\pm}$ bosons or neutral current (NC) interactions which are mediated by Z^0 bosons. The Feynman diagrams depicting these interactions are summarized in fig. 4.1. A charged-current interaction of a neutrino with nucleus in the ice produces a charged lepton:
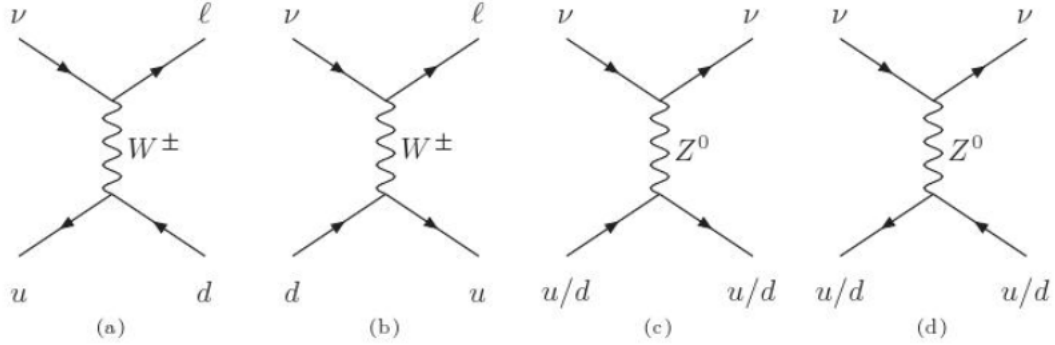
Figure 4.1: Feynman diagrams for neutrino-quark Charged Current and Neutral Current interactions

$$\nu_l + q \rightarrow l + q' \tag{4.1}$$

where q is a valence or sea quark in the nucleus and q' is a quark of a different flavor. (The flavor of the quark is changed by the exchange of a W boson.) As an example, a muon neutrino that undergoes a charged-current interaction with one of the ice nuclei would result in a muon.

The deep-inelastic scattering cross sections are the most important for the energy range relevant to an astrophysical neutrino observatory. The neutrino in the *deep-inelastic regime* has enough energy to interact with the quarks or gluons as point particles. The neutrino transfers enough energy to the parton (a quark or gluon constituent of the nucleon) such that the interaction dissociates the parent nucleon. The NC and CC neutrino-nucleon deep inelastic cross sections in ice are summarized in fig. 4.2.
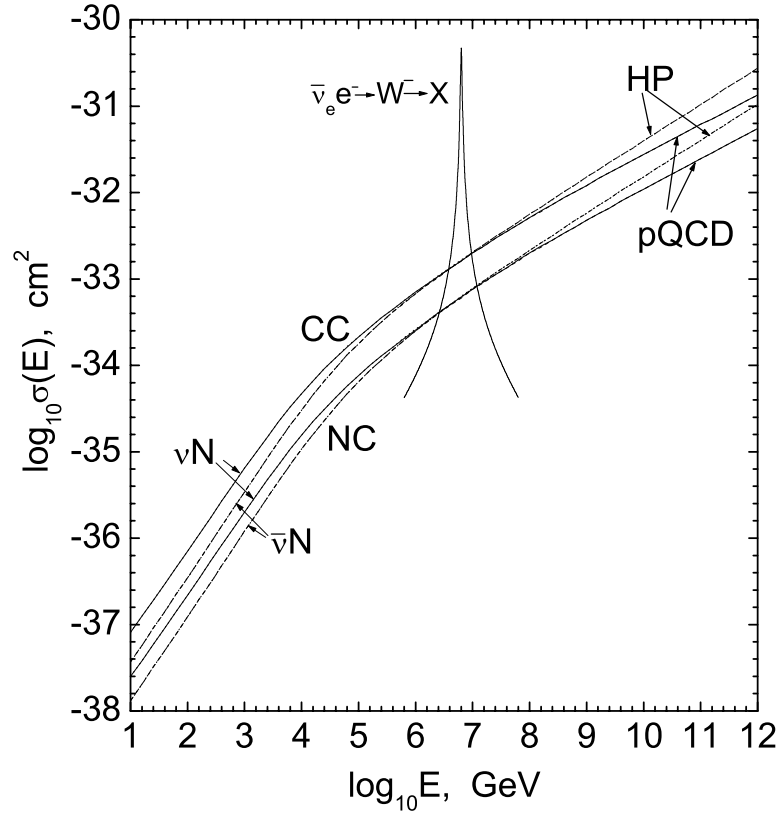
Figure 4.2: Charged Current and Neutral Current cross sections for neutrino-nucleon deep inelastic scattering. From [36], which uses the Parton Distribution Functions parametrized in CTEQ5. [37]
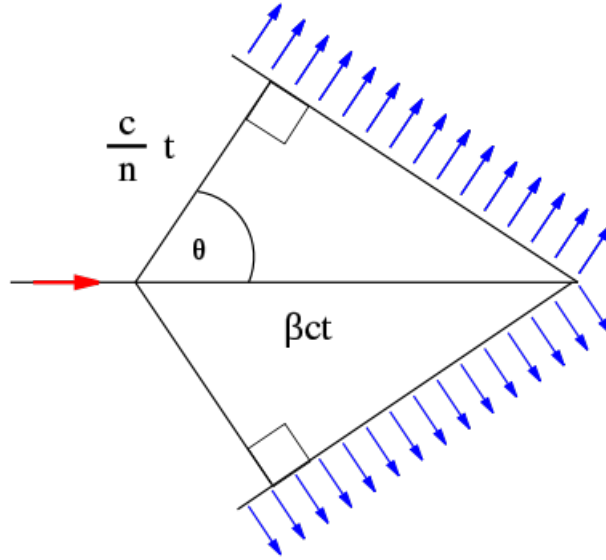
Figure 4.3: Čerenkov cone geometry formed by a relativistic muon traveling through a medium

4.2   Čerenkov Radiation

Neutrinos can not be seen directly in a detector since they only interact via the weak interaction. A relativistic muon from a charged-current neutrino-nucleon interaction radiates light via the Čerenkov effect if the muon travels faster than the speed of light in the medium. The detection of Čerenkov radiation in a transparent medium arising from neutrino interactions is the primary operating principle of a neutrino telescope. A coherent front of light analogous to a shock wave forms at a characteristic angle θ_c which depends on the index of refraction of the medium:

$$\cos\theta_c = \frac{1}{n\beta} \tag{4.2}$$

where $\beta = v/c$ is the velocity of the particle. The geometry of the Čerenkov cone is depicted in fig. 4.3. The Čerenkov angle for ice is $\theta_{c,ice} \approx 41°$ for relativistic

particles ($\beta \approx 1$) and an index of refraction $n_{ice} \approx 1.33$.

The number of Čerenkov photons emitted per unit track length as a function of wavelength of light λ is given by the Frank-Tamm formula [27]:

$$\frac{d^2 N}{dx d\lambda} = \frac{2\pi\alpha}{\lambda^2} \left(1 - \frac{1}{\beta^2 n^2} \right) \qquad (4.3)$$

where α is the fine structure constant. High frequency radiation dominates the Čerenkov emission due to the $1/\lambda^2$ dependence of the Frank-Tamm formula. A cutoff at the ultraviolet end of the spectrum is imposed (300 nm [38]) due to the absorption of light by the glass of the photomultiplier-tube.

4.3   Muon Energy Loss

It is of critical importance to understand the physical processes involved in muon propagation and energy loss since all information about the atmospheric ν_μ flux and a potential astrophysical ν_μ flux is inferred from the secondary muons. Muons do not lose much energy via Čerenkov radiation, which is estimated to be 24 keV/cm for $E_\mu > 1$ GeV [40]. The muon energy loss rate as a function of distance, dE/dX, is commonly expressed [27] as:

$$\frac{dE}{dX} = a\left(E\right) + b\left(E\right) E \qquad (4.4)$$

Where $a(E)$ corresponds to continuous muon energy loss mechanisms and $b(E)$ corresponds to the sum of stochastic energy losses. An assumption is often made that a and b are constant such that one can use the relation
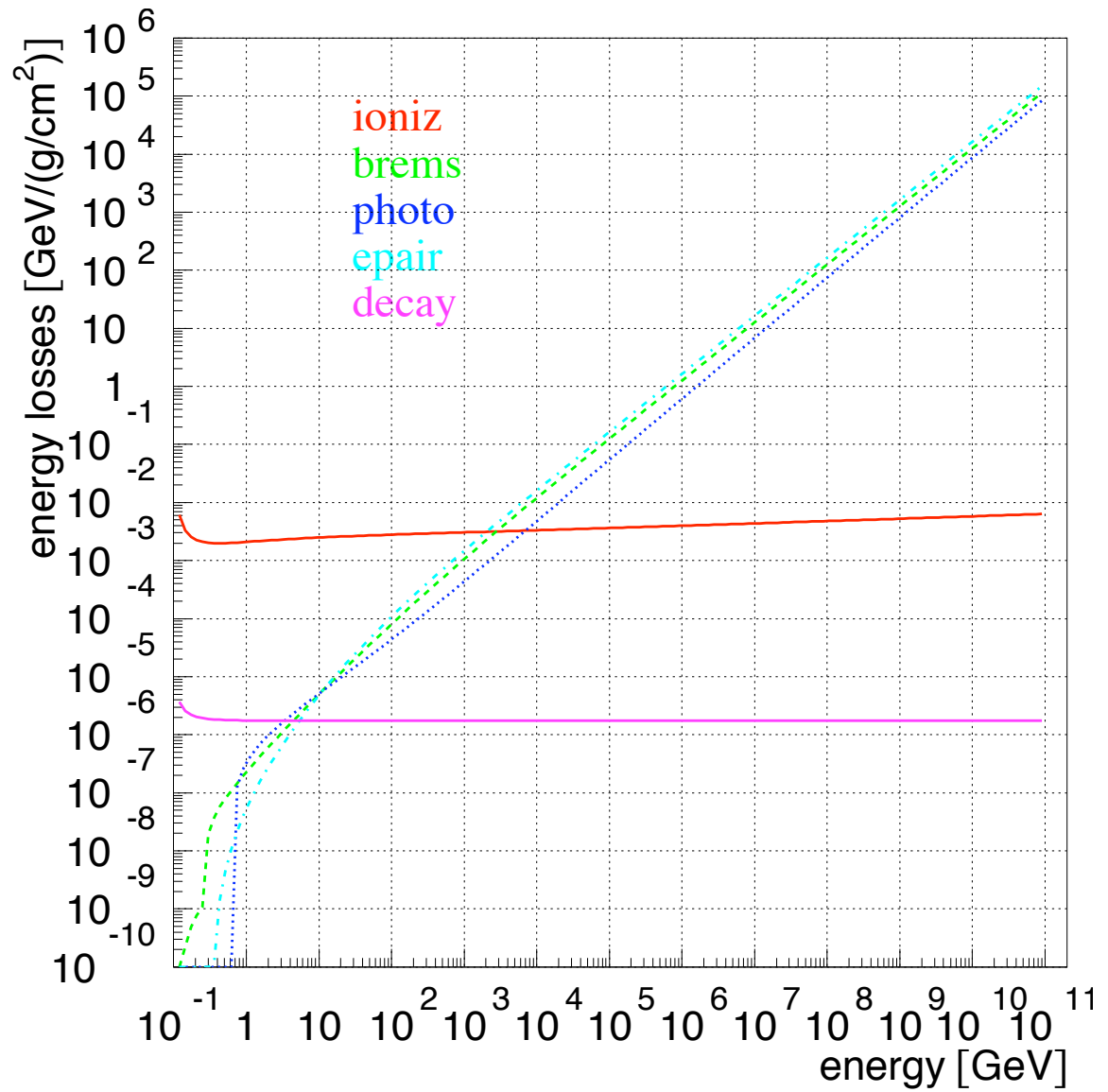
Figure 4.4: Average muon energy loss in ice as a function of the energy of the muon. From [39]

$$\frac{dE}{dX} \approx a + bE \tag{4.5}$$

to make an estimate of the energy loss for high energy muons. In ice:

$$a = 0.25958 \text{ GeV/mwe} \tag{4.6}$$

$$b = 3.5709 \times 10^{-4} \text{ GeV/mwe}$$

with a systematic error of 3.7% [?]. An example of such a calculation is an estimate of the muon range. The mean range R of a muon with initial energy E_0 is given by integrating eq. 4.5:

$$R \approx (1/b) \ln \left(1 + \frac{E_0}{E_{crit}} \right) \tag{4.7}$$

Where $E_{crit} = a/b$ is an estimate of the critical energy where continuous and stochastic energy losses are equal. In ice, $E_{crit} \approx 727$ GeV. A 1 TeV muon for example would have a mean range in ice of $R \approx 2.6$ km. This illustrates that a muon can have a range larger than the instrumented volume of a neutrino telescope, so a CC ν_μ interaction does not need to be contained within the fiducial volume of the detector.

The continuous and stochastic energy losses of the muon come from different physical processes. Continuous energy losses come from ionization and stochastic energy loss mechanisms come from e^+e^- pair production, bremsstrahlung, and photonuclear interactions. The energy losses from these various components are shown in fig. 4.4.

Stochastic muon energy losses in ice come in the form of relativistic electromagnetic and hadronic showers which also produce visible light due to Čerenkov radiation. The total light output of a stochastic shower can be estimated from the muon track length subtended by the constituent particles of the shower. This effective track length has been parameterized with shower energy in ice by C. Wiebusch [41]:

$$l_{eff}(E) = 0.894 \left(E_{(GeV)} \cdot 4.889 \right) \text{ For EM showers} \tag{4.8}$$

$$l_{eff}(E) = 0.860 \left(E_{(GeV)} \cdot 4.076 \right) \text{ For Hadronic Showers}$$

The amount of Čerenkov light emitted by a stochastic shower is then calculated by:

$$N_{\mu,S} = l_{eff}(E) \times n_C \tag{4.9}$$

where $l_{eff}(E)$ is given by eq. 4.8 and n_C is obtained by integrating the Frank-Tamm formula (eq. 4.3) over the sensitivity range of the photomultiplier tube.

Chapter 5

The IceCube Neutrino Observatory

The IceCube Neutrino Observatory is the largest neutrino detector built to date. When construction is completed in 2011, it will encompass a cubic-kilometer of instrumented Antarctic ice. The large instrumented volume is necessary because of the low neutrino interaction cross sections and the low predicted flux rates for astrophysical neutrinos. The IceCube detector is specifically designed to be a large tracking calorimeter, measuring energy deposition in the form of Čerenkov light contained within the instrumented volume.

Neutrino detection in the Antarctic ice was pioneered by AMANDA[42], the prototype and proof-of-principle for the IceCube detector. Operational from 1996 to 2009, the AMANDA array consisted of 677 optical modules deployed on 19 strings at a depth between 1900 m and 2000 m. IceCube will be over two orders of magnitude larger than its predecessor and will use improved electronics.

The IceCube design consists of three detectors operating in union, see fig. 5.1. The main in-ice array will be composed of 4800 photosensors arranged in 80 strings which are deployed vertically with 60 photosensors per string. The detector is deployed deep in the Antarctic ice between a depth of 1450 and 2450 meters. Each photosensor

IceCube Lab

IceTop
80 Stations, each with
    2 IceTop Cherenkov detector tanks
    2 optical sensors per tank
320 optical sensors

50 m

2010: 79 strings in operation
2011: Project completion, 86 strings

IceCube Array
86 strings including 6 DeepCore strings
    60 optical sensors on each string
    5160 optical sensors

1450 m

DeepCore
6 strings-spacing optimized for lower energies
360 optical sensors

Eiffel Tower
324 m

2450 m
2820 m

Bedrock

Figure 5.1: The IceCube Neutrino Observatory

is vertically spaced 17 m from its neighbor and each string of photosensors has a horizontal spacing of 125 m giving a total instrumented volume of 1 km^3. The design is optimized for the energy range of 100 GeV to 100 PeV [38] and for the event reconstructions discussed in chap. 8.

The DeepCore extension is deployed within the main in-ice array and consists of six specialized strings of photosensors with increased quantum efficiency in order to lower the energy reach to 10 GeV. Each DeepCore string also has 60 photosensors, but the extension is more densely spaced than the main in-ice array with a horizontal spacing of 72 m. Ten of the photosensors are deployed at shallow depths between 1750 m and 1850 m with a 10 m vertical spacing and the other 50 sensors are deployed with a 7 m vertical spacing at a depth below 2100 m where the Antarctic ice is the clearest. This extends the number of strings in the main in-ice array to 86 giving a total of 5160 photosensors. The physics goals of DeepCore include indirect dark matter searches and atmospheric neutrino oscillations studies [43].

The IceTop surface array [44] is an extensive air shower detector instrumenting a 1 km^2 area at the surface of the South Pole directly above IceCube. It will consist of 160 tanks deployed in pairs with two photosensors per tank. The primary physics goals of IceTop include measurements of the cosmic ray energy spectrum & mass composition near the region of the knee and studies of cosmic ray anisotropy.

79 of the total 86 strings are currently operational. The remaining seven strings will be deployed during the 2010-2011 South Pole construction season. This work is based on one year of data taken with the 40-string configuration of IceCube which was operational from April 2008 to May 2009.

5.1 Digital Optical Modules

Photosensors are critical to the design and construction of a neutrino telescope since they are responsible for converting Čerenkov light to electrical signals. In the IceCube Neutrino Observatory, the fundamental photosensor component takes the form of a Digital Optical Module (DOM) [45]. Each DOM consists of a 10-inch (25 cm) Hamamatsu photomultiplier tube (model R7081-02) and associated electronics. These electronics include a 2kV high voltage power supply, a DOM main board, a delay board, and a LED flasher board. These components are responsible for the operation and control of the PMT as well as amplification, filtering, and calibration. The PMT, associated electronics, and mu-metal magnetic shield are housed within a 35.6 cm pressurized glass sphere. The photocathode glass of the PMT rests in a silicone gel in order to provide optical coupling to the glass sphere. The DOM is schematically shown in fig. 5.2.
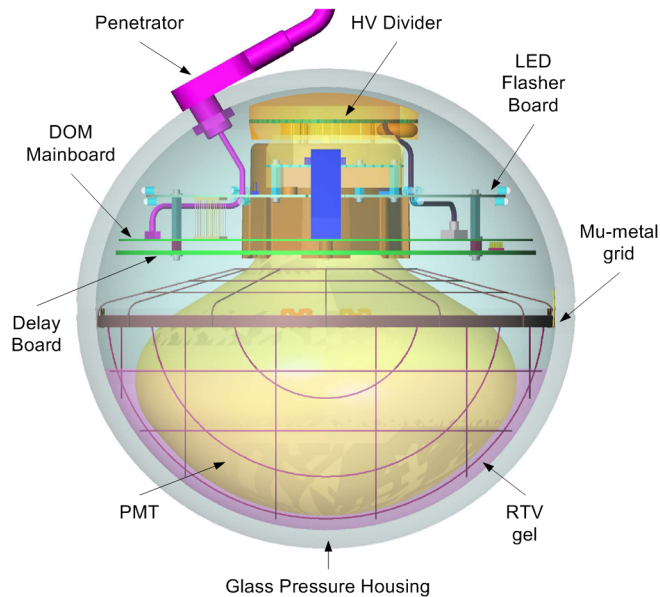
Figure 5.2: Schematic of the Digital Optical Module (DOM)

The PMT is sensitive in the wavelength range of 300 nm to 600 nm. The peak quantum efficiency of the PMT is 0.25 at around 400 nm and starts to plummet at shorter wavelengths due to the absorption of UV light by the photocathode glass. It has ten dynodes and operates in the voltage range between 1200 V and 1400 V with a gain of 10^7.

The flasher boards contain twelve LEDs each pointing radially outward. Six of the LEDs point in the horizontal direction and six point upward at a 48° angle. These flashers are useful for timing & geometry calibration, setting the energy scale for an energy reconstruction, and measurement of the optical properties of the South Pole Ice.

5.2 Data Acquisition System

Analog waveforms captured by the Hamamatsu PMTs are digitized in situ by the DOM main board. The analog waveform is first split between a trigger discriminator and the 75 ns delay board. If the discriminator threshold (0.25 photoelectrons) is surpassed, the raw waveform is then digitized in two ways.

An Analog Transient Waveform Digitizer (ATWD) digitizes the waveform into 128 bins at a sampling frequency of 300 MHz in order to capture the precise timing information of the analog signal in a 422 ns long digitized waveform. The ATWD has three channels operating at three different gains (0.25x, 2x, and 16x) that cover a dynamic range up to 400 PE/15 ns. A fourth ATWD channel is implemented for a variety of uses including an internal clock, local coincidence trigger conditions, and communications. In order to minimize dead time during a trigger readout, two ATWD chips were designed into the DOM main board. The second method uses a fast Analog

to Digital Converter (fADC) to capture longer waveforms. The 256 bins in the fADC are sampled at 40 MHz which gives a waveform that is up to 6.4 μs wide.

A single cable from the surface connects the 60 DOMs in a string to a surface junction box. (The junction box also receives input from two IceTop tanks.) The surface junction box provides power ($\pm 48\ VDC$) to the DOMs and relays the acquired data to the central counting house in the IceCube Laboatory (ICL). Each string is controlled by a specialized computer in the ICL called a DOMHub. Each DOMHub contains eight DOM readout (DOR) cards. The DOR card controls the power, boot-up, software, firmware updates, calibration, data transfer, and time calibration of the DOMs.

The DOMs can operate in local coincidence (LC) mode in order to reduce the dark noise trigger rate of 540 Hz. DOMs can transmit and receive LC tags to and from the neighboring vertical DOMs. When a DOM triggers, it transmits a LC tag to its immediate vertical neighbors and sets a time window of 1 μs. A DOM satisfies the LC condition If it receives a reciprocal tag from its vertical neighbor. Hard local coincidence was implemented for the 40-string configuration where only waveforms from DOMs that pass the LC condition are digitized and sent to the surface. Soft Local Coincidence is also possible where only limited timing information is sent for waveforms that do not satisfy the LC condition. Soft Local Coincidence (SLC) was first implemented for the 59-string configuration. The hard local coincidence condition reduces the false trigger rate to less than 1 Hz. For the 40-string data run, the event is then sent to a buffer for further filtering (ch. 9) if it passes a simple majority trigger (SMT) of eight triggered DOMs within a 5 μs time window.

Chapter 6

Optical Properties of the South Pole Ice

IceCube functions as a neutrino observatory by measuring the Čerenkov light emitted by relativistic muon tracks and showers. It is therefore extremely important to understand the propagation of Čerenkov photons through the detector medium, which for IceCube means a thorough understanding of the optical properties of the South Pole Ice. The ice at the South Pole has a complex depth structure consisting of horizontal ice sheets with varying degrees of dust concentration [46]. The glacial ice under the South Pole was created over a period of 165,000 years and currently has a thickness of 2820 m. The ice structure varies quite strongly with depth due to the accumulation of dust particles due to varying atmospheric conditions and volcanic activity during the glacial history of Antarctica. The largest concentration of dust in the South Pole ice is in a layer at 2050 m.

The optical properties of the South Pole ice are described by the absorption length and the scattering length as a function of depth. The absorption length λ_a is defined as the distance over which the photon survival probability drops by a factor of e. The scattering length λ_s is the average distance a photon travels before scattering with an average angle denoted by $\langle \cos \theta \rangle$. In Mie scattering, the photon wavelength is

comparable to the particle size and the scattering is peaked in the forward direction $\langle \cos \theta \rangle = 0.94$ [47]. It is customary to use the effective scattering length, λ_e, which is the distance after which the direction of a photon is randomized. It is given by:

$$\lambda_e = \frac{\lambda_s}{1 - \langle \cos \theta \rangle} \tag{6.1}$$

In general, the ice at the South Pole has short effective scattering lengths averaging around 20 m but long absorption lengths averaging around 110m. (This is in contrast to neutrino telescopes in water, where for example the Mediterranean site of the ANTARES experiment has longer effective scattering lengths of 100 m but shorter absorption lengths of 57 m [48].) At shallow depths above 1400 m, scattering is dominated by air bubbles trapped in the ice. Below 1400 m, a phase transition occurs such that air bubbles become a solid air hydrate phase with the gas within the ice giving the same index of refraction as the ice [49]. The Scattering and absorption of the ice instrumented by the IceCube detector are therefore dominated by the varying concentration of dust.

The effective scattering length λ_e and the absorption length λ_a has been parametrized in a six-parameter model [47]. The model is parametrized in scattering and absorption coefficients which are the reciprocal of the respective lengths:

$$b_e(400) = 1/\lambda_e(400) \tag{6.2}$$

$$a(400) = 1/\lambda_a(400)$$

The model fits the scattering and absorption coefficients at 400 nm, which the peak of the IceCube PMT quantum efficiency. The model is parametrized in terms of the temperature of the ice δT and six parameters denoted by α, κ, A, B, D, and E:

$$b_e(\lambda) = b_e(400) \cdot \left(\frac{\lambda}{400}\right)^{-\alpha}$$

$$a(\lambda) = a^*(400) \cdot \lambda^{-\kappa} + Ae^{-B/\lambda} \cdot (1 + 0.01\delta T) \qquad (6.3)$$

$$a^*(400) = D \cdot a(400) + E$$

Where α describes the wavelength dependence of the scattering coefficient as calculated by Mie theory. The parameter A describes absorption due to an *Urbach tail* which is a steep exponential decrease in absorption for wavelengths longer than the band gap energy of ice. The parameter B describes the absorption of light by the ice itself and is independent of the dust concentration. Parameters D and E describe absorption due to dust particles. The values of D and E vary with depth and are the dominant parameters that determine the absorption length for the relevant wavelength range of the IceCube PMTs.

The scattering and absorption coefficients as a function of depth have been measured with a variety of in-situ light sources [47] which has led to the AHA ice model. This model was originally derived for depths spanned by the the AMANDA detector and subsequently the ice properties below the dust peak at 2050 m were not directly measured. The AHA ice model was extrapolated to the clean ice region using ice core measurements at Vostok Station and Dome Fuji in Antarctica to scale the scattering

and absorption coefficients by using an age vs. depth relation [46]. The ice, however, was found to be significantly cleaner below the dust layer than was initially calculated.

Recent developments [50] have measured the ice properties over the full depth range of the IceCube detector using the in-situ LEDs present in every DOM main board resulting in what is called the South Pole Ice (SPICE) model. This new work also implements a new, direct-fit approach to fitting the optical properties of the South Pole ice. A global maximum likelihood procedure is performed on the data which fits all flashing LEDs in a single string that cover the entire depth range of IceCube simultaneously. The scattering and absorption coefficients as a function of depth for SPICE is shown in fig. 6.1.
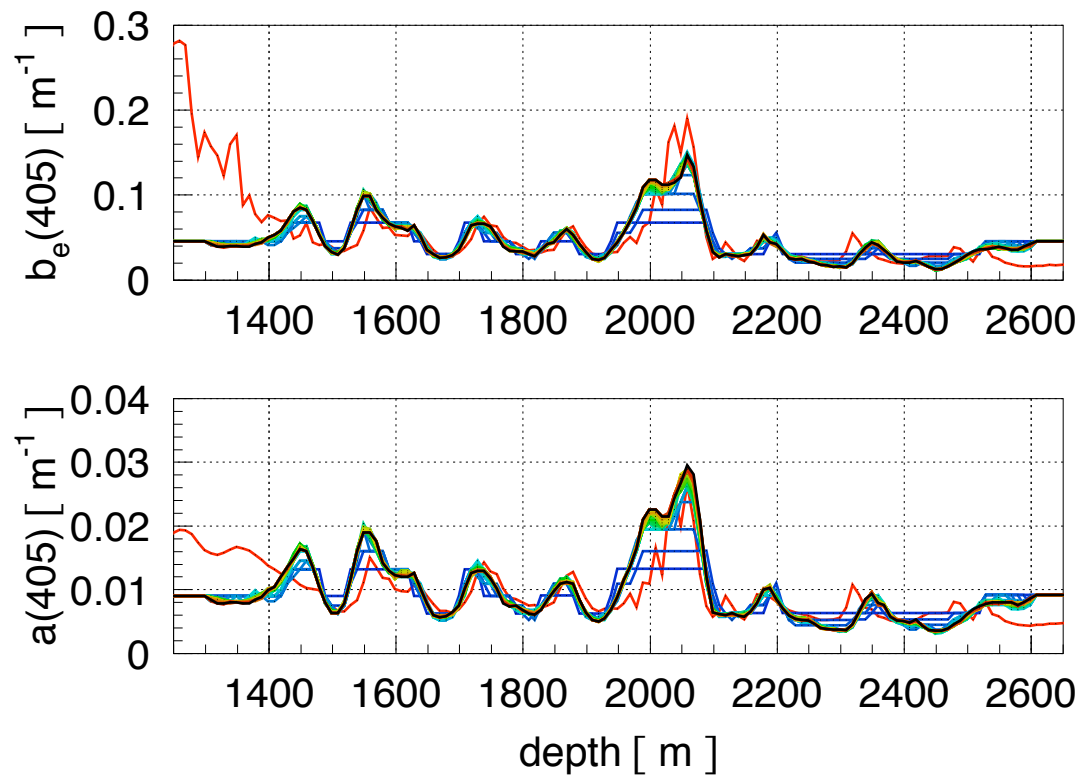
Figure 6.1: Scattering and absorption coefficients as a function of depth as derived by the South Pole Ice (SPICE) model [50]. The final SPICE model is in black. The previous AHA model is shown in red. The green area denotes the error range of the fit. The light blue lines show the iterative progress of the global likelihood fit procedure.

Chapter 7

Simulation

An accurate Monte Carlo (MC) simulation of the down-going atmospheric muon background, the atmospheric neutrino flux and the subsequent detector response is absolutely critical for this analaysis. A reliable MC simulation allows us to meaningfully compare IceCube data with the expectation from these various components and develop selection criteria to reject the significant atmospheric muon background. Since the atmospheric neutrino flux is the main background in the search for a diffuse astrophysical neutrino flux, an inaccurate simulation of the atmospheric neutrino flux and the subsequent detector response can lead to a false identification or rejection of a signal flux. An accurate simulation allows us to predict a physically meaningful sensitivity of this analysis to an astrophysical neutrino flux and make a discovery or set a convincing upper limit once the data is analyzed. An accurate simulation of the down-going atmospheric muon background also enables us to reliably estimate the contamination from this background in our final event sample. (The procedure of obtaining our final event sample for this data set will be discussed in ch. 9.)

The simulation of IceCube data proceeds in three stages:

- The *event generation* stage. Event generators create primary particles from

input flux models and assign physics parameters to each particle such as energy, direction, distance from the IceCube detector, and particle type.

- The *propagation* stage. Propagators transport these particles through different media such as the atmosphere, earth rock, and the Antarctic ice taking incorporating the various energy loss mechanisms and the production of secondary particles. The propagation stage also tracks the Čherenkov photons produced by the primary and secondary particles in the Antarctic ice.

- The *detector simulation* stage. This stage simulates the response of the IceCube detector.

These three stages are separately discussed in the following sections. All three stages of the simulation chain are handled in a collective software framework called *IceSim* [51]. The IceCube simulation chain is summarized in fig. 7.1.

7.1 Event Generation

The trigger rate of the IceCube experiment is dominated by down-going atmospheric muons, so an accurate simulation of this background is very important. The generation of extensive air showers initiated by high energy cosmic ray particles and the propagation of the subsequent muons through the atmosphere is handled by the CORSIKA (COsmic Ray SImulations for KAscade) [52] event generator. The generation of the air showers can be done at the primary cosmic ray energy spectrum of $E^{-2.7}$, or can be done with a higher power of $E^{-1.7}$ in order to increase the amount of event statistics at higher energies. The simulated events are therefore weighted to a steeper spectrum in order to do meaningful comparisons with data.
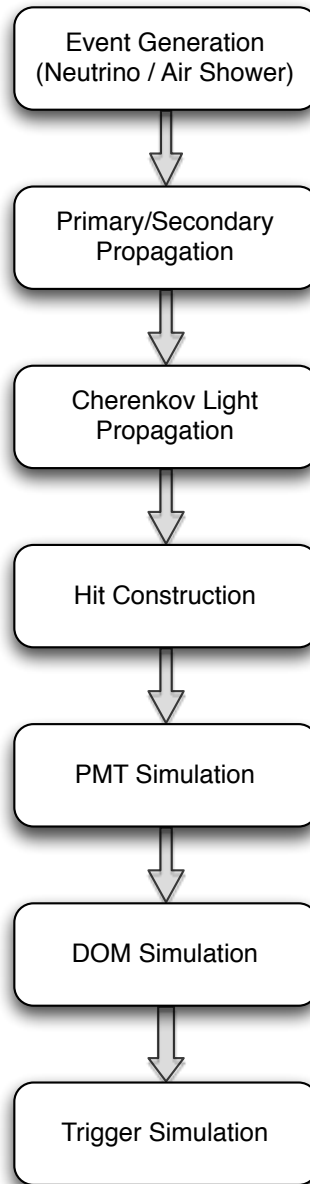
Figure 7.1: Summary of the Monte Carlo simulation chain of the IceCube experiment.

The generation of neutrinos of all flavors are handled by the Neutrino Generator software package which is based on the ANIS (All Neutrino Interaction Simulation) code [36] and uses the parton structure functions from CTEQ-5 [37]. Neutrinos are generated on a random position on the Earth's surface and then propagated through the Earth. ANIS takes into account the absorption due to charged current interactions and energy losses due to neutral current interactions. Note that ANIS handles both the generation and propagation of neutrino primaries. The structure of the Earth is modeled by the PREM, or Preliminary Reference Earth Model [53].

In order to reduce computation time, neutrinos that reach IceCube are forced to interact with the nearby Antarctic ice or bedrock to produce secondary particles that would trigger the detector. Each event is assigned a weight that represents the probability that this particular neutrino interaction has occurred. Neutrinos are typically generated with a baseline energy spectrum of either E^{-1} or E^{-2}. Despite the large number of atmospheric and astrophysical neutrino models described in ch. 3 and ch. 2, the event weights that are calculated can be used to weigh the baseline spectra to one of the models considered in those chapters.

7.2   Propagation

A daughter muon from a neutrino charged current interaction or an atmospheric muon passing from the atmosphere into earth rock is propagated using the Muon Monte Carlo (MMC) [39] code. MMC incorporates the various continuous and stochastic energy loss mechanisms described in ch. 4 to propagate the muon and the various secondaries it produces. The Čerenkov light produced by the muon and the various secondaries are then propagated separately from the muon track through the detector

volume to the DOMs in the IceCube detector.

There are two methods used for photon propagation in the IceCube simulation. Both methods can incorporate either ice model described in ch. 6. The first method is provided by the PHOTONICS [54] software package. PHOTONICS numerically tabulates the photon distribution results of various simulation runs with different light sources. Predicted light distributions in the IceCube simulation chain are thus drawn from these tabulated results. These PHOTONICS tables are computationally efficient and has the added benefit of allowing the full ice description to be used in the reconstruction of muon events as described in ch. 8.

The second method for propagating Čerenkov photons through the Antarctic ice uses direct photon tracking provided by the Photon Propagation Code (PPC) [50]. Although computationally intensive, direct photon tracking allows for a more complete description of photon propagation in the Antarctic ice and avoids many of the numerical approximations that are made with a numerically tabulated propagation strategy provided by a software package such as PHOTONICS. A significant improvement in computation speed is provided by the latest version of PPC which incorporates support for Graphics Processing Units (GPUs) with the CUDA architecture [55].

The choice of which photon propagation to incorporate into simulation production depends on the needs of the analysis. This analysis uses PPC for the simulation of neutrino Monte Carlo data and PHOTONICS for the simulation of the background atmospheric muons.

7.3 Detector Simulation

Once the Čerenkov photons have propagated to the DOMs, the detector response to these photons is simulated. Since all event information is digitized in situ, the detector simulation amounts to simulating the DOM response. The first step of this process is called *hit construction*. Hit construction uses the output of the photon propagation to determine the number of photons that propagate from the pressurized sphere that encases the DOM to the PMT photocathode. The *PMT simulation* step simulates the resulting photo-electrons and the output pulse of the PMT. The *DOM simulation* stage simulates the response of the DOM mainboard and electronics, including the PMT base transformer, the mainboard input discriminator, and the waveform capture from the ATWD and fADC. Finally, the *trigger simulation* applies the trigger logic to build an IceCube event. It fills the trigger status and rejects events that do not fulfill the trigger requirement.

7.4 Simulation Sample

There should ideally be as much simulated background live-time as the live-time of the IceCube 40-string data set of 375.15 days. Due to limited computational resources, however, the simulated background live-time is significantly less than the live-time of the data set. Using the weighting scheme to generate air showers with an $E^{-1.7}$ spectrum allows the effective live-time at higher energies to be substantially larger than the simulated live-time of the entire sample. Two classes of the atmospheric muon background are generated. The first class simulates down-going muons that trigger IceCube detector which come from a single extensive air shower and the second

class simulates muons from two separate air showers that trigger the detector within the trigger window. Table 7.1 summarizes the effective live-time in several energy ranges for simulated atmospheric muons from single extensive air showers generated with an $E^{-1.7}$ spectrum. The coincident atmospheric muon simulation used in this work does not employ the high-energy weighting scheme and has a total simulated live-time of 6 hours.

Table 7.1: Summary of simulated live-times at different energy ranges for atmospheric muons originating from single extensive air showers simulated by CORSIKA

All Energies	10 TeV	100 TeV
11 days	56 days	240 days

Neutrinos are simulated with a baseline energy spectrum of E^{-1} or E^{-2} as discussed above and the simulated events are then reweighed to an atmospheric or astrophysical neutrino model. This work uses an ensemble of neutrino Monte Carlo simulations to incorporate the various sources of systematic uncertainty discussed in ch. 11 to the analysis. Table 7.2 summarizes three main neutrino spectra used which includes the generation of ν_τ. Most of the systematic uncertainties discussed in ch. 11 have a corresponding Monte Carlo set of ν_μ generated with an E^{-2} spectrum with the equivalent number of events shown in Table 7.2.

Table 7.2: Summary of simulated $\nu + \bar{\nu}$ events used in this analysis. These events are all generated in the energy range of 100 GeV to 10^9 GeV.

Spectrum	Number of Generated $\nu + \bar{\nu}$
E^{-2} ν_μ	2×10^9
E^{-1} ν_μ	8×10^7
E^{-2} ν_τ	2×10^8

Chapter 8

Muon Track And Energy Reconstruction

Since the main science goal of the IceCube Neutrino Observatory is to detect high energy astrophysical neutrinos, determining the arrival direction, arrival time, and the energy of the daughter muons is of vital importance. The purpose of reconstruction is to convert the electrical signals recorded by the IceCube detector to an estimate of the muon trajectory and its energy. Reconstructing these physical quantities are also fundamental to background rejection since atmospheric muons and atmospheric neutrinos have different angle and energy distributions than astrophysical neutrinos.

The reconstruction of an event in IceCube is a specific case of a more general problem of estimating a set of unknown parameters $\{\vec{a}\}$ given a set of experimentally measured values $\{\vec{x}\}$ [56]. The parameters, $\{\vec{a}\}$, are determined by maximizing the likelihood function $L(\{\vec{a}\}|\{\vec{x}\})$ which for independent measured values x_i becomes:

$$L(\{\vec{a}\}|\{\vec{x}\}) = \prod_i^N p(x_i|\{\vec{a}\}) \tag{8.1}$$

where $p(x_i|\{\vec{a}\})$ is the probability density function (PDF) of observing the measured value x_i for given values of the parameters $\{\vec{a}\}$. The reconstruction is performed by

minimizing $-\log L$ with respect to $\vec{a}$ seeded by a first guess of the parameters $\vec{a}$.

For the specific case of a muon traveling through the Antarctic ice, the geometry of the muon track specifies the parameters $\{\vec{a}\}$ as shown in fig. 8.1. It is assumed that the Čerenkov radiation in this geometry is generated by a single muon track of infinite length (with $\beta = 1$) and forms a cone. The muon track is most generally described by the parameters

$$\vec{a} = (\vec{r_0}, t_0, \hat{p}, E_0) \tag{8.2}$$

where $\vec{r_0}$ is an arbitrary point along the muon track, t_0 is the time the track passes through point $\vec{r_0}$, E_0 is the energy of the muon at point $\vec{r_0}$, and $\hat{p}$ is the direction of the muon. The geometrical coordinates contain five degrees of freedom, namely the vertex position and the direction. The sixth degree of freedom is provided by the energy of the muon, E_0. One can reconstruct all six degrees of freedom together or reconstruct the geometry and the energy of the muon separately.

The measured values $\vec{x}$ depend on how the data was processed. The IceCube data acquisition system captures the full waveform $f(t)$ from the ATWD and the fADC digitizers as discussed in 5. This information is recorded as a series of voltages within the trigger window of the ATWD and the fADC. The full amplitude and timing information of the captured waveform can be directly used to reconstruct the muon parameters $\vec{a}$. It is common, however, to perform some initial processing of the waveform. Included in the initial processing step is baseline subtraction, removal of transformer droop and calculating the total charge of the waveform. In addition, the single photo-electron (SPE) response function of the photomultiplier tubes is deconvolved to obtain a series of Čerenkov photo-electron arrival times. This process is
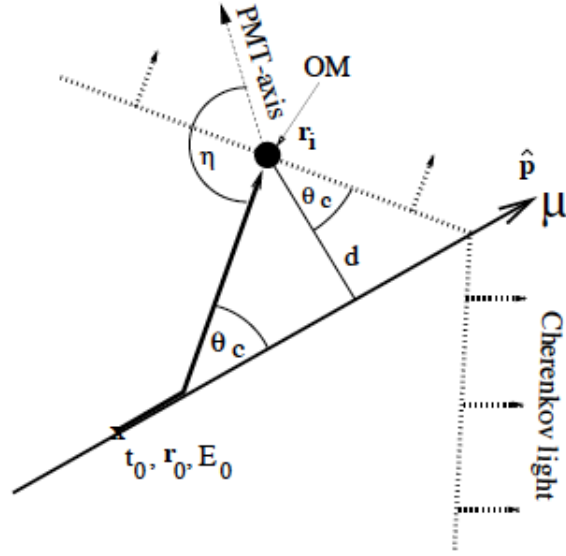
Figure 8.1: Geometry of the Čerenkov light front created by an infinitely long muon track with $\beta = 1$.

called *feature extraction* [57] and is a standard procedure performed on all IceCube data and monte carlo simulation.

8.1 First Guess Algorithms

The likelihood reconstructions require an initial track hypothesis to start the minimization. These initial hypotheses are provided by fast first guess methods that do not require an initial track geometry.

8.1.1 Line-Fit

The Line-Fit algorithm ignores the geometry of the Čerenkov light front and the optical properties of the medium and instead simplifies the geometry by assuming the light from the muon travels along a one dimensional line through the IceCube detector with a velocity $\vec{v}$. The location of each triggered OM $\vec{r}_i$ which trigger at time t_i can

be connected by a line:

$$\vec{r_i} = \vec{r} + \vec{v}t_i \tag{8.3}$$

The first guess algorithm simplifies to a χ^2 minimization problem where the χ^2 to be minimized is:

$$\chi^2 = \sum_{t=1}^{N_{pe}} (\vec{r_i} - \vec{r} - \vec{v}t_i)^2 \tag{8.4}$$

which has an analytic solution:

$$\vec{r} = \langle \vec{r_i} \rangle - \vec{v}\langle t_i \rangle \tag{8.5}$$

$$\vec{v} = \frac{\langle \vec{r_i}t_i \rangle - \langle \vec{r_i} \rangle \langle t_i \rangle}{\langle t_i^2 \rangle - \langle t_i \rangle^2} \tag{8.6}$$

where $\langle x_i \rangle = \frac{1}{N_{pe}} \sum_{i=1}^{N_{pe}} x_i$ denotes the mean of parameter x with respect to all photo-electrons. The line-fit algorithm gives a first guess for the more sophisticated log-likelihood reconstructions in the form of a vertex point r and a direction $e = \vec{v}_{LF}/|\vec{v}_{LF}|$.

8.1.2 Tensor of Inertia

The tensor of inertia algorithm models the light pattern that triggers the IceCube detector in a mechanical way. A charge amplitude from a PMT at $\vec{r_i}$ corresponds to a virtual mass a_i at r_i. A tensor of inertia $\vec{I}$ can be defined for this virtual mass distribution. The origin of $\vec{I}$ is the center of gravity (COG) of the mass distribution. These quantities are defined as:

$$C\vec{O}G = \sum_{i=1}^{N_{ch}} (a_i)^w \vec{r_i} \tag{8.7}$$

$$I^{k,l} = \sum_{i=1}^{N_{ch}} (a_i)^w [\delta^{kl}(\vec{r_i})^2 - r_i^k r_i^l] \tag{8.8}$$

The amplitude weight is chosen arbitrarily depending on how wants to weigh the photo-electron charges. The tensor of inertia has three eigenvalues I_1, I_2 and I_3 corresponding to its three main axes e_j. The smallest eigenvalue corresponds to the longest axis. For a track-like event, this eigenvalue is significantly smaller than the others and can be used to approximate the direction of the track. Cascade like events have a more spherical geometry in the detector, resulting in the three eigenvalues that are approximately equal to each other.

8.2   Likelihood Description

A likelihood function in the context of IceCube gives the an estimate of the parameters of a muon track given the observed data $f(t)$, which can be the captured waveform or a series of feature extracted photo-electrons. The estimate of the muon track is given by a maximum-likelihood estimation technique, which maximizes the probability of observing a photo-electron distribution $f(t)$ given an expected photo-electron distribution $\mu(t)$. The expected photo-electron arrival distribution is given by the PDF and depends on the hypothesis parameters $\vec{a}$ described in the last section. With $f(t)$ binned into K bins, the probability of observing n_i photons in the ith bin given an expectation of μ_i photons in the ith bin is given by Poissonian statistics. The overall probability for a single OM is given by the product over all bins:

$$L(\vec{a}|f(t)) = \prod_{i=1}^{K} \frac{e^{-\mu_i}}{n_i!} \mu_i^{n_i} \qquad (8.9)$$

Rearranging this equation gives:

$$L(\vec{a}|f(t)) = \left(\prod_{i=1}^{K} \frac{\mu_i^{n_i}}{n_i!}\right) \left(\frac{\prod_{i=1}^{K} \mu_{tot}^{n_i}}{\prod_{i=1}^{K} \mu_{tot}^{n_i}}\right) \left(\prod_{i=1}^{K} e^{-\mu_i}\right) \qquad (8.10)$$

$$L(\vec{a}|f(t)) = N_{pe}! \prod_{i=1}^{K} \frac{\left(\frac{\mu_i}{\mu_{tot}}\right)^{n_i}}{n_i!} \frac{\mu_{tot}^{N_{pe}}}{N_{pe}!} e^{-\mu_{tot}} \qquad (8.11)$$

where N_{pe} is the total number of photo-electrons. In this form, one can see that the likelihood function is a multinomial distribution giving the probability of arranging exactly N_{pe} photo-electrons into K bins multiplied by the Poisson probability of observing these N_{pe} photo-electrons. Taking the log of the likelihood function gives us:

$$\log L(\vec{a}|f(t)) = \sum_{i=1}^{K} \left(n_i \log \frac{\mu_i}{\mu_{tot}}\right) + N_{pe} \log \mu_{tot} - \mu_{tot} - \sum_{i=1}^{K} \log(n_i!) \qquad (8.12)$$

The first term is a sum over all bins. Each term in the sum $n_i \log \frac{\mu_i}{\mu_{tot}}$ corresponds to the log of the normalized timing probability of observing a photo-electron in the ith bin weighted by the number of observed photo-electrons in the ith bin. This timing probability is independent of the amplitude information present in $f(t)$. For the second and third terms, μ_{tot} is the total number of expected photo-electrons (which depends on the geometry and the energy of the muon), and N_{pe} is the total number

of observed photo-electrons in the OM. The second and third terms of the likelihood function depend solely on the amplitude information present in $f(t)$ and enable one to reconstruct the energy of the muon. The fourth term is a constant combinatorial term that does not depend on $\vec{a}$.

We evaluate Eq. 8.12 for all DOMs in the ice and sum these values as our log-likelihood function which we then maximize with respect to the free parameters of the track. This amounts to fitting the shape of the PDF to $f(t)$. This allows the reconstruction of not only the geometry of the muon, but also its energy. Every term in Eq. 8.12 can be used to reconstruct the geometry and the energy of the muon simultaneously. The geometry and energy of the muon can also be reconstructed separately by considering only the timing information for the geometry and the amplitude information for reconstructing the energy of the muon.

8.2.1 Time Likelihood

Although the form of Eq. 8.12 is completely general, in practice one reconstructs the geometry and the energy of the muon separately. For reconstructing the geometry of the muon, the arrival times of the photo-electrons give the most relevant information and the amplitude information in $f(t)$ can be ignored. This simplifies Eq. 8.12 to:

$$\log L(\vec{a}|f(t)) = \sum_{i=1}^{N_{pe}} p(t_{res}|\vec{a}) \tag{8.13}$$

The likelihood is simply a sum over the arrival time probabilities of the observed photo-electrons. The PDF of the arrival times are typically formulated as a function of the *time residual* which is the difference in time between when a photo-electron is

recorded and when it is expected to arrive according to the geometry of fig. 8.1:

$$t_{res} = t_{pe} - t_{geo} \tag{8.14}$$

$$t_{geo} = t_0 + \frac{\hat{p} \cdot (\vec{r_i} - \vec{r_0}) + d \tan \theta_c}{c_{vac}} \tag{8.15}$$

Here, t_{geo} represents the expected arrival time of a direct Čerenkov photon, a photon that travels undelayed from the muon directly to the photomultiplier tube without scattering. The shape of the probability density function should ideally be a delta function. The dominant effect on the shape of the timing residual distribution is the scattering of the antarctic ice [47]. The shape is also affected by PMT jitter, the dark noise rate and stochastic energy losses along the muon track.

The simplest form of the likelihood function is constructed from a PDF describing the arrival times of only the photons with the earliest arrival times at the location of the triggered photomultiplier tubes:

$$\log(L_{time}) = \sum_{i=1}^{N_{DOM}} p_1(t_{res,i}|\vec{a}) \tag{8.16}$$

where only the earliest photo-electron in every DOM contributes to the overall likelihood function. This is known as the single photo-electron (SPE) likelihood reconstruction. The first photon is usually less scattered than the average single photon, which modifies the PDF of the detected photo-electron. The arrival time distribution of the first of N photons is given by:

$$p_N^1 = Np_1(t_{res}) \left(\int_{t_{res}}^{\infty} p_1(t)dt \right)^{N-1} = Np_1(t_{res})(1 - P_1(t_{res}))^{N-1} \qquad (8.17)$$

P_1 is the cumulative distribution of the SPE PDF. This function is known as the multi-photo-electron (MPE) PDF and defines L_{MPE} [56].

8.2.2 Amplitude Likelihood

The second and third terms of Eq. 8.12 as discussed before allows one to reconstruct the energy of the muon or both the geometry and the energy simultaneously. This is made possible by modeling μ_{tot}, the total number of expected photo-electrons, as a function of the muon energy E_0. The simplest models of μ_{tot} describes the expected number of photo-electrons as scaling linearly with energy:

$$\mu_{tot,i} = \frac{E}{E_{ref}} \cdot \mu_{0,i} \qquad (8.18)$$

where $\mu_{0,i}$ is the number of expected photo-electrons at the ith OM at some baseline energy E_{ref}. This baseline energy is normally determined from monte carlo studies. Electromagnetic cascades are a classic example where the dependence of the amount of Čerenkov light on the cascade energy is a linear scaling factor [58]. Under such a linear scaling case, the geometry parameters of $\vec{a}$ can be made constant and Eq. 8.12 has an analytic solution in the energy:

$$\frac{d\log L}{dE} = 0 = \sum_{i=1}^{N_{OM}} \frac{d}{dE}\left(\sum_{j=1}^{K}(n_j \log p(t_{res}|\vec{a})) + N_{pe,i}\log(\frac{E}{E_{ref}}\mu_{0,i}) - \frac{E}{E_{ref}}\cdot\mu_{0,i}\right)$$

$$0 = \sum_{i=1}^{N_{OM}}\left(\frac{d}{dE}N_{pe,i}\log(\frac{E}{E_{ref}}\mu_{0,i}) - \frac{d}{dE}\frac{E}{E_{ref}}\cdot\mu_{0,i}\right)$$

$$0 = \sum_{i=1}^{N_{OM}}\left(\frac{N_{pe,i}}{\mu_{0,i}} - \frac{E}{E_{ref}}\right)$$

$$E = \frac{\sum_{i=1}^{N_{OM}} N_{pe,i}}{\sum_{i=1}^{N_{OM}} \mu_{0,i}}\cdot E_{ref} \tag{8.19}$$

The sum in the numerator is over the observed number of photo-electrons in every OM. The sum in the denominator is over the expected number of photo-electrons in every OM at the baseline energy.

8.2.3 Bayesian Likelihood

The likelihood function 8.12 can be extended to incorporate prior information of the atmospheric muon flux. Bayes' Theorem states for a track with parameters $\vec{a}$ and a given set of observables $\vec{x}$:

$$P(\vec{a}|\vec{x}) = \frac{P(\vec{x}|\vec{a})P(\vec{a})}{P(\vec{x})} \tag{8.20}$$

$P(\vec{x}|\vec{a})$ is simply the likelihood function defined in Eq. 8.12 or one of its simplified forms. The current version of the Bayesian reconstruction that is used in the IceCube data processing uses the SPE likelihood defined in Eq. 8.16. The $P(\vec{x})$ term is independent of the track parameters $\vec{a}$ and is a constant factor. The denominator therefore can be safely ignored. $P(\vec{a})$ is the *prior probability* distribution for the muon
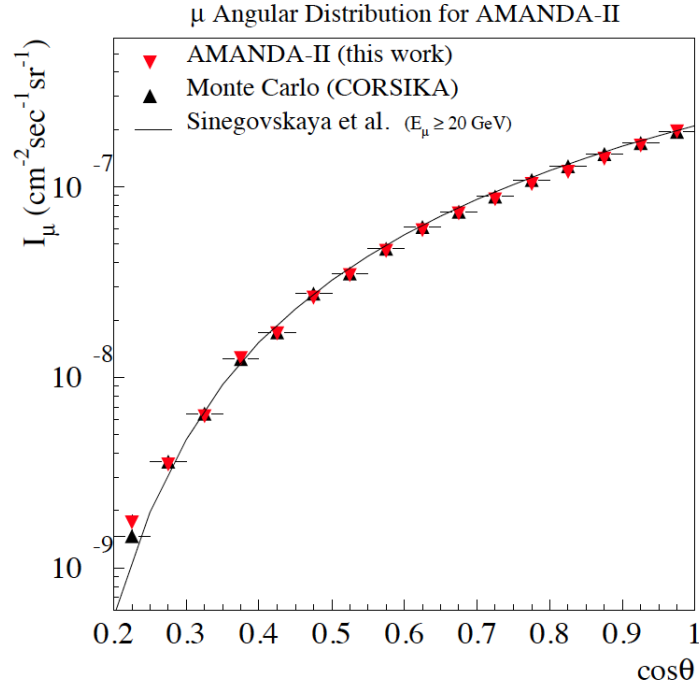
Figure 8.2: The angular distribution of atmospheric muons. $\cos\theta = 0$ is the horizon, while $\cos\theta = 1$ is vertically downgoing. Taken from [59].

track with parameters parametrized by $\vec{a}$. The atmospheric muon distribution has a strong and very well characterized zenith dependence which is shown in Fig. 8.2. This provides the prior probability distribution $P(\vec{a})$. The atmospheric muon flux becomes negligible near the horizon due to absorption by the Earth. By weighting the likelihood reconstruction with this prior angular distribution, $P(\theta)$, events that would otherwise reconstruct as upward-going through the Earth will instead reconstruct as downward-going. This Bayesian Likelihood is written as:

$$L_B = L \cdot P(\theta) \tag{8.21}$$

The Bayesian likelihood forces the muon to reconstruct as down-going. In prac-

tice, the Bayesian likelihood value is used as a test statistic by forming a likelihood ratio in order to compare the hypothesis of an upward going reconstructed muon with an alternative hypothesis of a track that is forced to reconstruct downward. Low values of the test statistic support atmospheric muons where as higher values of the likelihood ratio support upward going muon tracks arising from neutrinos. The Bayesian likelihood ratio test statistic is a powerful tool for reducing the mis-reconstructed upward-going atmospheric muon contamination.

8.2.4 Split Reconstruction

Multiple down-going atmospheric muons from different, uncorrelated extensive air showers can trigger the IceCube detector during its trigger window. These coincident muons are difficult to reject, and the reconstruction algorithms discussed in the previous sections need to be extended to a two muon hypothesis. The strategy we use is to perform a split reconstruction. This involves splitting the triggered DOMs to two separate groups and using each group of DOMs to reconstruct a muon hypothesis resulting in two reconstructed muon tracks.

The DOM splitting is performed one of two ways. The first is to perform a geometry splitting which takes advantage of the fact that two muons triggering IceCube during its trigger window would result in two groups of triggered DOMs that would be spatially separated in the detector. The splitting of the triggered DOMs into these two groups uses a plane which is defined to be perpendicular to the track and contain the Center of Gravity (see eq. 8.7) of the captured charge. The second method involves a splitting in time. This strategy uses the mean time of the captured waveforms to divide the DOM responses to two groups.

This work uses the split reconstruction as a means to reject coincident atmospheric muons that are mistakenly reconstructed as upward going muon tracks. The Bayesian likelihood (eq. 8.21) formalism can be extended to reconstruct a multiple down-going atmospheric muon hypothesis. A muon that is reconstructed as a single upward going track can be compared to an alternative hypothesis of multiple down-going muon tracks which provides a powerful tool for reducing the mis-reconstructed upward-going coincident atmospheric muon contamination.

8.3   Probability Density Functions

A reliable reconstruction of the muon geometry relies upon on an accurate probability density function that correctly models the photon hit probabilities and the photo-electron arrival times. A reliable reconstruction of the muon energy relies upon an accurate description of the light yield μ_{tot} in Eq. 8.12. The probability density functions can be written as an analytic function or by numerically tabulating the output of a photon propagation simulation.

8.3.1   The Pandel Function

The Pandel function is a PDF which parameterizes the arrival time distribution of Čerenkov photons as a gamma distribution. It assumes bulk ice (Antarctic ice without dust layers) and has the same form for muons and electromagnetic cascades. Its use is motivated by an analysis of laser light signals in the BAIKAL experiment [56]. It is defined as:

$$p(t_{res}) = \frac{1}{N(d)} \frac{\tau^{-d/\lambda} t_{res}^{(d/\lambda-1)}}{\Gamma(d/\lambda)} e^{-\left(t_{res}\left(\frac{1}{\tau}+\frac{c_{medium}}{\lambda_a}\right)+\frac{d}{\lambda_a}\right)} \tag{8.22}$$

$$N(d) = e^{-d/\lambda_a} \left(1 + \frac{\tau c_{medium}}{\lambda_a}\right)^{-d/\lambda} \qquad (8.23)$$

where λ_a is the absorption length, d is the closest approach distance between the OM location and the hypothesis, and λ and τ are two unspecified parameters whose form depends on whether the hypothesis is a muon or an electromagnetic cascade. The Pandel function is normalized, does not require much computing resources, and can be integrated analytically over the time. This makes the construction of the multi-photo-electron (MPE) time PDF straightforward. A sample illustration of the Pandel PDF as a function of the time residual is given in fig. 8.3.
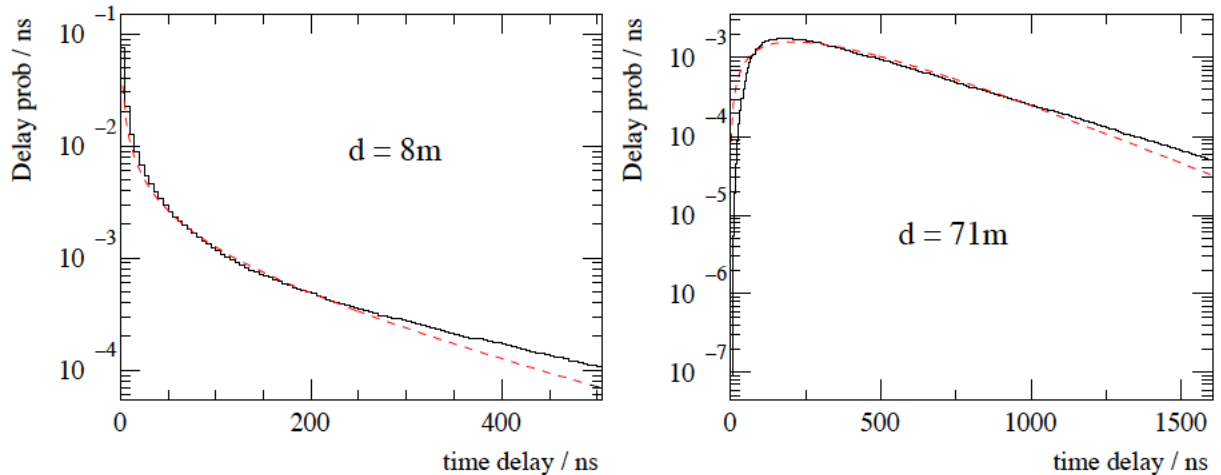
Figure 8.3: Illustration of the timing residual distribution of the Pandel function (dashed curve) and its comparison with monte carlo simulation (black histogram) at two distances from the muon track.

8.3.2 Photorec

The main disadvantage to using the Pandel function defined in eq. 8.22 for muon reconstruction is that it assumes bulk ice which treats the scattering and absorption coefficients as constant as a function of depth in the detector. This assumption limits

how accurately eq. 8.22 can describe the arrival time distribution of Čerenkov photons. It would be ideal to incorporate the more detailed layered description of the ice used in the simulation of IceCube data described in Ch. 7 into a likelihood reconstruction of muon tracks. This is made possible by the PHOTONICS photon propagation code since the results of the photon propagation are stored in the form of tables. An interface for the purposes of reconstruction called *Photorec* [54] has been developed that provides a numerical PDF describing the normalized arrival time probability distribution of Čerenkov photons and the expected amplitudes using the complete ice description used in the IceCube simulation. Tables are available for electromagnetic cascades and for bare muon tracks.

One of the major challenges in using Photorec for muon reconstruction is the large system memory requirements imposed by the PHOTONICS tables. A possible solution to this problem is the use of spline interpolation that parametrizes the tabulated photon arrival time probabilities and amplitudes at various depths in the ice as a spline function. This work is the subject of ongoing research and was first applied to the problem of cascade reconstruction [60].

The performance of the likelihood functions described in Ch. 8.2.1 and the probability density functions described in this section are summarized in Fig. 8.4. The waveform log-likelihood algorithm uses the captured waveform directly in Eq. 8.12 and the Photorec PDF. The Photorec log-likelihood algorithm uses the feature extracted waveform in Eq. 8.12 and the Photorec PDF. The SPE Pandel algorithm uses Eq. 8.16 and the Pandel PDF. The MPE Pandel algorithm uses Eq. 8.17 and the Pandel PDF. The complete description of the ice provided by the Photorec PDF
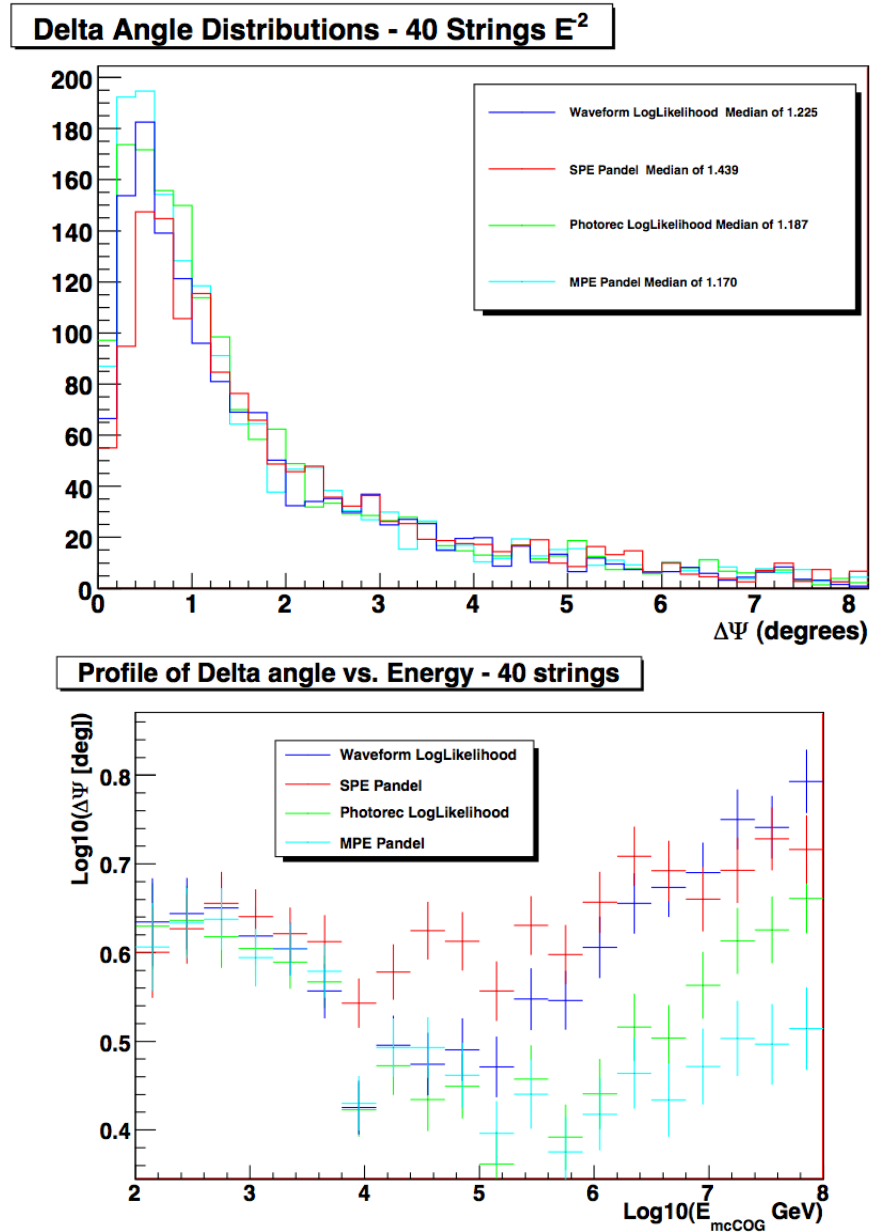
Figure 8.4: The top plot shows the angular difference between the reconstructed muon track direction and the Monte Carlo track direction as a measure of reconstruction performance. The study used neutrino Monte Carlo simulation generated with an E^{-2} spectrum in the 40 string configuration. The bottom plot shows the median angular difference as a function of energy.

provides a better angular resolution than the Pandel function. The MPE likelihood defined in eq. 8.17 gives the best angular resolution especially at higher energies. This demonstrates that the earliest Čerenkov photon arrival times are the most important for reconstructing the muon track geometry. The MPE reconstruction is used when the data from the 40 string configuration is processed. A future improvement to the MPE reconstruction algorithm would incorporate the Photorec PDF in the form of a spline function such that eq. 8.17 could be properly integrated.

8.4   Energy Reconstruction

Since extra-terrestrial sources of neutrinos are expected to have harder energy spectra than the atmospheric neutrino backgrounds, a reliable method for reconstructing the energy of the event is crucial. Here we summarize two algorithms that estimate the muon energy.

8.4.1 N_{ch}

The number of triggered PMTs (channels) in an event provides a simple energy estimator that is called N_{ch}. Muons with higher energy deposit more light in the detector subsequently triggering more DOMs. A problem with using N_{ch} as an energy estimator is that the dust concentration in the Antarctic ice affects the absorption of light, which affects the number of triggered DOMs in an event. This introduces a systematic depth dependence in using N_{ch} as an energy estimator. Nevertheless, N_{ch} represented a reliable and simple energy estimator for previous analyses done in IceCube and AMANDA, its predecessor. The correlation of N_{ch} with the simulated muon energy for the IceCube detector in the 40-string configuration is shown in fig.

8.5.
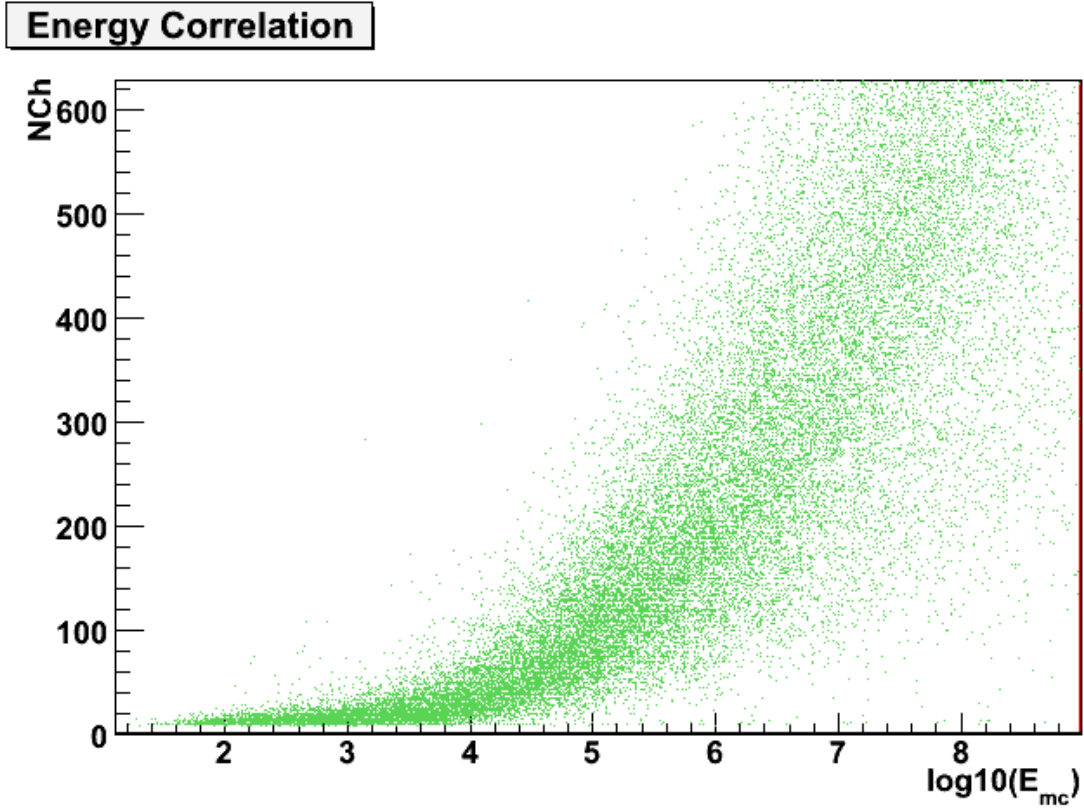
Figure 8.5: Scatter plot demonstrating the correlation between the number of triggered optical modules, N_{ch}, and the simulated energy of the muon closest to the center of gravity (COG) of the triggered DOMs for IceCube in the 40-string configuration. The COG is defined in eq. 8.7.

8.4.2 Photorec dE/dX Reconstruction

Estimating the energy of muon tracks is quite a challenge for non-accelerator experiments such as IceCube. An estimate of the muon energy is obtained through modeling μ_{tot} which is the total light yield of the muon defined in the second and third term of eq. 8.12. Although μ_{tot} allows one to reconstruct the energy of the muon, modeling the total light yield is difficult for high energy muons due to the stochastic
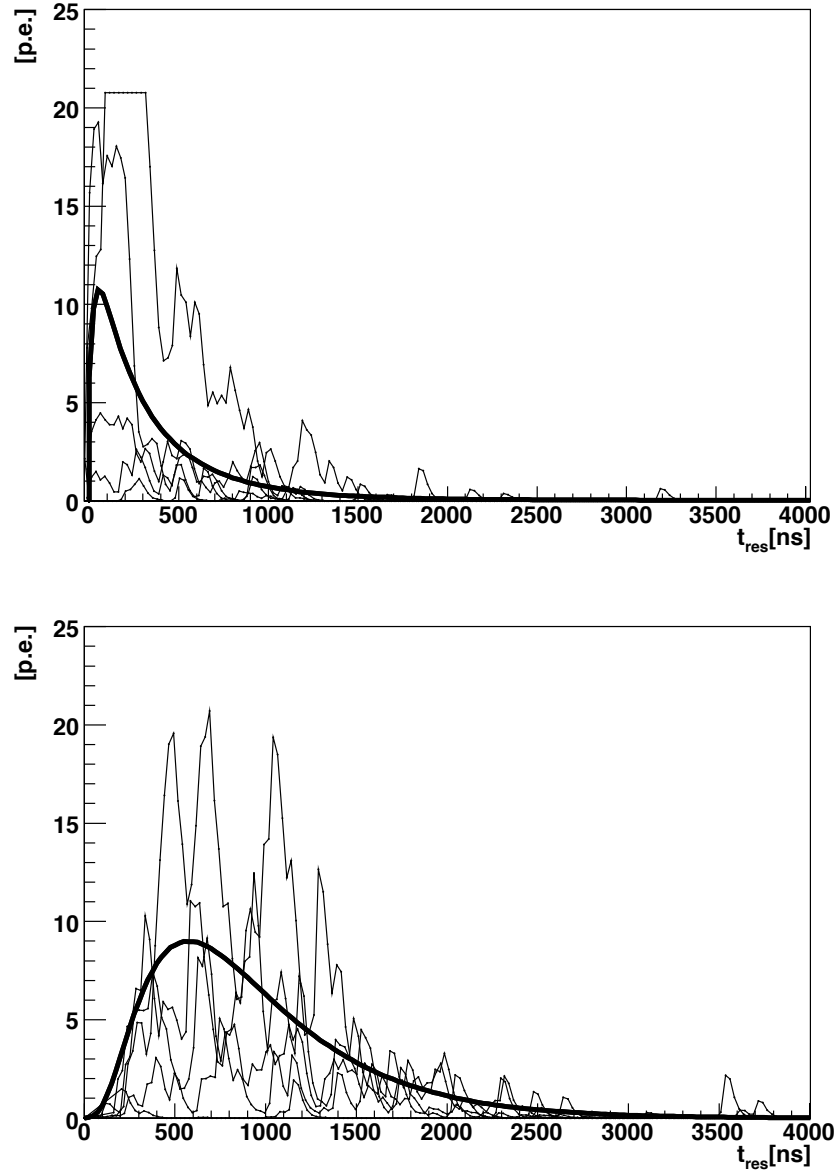
Figure 8.6: Comparison of the expected photo-electron distribution $\mu_{tot}(t)$ (thick line) from photorec lightsaber tables with a sample of individual simulated waveforms taken from a high energy muon MC sample (thin lines). Upper figure: 1 PeV muon at 53 meters from the track. Lower figure: 100 PeV muon at 147 meters from the track.

nature of muon energy loss. The stochastic muon energy loss mechanisms dominate over continuous energy losses above $\gtrsim 1$ TeV. The majority of Čerenkov light comes from the many secondaries produced by the various stochastic energy loss processes discussed in Ch. 4. What one measures is not the energy of the muon E_0, but the energy loss of the muon dE/dX. The relationship is approximately linear in this energy regime and is given by $dE/dX = a + bE$ as also discussed in ch. 4.

The Photorec dE/dX reconstruction algorithm models the average energy loss dE/dX of the muon as an infinite chain of mono-energetic electromagnetic cascades that are equally spaced by one meter. This approximation of the dE/dX profile of the muon models μ_{tot} as a continuous cylinder of light and is known as the *lightsaber* model. The Photorec energy reconstruction algorithm takes advantage of the Photorec interface to PHOTONICS and uses specialized muon tables called *lightsaber tables* for the purpose of modeling μ_{tot} in eq. 8.12 in order to reconstruct the dE/dX of the muon.

Fig. 8.6 demonstrates example comparisons between the expected photo-electron distribution as obtained with the photorec lightsaber tables and individual waveforms as obtained in the full MC simulation. It should be noted that the lightsaber model describes the average energy loss behavior of the muon track and therefore predicts an average photo-electron arrival profile. In many events, the individual waveforms in various DOMs will look quite different as shown in fig. 8.6. Individual stochastic energy losses near the DOMs may produce deviations beyond the statistical fluctuations from the Čerenkov light profile modeled by the lightsaber approximation.

The performance of the Photorec dE/dX reconstruction is characterized by con-
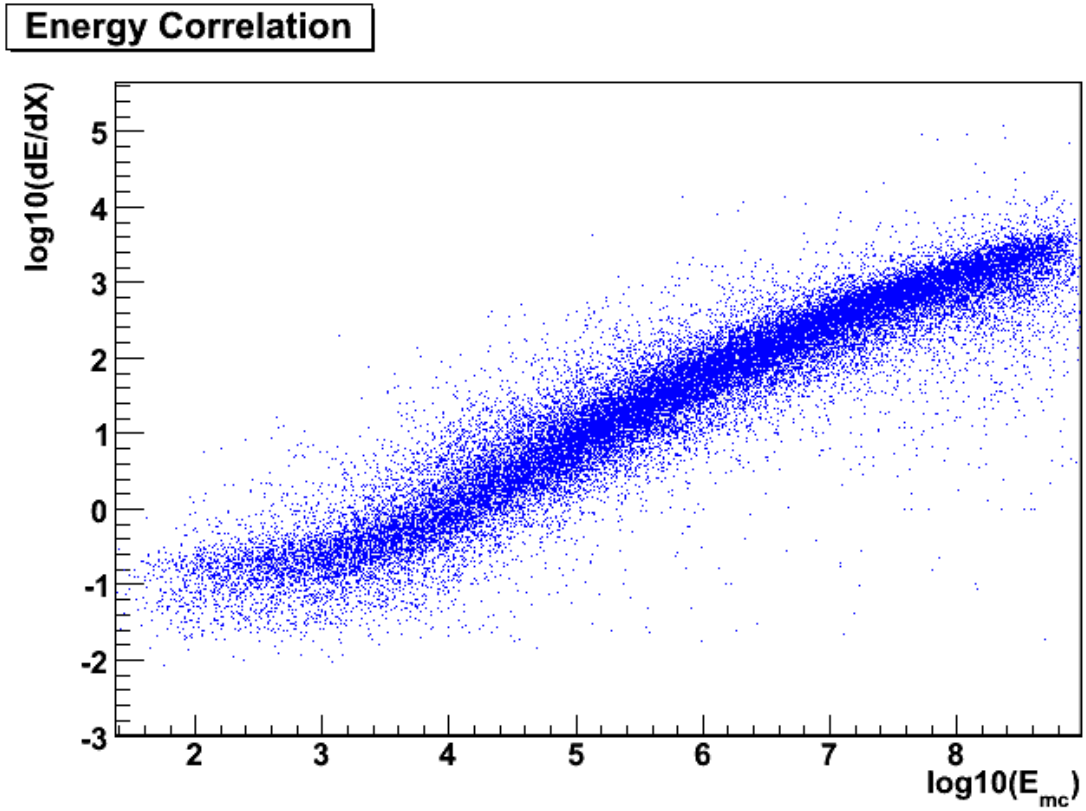
Figure 8.7: Correlation between the reconstructed dE/dX and the energy of the muon closest to the center of gravity (COG) of the triggered DOMs for IceCube in the 40-string configuration. The COG is defined in eq. 8.7. The Monte Carlo sample used was generated with an E^{-1} energy spectrum.
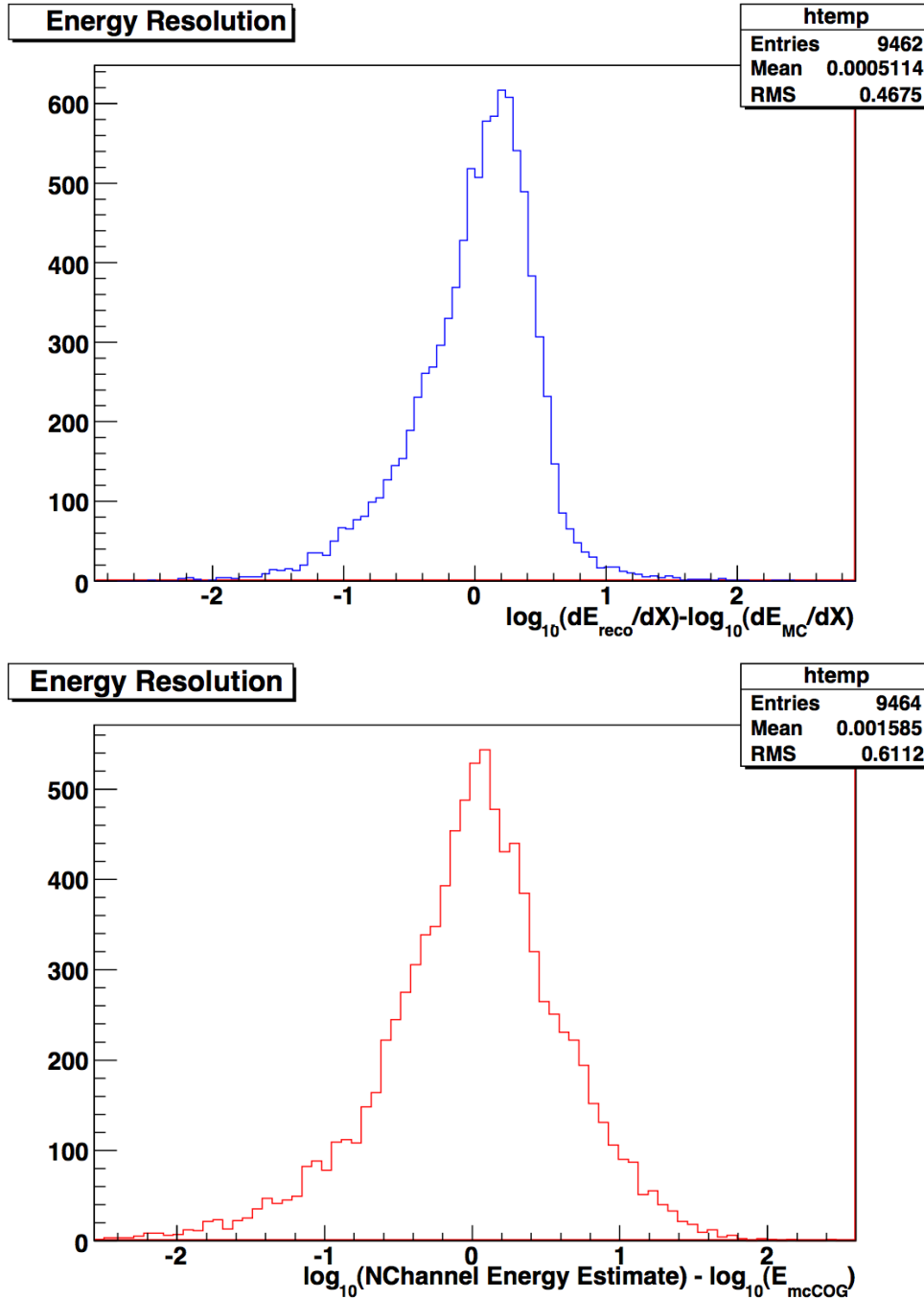
Figure 8.8: Energy resolution plots comparing the results from the photorec dE/dX reconstruction and the N_{ch} energy estimator for IceCube in the 40-string configuration. The energy resolution is calculated with respect to the simulated average muon energy loss. Upper Plot: Photorec dE/dX. Lower Plot: N_{ch}. The Monte Carlo sample used was generated with an E^{-1} energy spectrum.
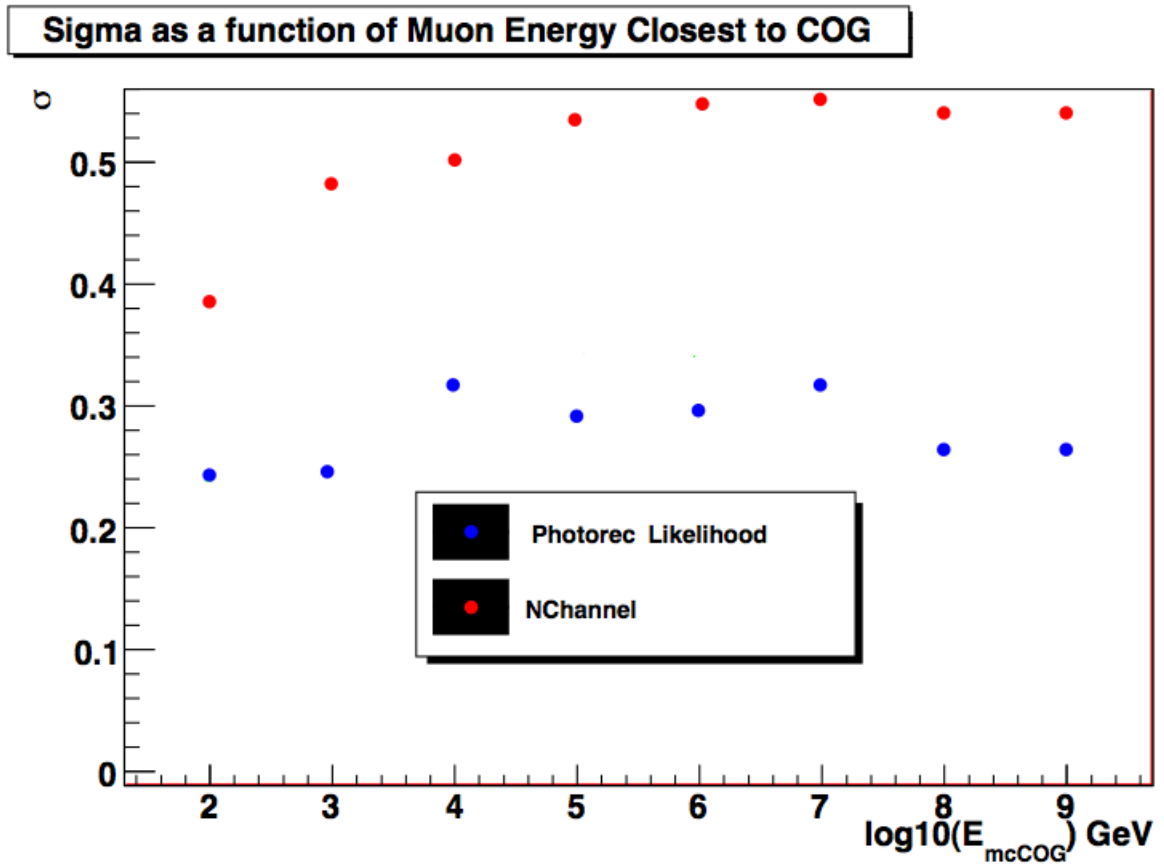
Figure 8.9: Energy estimator resolution as a function of the muon energy closest to the COG of the triggered DOMs for IceCube in the 40-string configuration. Gaussian functions are fit to the energy resolution distributions in different energy slices to get a numerical estimate of the resolution. The Monte Carlo sample used was generated with an E^{-1} energy spectrum.

sidering simulated high energy muons and neutrinos. Since IceCube measures the energy loss of the muon in the form of Čerenkov light produced by stochastic showers, we first derive the intrinsic resolution of the Photorec dE/dX reconstruction by using a sample of simulated high energy muons with a flat E^{-1} energy spectrum. We then characterize the response of the energy estimator to neutrino fluxes with different energy spectra.

The correlation between the Photorec dE/dX reconstruction and the muon energy for the IceCube detector in the 40-string configuration is shown in fig. 8.7. Only moderate quality criteria are applied. A containment cut is applied that selects only muons that traverse through the IceCube detector and whose direction are well reconstructed with a paraboloid sigma error estimate (See ch. 9) of 3 degrees or less. The dE/dX energy reconstruction is more linearly correlated with the muon energy than the N_{ch} estimator. Fig. 8.8 and fig. 8.9 compare the energy resolution of N_{ch} with the Photorec dE/dX reconstruction. The energy resolution is calculated by considering the average dE/dX of the simulated muon track. The average muon energy loss is calculated from the total energy deposit of the simulated muon in the detector divided by the total path length traversed by the muon through the detector. A numerical estimate of the overall energy resolution can be obtained by fitting Gaussian distributions to the curves shown in fig. 8.8. The standard deviation of these fits are summarized in table 8.1.

Table 8.1: Energy Resolution for IceCube in the 40 String Configuration

Energy Estimator	σ of $\log(E_{reco}/E_{MC})$
N_{ch}	0.43
Photorec	0.27
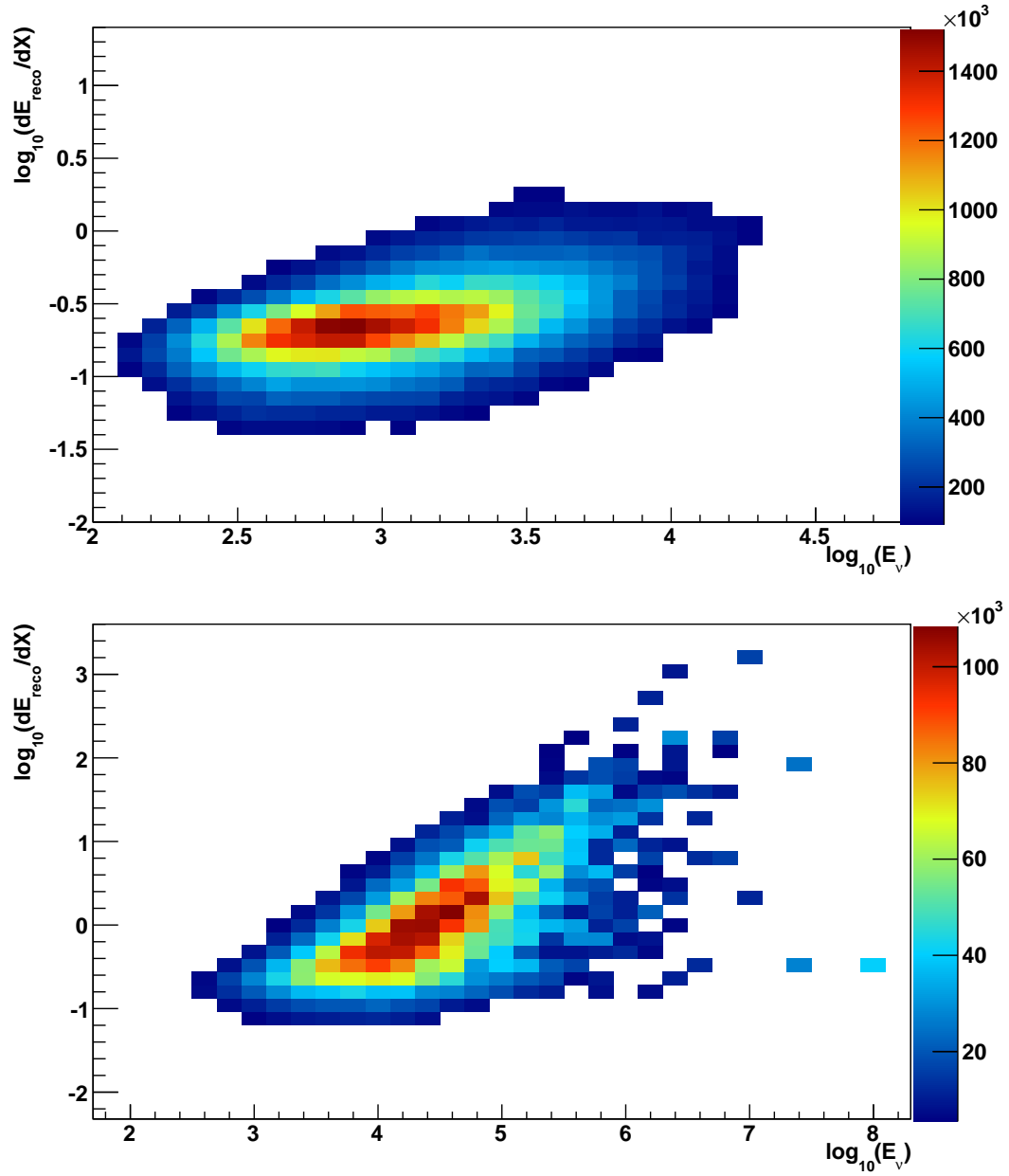
Figure 8.10: Correlation between the reconstructed dE/dX and the energy of the primary neutrino for IceCube in the 40-string configuration. The top plot demonstrates the correlation for atmospheric neutrinos and the bottom plot for a hypothetical astrophysical E^{-2} ν_μ flux.
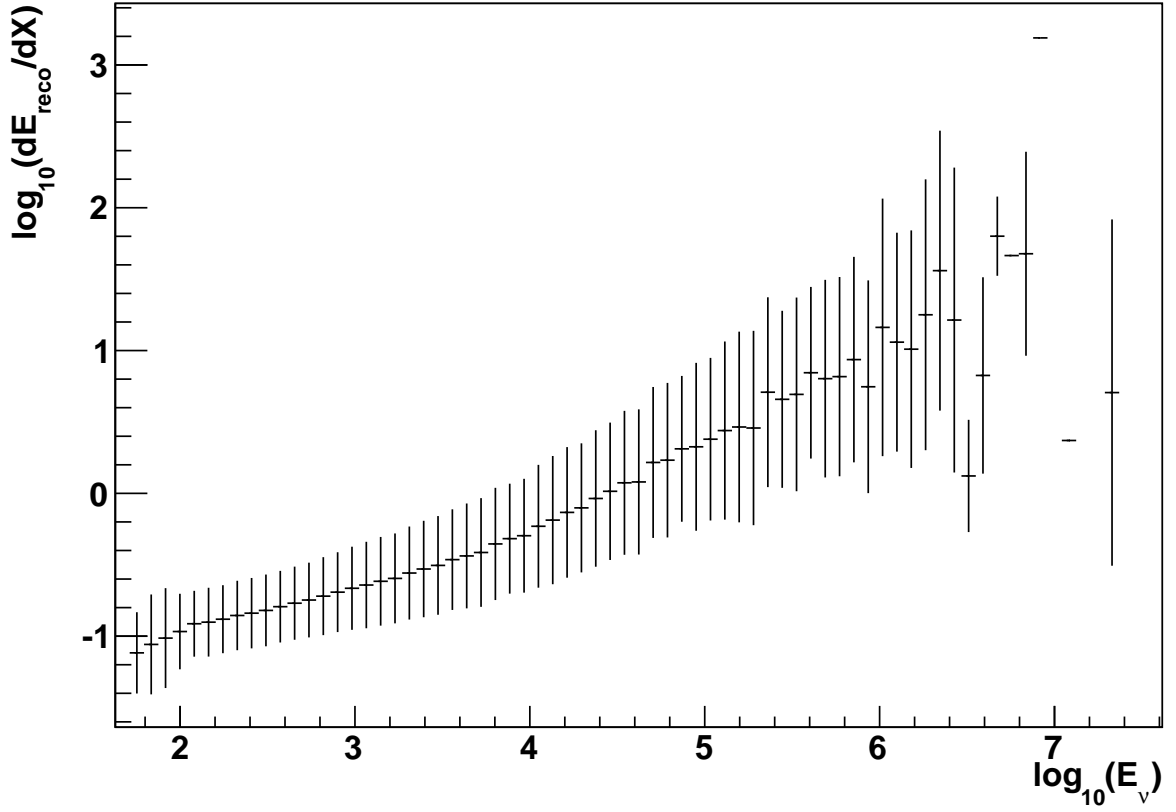
Figure 8.11: Profile of the RMS in the reconstructed dE/dX for different slices in the energy of the primary neutrino for IceCube in the 40-string configuration. We note that the spread gets larger for higher neutrino energies due to the increased muon range.

Table 8.2: dE_{reco}/dX spread for different values of E_ν for IceCube in the 40 String Configuration

E_ν	$\log_{10}(dE_{reco}/dX)$ RMS
10 TeV	0.38
100 TeV	0.55
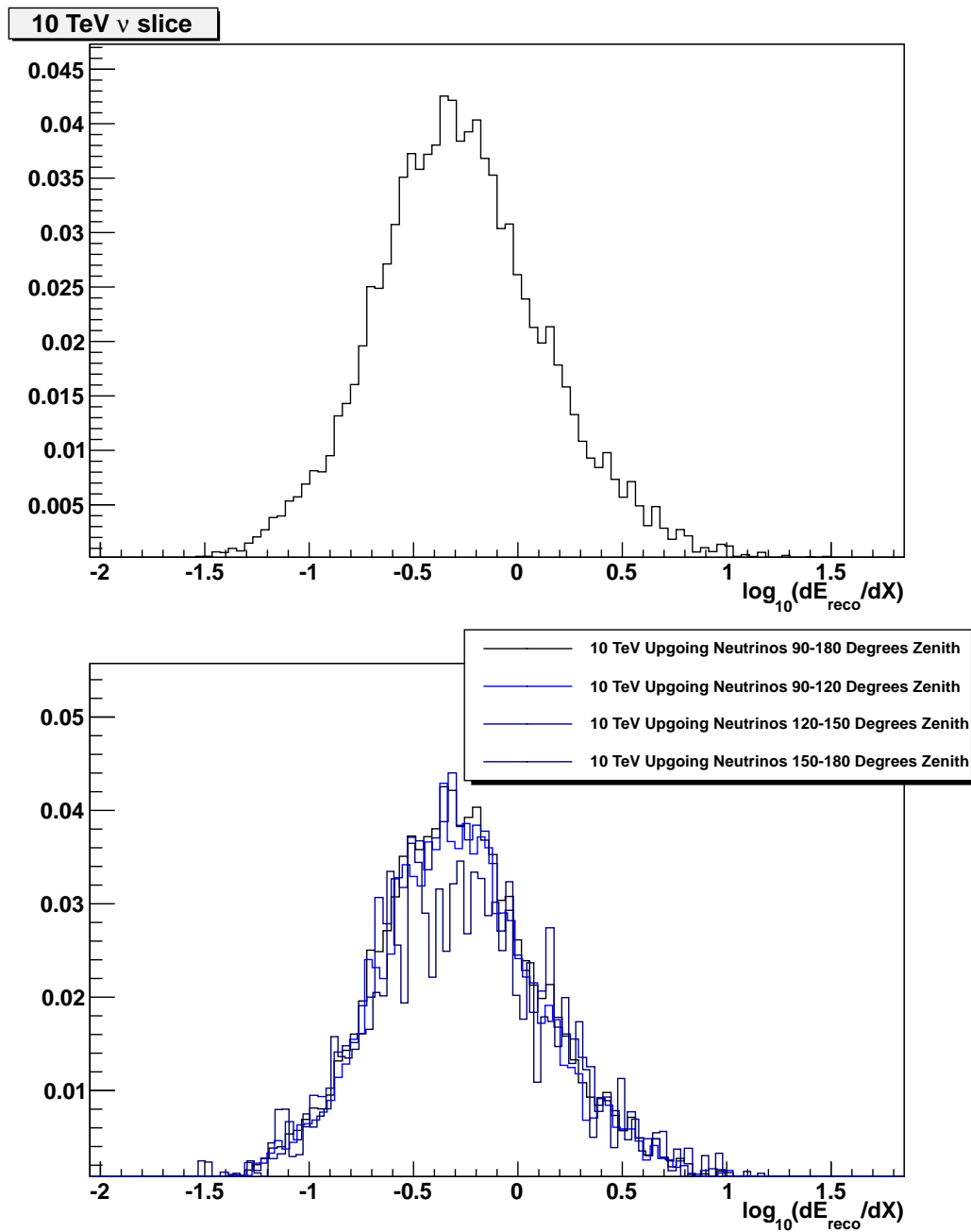
Figure 8.12: Distribution of Reconstructed dE/dX for a primary neutrino energy of 10 TeV for IceCube in the 40-string configuration. The top plot shows the distribution for all up-going zenith angles. The bottom plot shows the reconstructed dE/dX for different zenith ranges. We note that the spread does not have a large zenith dependence.
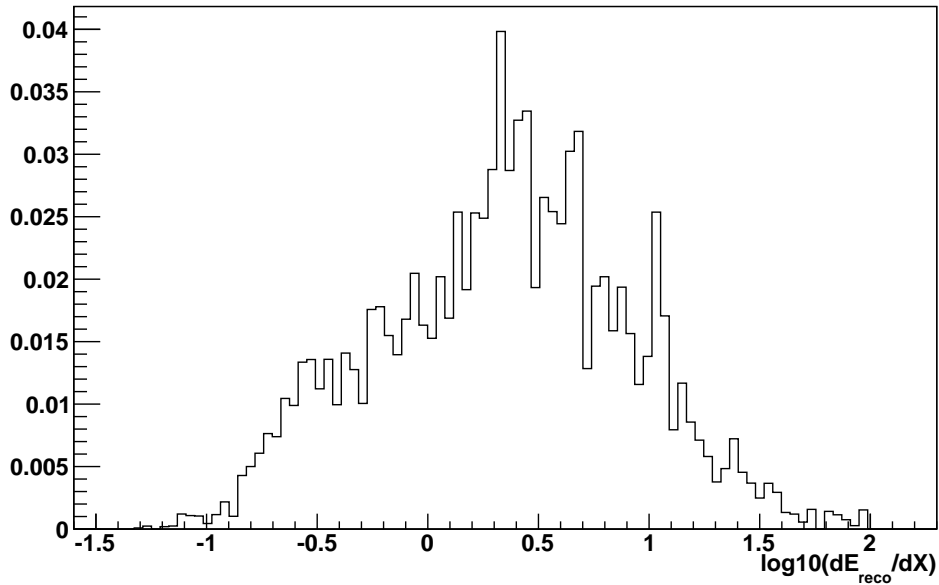
Figure 8.13: Distribution of Reconstructed dE/dX for a primary neutrino energy of 100 TeV for IceCube in the 40-string configuration.

With the muon energy resolution well characterized for many decades of the muon energy, we then study the performance of the Photorec dE/dX algorithm for different neutrino energy spectra. The correlation between the Photorec dE/dX reconstruction and the parent neutrino energy for the IceCube detector in the 40-string configuration is shown in fig. 8.10 for different muon neutrino energy spectra. The plots are shown with stringent quality criteria (see 9) that are eventually applied to the data in order to get a pure neutrino sample. Fig. 8.14 shows a profile of the RMS of the Photorec dE/dX reconstruction in different bins of the parent neutrino energy. We note that the RMS gets larger for higher neutrino energies due to the increased muon range. Fig. 8.12 shows the Photorec dE/dX distribution for 10 TeV neutrinos and for different zenith bands. We note that the spread does not have a large dependence on the zenith angle. Fig. 8.13 shows the dE_{reco}/dX distribution for
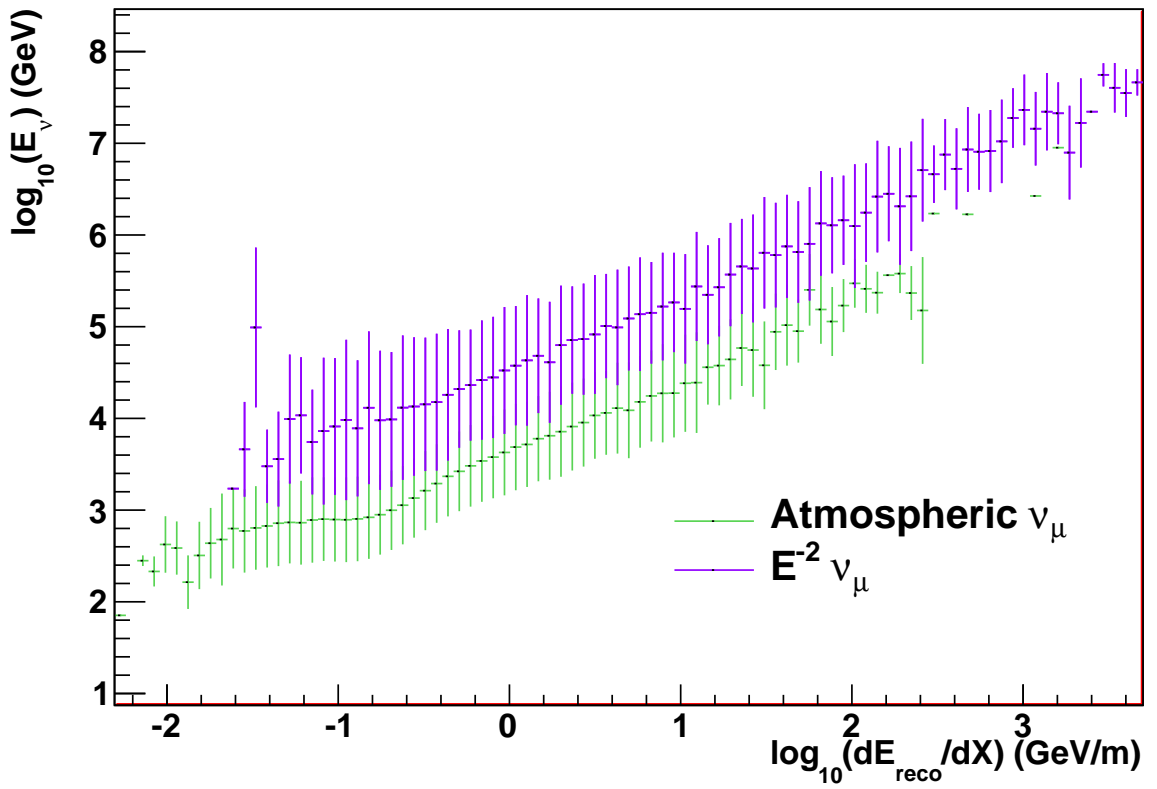
Figure 8.14: Profile of the RMS in the energy of the primary neutrino for different bands in reconstructed dE/dX for IceCube in the 40-string configuration. Shown are spectra for atmospheric neutrinos and a hypothetical E^{-2} astrophysical ν_μ flux.
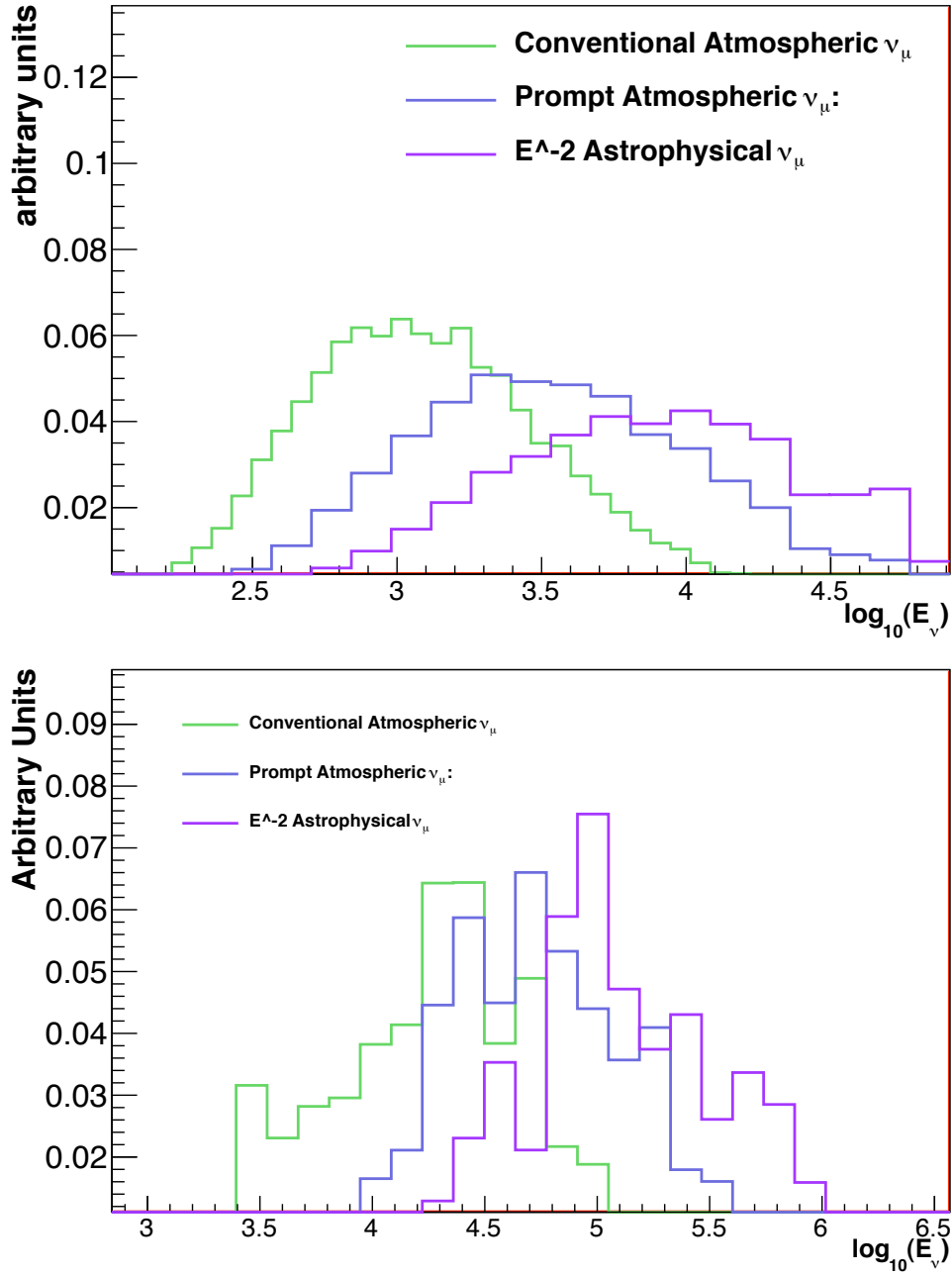
Figure 8.15: Distribution of the primary neutrino energy for different ν_μ spectra in two slices of dE_{reco}/dX for IceCube in the 40-string configuration. The top plot is for a dE_{reco}/dX of $0.252\,GeV/m$ (the peak of the atmospheric neutrino energy response) and the bottom plot is for a dE_{reco}/dX of $6.31\,GeV/m$ where the dE_{reco}/dX distribution is expected to turnover to an astrophysical $E^{-2}\,\nu_\mu$ spectrum with a normalization of $N_a = 1.0^{-7}GeV\,cm^2\,s\,sr$. The large bin to bin variations in the bottom plot is due to the lack of statistics in the simulation at higher energies.

100 TeV neutrinos, which is considerably wider than for 10 TeV ν_μ. We summarize the spread in dE_{reco}/dX for 10 TeV and 100 TeV neutrinos in Table 8.2.

A prior assumption of the neutrino energy spectrum must be made in making an estimate of the neutrino energy from a measured value of the reconstructed dE/dX. Fig. **??** shows a profile of the RMS of the simulated neutrino energy in different bins of dE_{reco}/dX. The profile is shown for conventional atmospheric neutrinos and astrophysical neutrinos. Fig. 8.15 demonstrates the distribution in the parent neutrino energy for two different values of Photorec dE/dX. The distributions are shown for conventional atmospheric neutrinos, prompt atmospheric neutrinos, and a hypothetical astrophysical neutrino flux. The significance of these two values of dE_{reco}/dX is that 0.252 GeV/m is the peak of the dE_{reco}/dX distribution for conventional atmospheric neutrinos and 6.31 GeV/m is the value of Photorec dE/dX for which the distribution is expected to turnover to an astrophysical E^{-2} ν_μ spectrum with a normalization of $N_a = 1.0^{-7} GeV cm^2 \ s \ sr$. Table 8.3 characterizes the spread in primary neutrino energy for different spectral shapes for these two important values of dE_{reco}/dX.

Table 8.3: $\log_{10}(E_\nu)$ RMS for two values of dE_{reco}/dX for IceCube in the 40 String Configuration

dE_{reco}/dX	Atmospheric ν_μ RMS	Prompt ν_μ RMS	Astrophysical ν_μ RMS
0.252 GeV/m	0.43	0.5	0.52
6.31 GeV/m	0.52	0.49	0.51

The energy scale of the Photorec dE/dX reconstruction depends on the light yield for stochastic electromagnetic cascades. The reconstruction algorithm incorporates the effective muon track length parameterization derived by C. Wiebusch (eq.

4.8) from which the total amount of Čerenkov light from stochastic electromagnetic cascades can be calculated. Another parameterization of the effective muon track length has been derived by M. Kowalksi [61], but this parameterization has a negligible affect on the energy scale of the Photorec dE/dX reconstruction. One can approximate a larger change in the muon light yield by varying the stochastic energy loss cross sections in the muon propagation stage in the simulation. This is discussed in ch. 11. We note here that such an increase or decrease in the muon energy loss cross sections do not largely affect the energy scale of the reconstructed dE/dX distribution.

8.5 Iterative Reconstruction

The log-likelihood reconstructions described in this chapter need to be seeded with a vertex and a direction which is normally provided by the first guess algorithms described in this chapter. It is possible for the log-likelihood reconstruction to fit a vertex and direction from a local minimum in the likelihood space. This undesirable behavior can be mitigated by performing multiple iterations of the same log-likelihood reconstruction, but with a variety of seed values for the geometry and the direction. This increases the chances that the global minimum is indeed found and the most accurate track is returned. There is a trade off between the number of iterations performed and the total computing time required. $16 - 64$ iterations are commonly performed.

Chapter 9

Event Selection

The data used for this analysis were taken using IceCube in the 40 string configuration which operated between April 2008 and May 2009 giving a total live time of 375.5 days. Since the goal of this analysis is to look for evidence of astrophysical muon neutrinos in the atmospheric muon neutrino energy spectrum, the data must first be processed in order to obtain a pure sample of muon neutrinos. This involves rejecting the large amount of down-going atmospheric muon background. The background rejection strategy was developed using simulation in several stages. First, the triggered event rate at the South Pole was reduced using a level 1 software filter before the data was transmitted via satellite to the northern hemisphere. The level 2 filtering stage sees CPU intensive reconstructions performed offline in the northern hemisphere. Finally, analysis level cuts were applied to reject the atmospheric muon background and obtain a pure muon neutrino sample.

9.1 Filtering

The data rate from the IceCube DAQ far exceeds the bandwidth capability of the satellite (35 GB/day) that transmits data from the South Pole to the northern

hemisphere. A significant reduction of the trigger-level data rate is required before the data is transmitted to the northern hemisphere. The Processing and Filtering (PnF) system runs on a cluster of computers at the South Pole which takes events from the DAQ and performs a variety of fast first guess reconstruction algorithms (see ch. 8). The PnF system sends an event to the South Pole Archival and Data Exchange (SPADE) system for transmission to the northern hemisphere if it passes one or more of the software filters set up at the South Pole. Although there are a variety of filters in use, only events passing the muon and the extremely high energy (EHE) filter are used in this analysis. The EHE filter simply tags high energy events with $\log(N_{pe}) = 3.5$ or greater photoelectrons. The muon filter, however is the primary filter in this analysis for rejecting down-going atmospheric muons and retaining candidate muon neutrino events near and below the horizon. It is also a common filter shared by other analyses such as the point source analysis and the atmospheric neutrino analysis.

The level 1 muon filter consists of two cut branches and a NChannel threshold of 10. Two reconstructions using the simplified SPE likelihood (eq. 8.16) are performed as inputs to the level 1 filter. The first reconstruction is seeded with the result of a LineFit first guess reconstruction. The second is seeded with the opposite direction of the first guess result with the intention of reducing the number of mis-reconstructed events that might otherwise pass the filter. Branch 1 of the filter tags whether both log likelihood reconstructions pass a specified zenith cut. Branch 2 determines if one of the reconstructed tracks passes a specified zenith cut. The filter branches are defined in table 9.1. An event passes the level 1 muon filter if it passes either the branch 1 or branch 2 criteria.

Level 2 IC40 Muon Processing
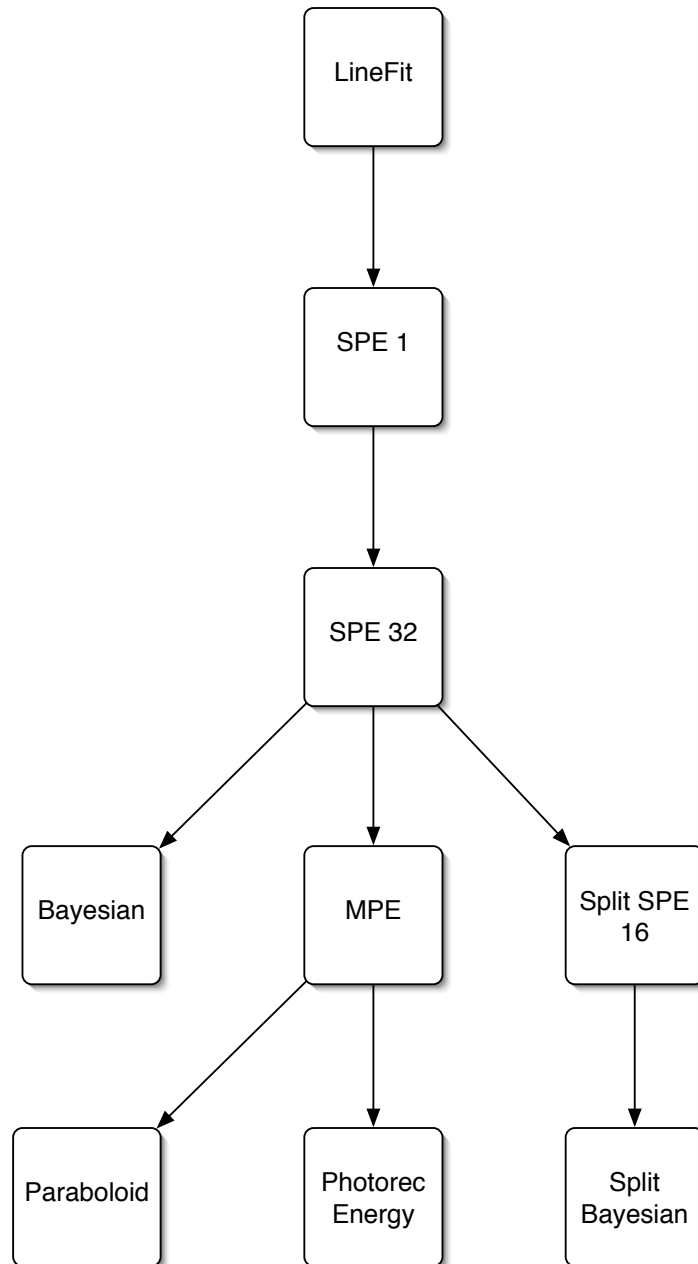
Figure 9.1: Summary of the Level 2 muon filter data processing chain used for this analysis.

Table 9.1: Summary of the level 1 muon filter for IceCube in the 40 string configuration

Branch	Selection Criteria
Branch 1	$(\theta_{SPE1}$ AND $\theta_{SPE2} \geq 80$ AND $N_{ch} \geq 10)$ OR
	$(\theta_{SPE1}$ AND $\theta_{SPE2} \geq 70$ AND $N_{ch} \geq 16)$
Branch 2	$N_{pe}/N_{ch} \geq 5$ AND $(\theta_{SPE1}$ OR $\theta_{SPE2} \geq 50$ AND $N_{ch} \geq 20)$ OR
	$(\theta_{SPE1}$ OR $\theta_{SPE2} \geq 70$ AND $N_{ch} \geq 10)$

The more CPU intensive level 2 processing of the muon filter is done in the northern hemisphere. The processing is summarized in fig .9.1. The level 2 processing chain has the following steps performed offline on events that pass either the muon filter or the EHE filter:

- Feature Extraction: The waveform is first reprocessed with a more complete feature extraction (see ch. 8).

- First Guess Reconstruction: The LineFit first guess algorithm is run on the data.

- SPE reconstruction: The SPE log-likelihood reconstruction is performed.

- SPE32 reconstruction: The previous SPE log-likelihood reconstruction seeds a subsequent SPE log-likelihood reconstruction run with 32 iterations.

- Bayesian Reconstruction: The Bayesian reconstruction (eq. 8.21) is performed using the SPE likelihood and seeded with the result of the SPE 32 iteration reconstruction.

- Split Bayesian Reconstruction: The Bayesian reconstruction is ran on a two-muon hypothesis. Each muon hypothesis is reconstructed using the SPE likelihood with 16 iterations. (See sec. 8.2.4 for a discussion on split reconstruction.)

- MPE Reconstruction: The MPE log-likelihood reconstruction (eq. 8.17) is performed using the result of the SPE 32 likelihood reconstruction as a seed.

- Paraboloid: The paraboloid error estimate (see discussion in the next section) of the MPE log-likelihood reconstruction is calculated.

- Photorec Energy Reconstruction: The Photorec Energy Reconstruction is run using the result of the MPE likelihood reconstruction as a seed.

The zenith and dE_{reco}/dX distributions at filter level comparing data and Monte Carlo for one day of IceCube 40-string data is shown in fig. 9.2.

9.2 Analysis Level Cut Variables

In order to prevent any inadvertent tuning of the event selection criteria that would bias the final event sample, a blindness procedure was followed. The blindness criteria for the IceCube 40-string dataset allowed thirty days of data taken during the month of June 2008 (called the "Burn Sample") to be used to develop an analysis. The burn sample and simulation were used to establish the final analysis level cuts for this analysis. The observables used to separate neutrino like events from the down-going muon background events are derived from the reconstructed track and are summarized below:

- θ_{MPE}: The zenith angle of the muon track reconstructed with the MPE likelihood is used as a cut parameter. As discussed in section 8.2.3, the atmospheric muon flux has a well characterized zenith dependence that quickly drops to zero at the horizon.
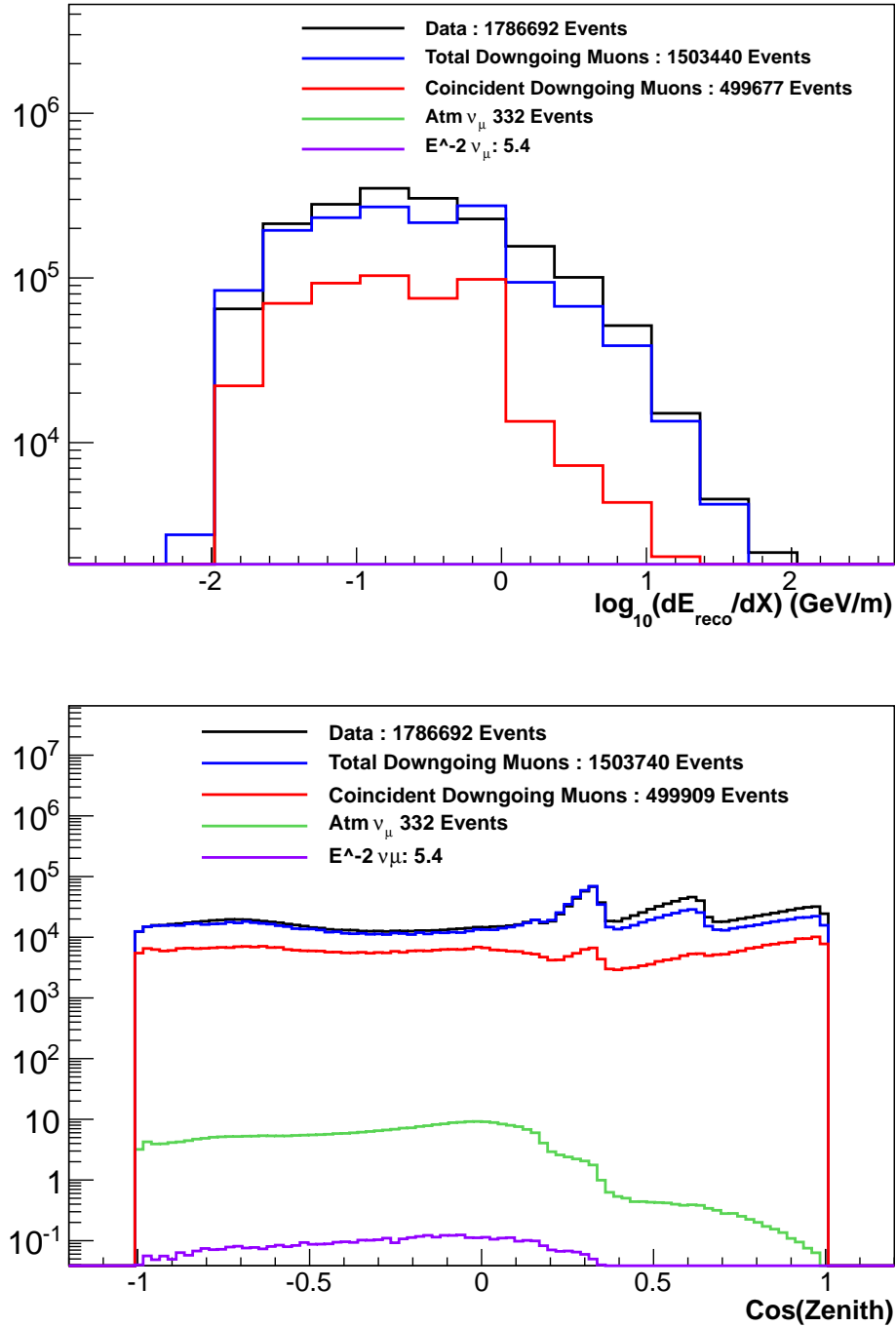
Figure 9.2: Distributions comparing data to simulation for one day of IceCube data at filter level. Top plot is the dE_{reco}/dX distribution and the bottom plot is the zenith distribution. Shown is the total sum of Corsika atmospheric muon simulation from single and coincident atmospheric muons, simulated atmospheric ν_μ, and a hypothetical astrophysical E^{-2} ν_μ flux.

- **Reduced log-likelihood of the MPE reconstruction,** $\frac{\log(L_{MPE})}{N_{ch}-5}$: The reduced log-likelihood value is the log-likelihood value of the reconstructed track divided by the number of degrees of freedom of the fit. The number of degrees of freedom is taken to be the number of triggered DOMs minus five, which is the number of free parameters in the reconstruction. A smaller value of the reduced log-likelihood indicates that the Čerenkov photons arrived at the individual DOMs as predicted by the Pandel function. It is an efficient observable for separating higher energy atmospheric neutrinos from mis-reconstructed atmospheric muons.

- **Redefined reduced log-likelihood of the MPE reconstruction,** $\frac{\log(L_{MPE})}{N_{ch}-2.5}$: The reduced log-likelihood defined above should be independent of the energy of the muon track. In practice, the reduced log-likelihood is not energy dependent for lower values of N_{ch}. Redefining the effective degrees of freedom to $N_{ch} - 2.5$ makes the reduced log-likelihood energy dependent at low N_{ch} making this an efficient observable for separating medium and lower energy atmospheric neutrinos from mis-reconstructed atmospheric muons.

- **Paraboloid sigma error estimate of the MPE reconstruction** σ_{MPE}: A technique for estimating the 1σ error of a log-likelihood reconstruction was developed [62] that calculates an error ellipse in the likelihood function space of the reconstruction. The 1σ error is given from the major and minor axis of the event error ellipse: $\sigma = \sqrt{(\sigma_x^2 + \sigma_y^2)/2}$. This parameter provides an event by event uncertainty in the likelihood function used in the reconstruction of muon tracks.

- **Log-likelihood ratio of the Bayesian reconstruction to the SPE-32 reconstruction** $\log(L_{bayesian}) - \log(L_{SPE32})$: The Bayesian likelihood ratio compares the hypothesis of an up-going muon track with the alternative hypothesis of a down-going muon track reconstructed with the Bayesian prior defined in eq. 8.21. The likelihood ratio of the two reconstructions provides a powerful observable to reject mis-reconstructed atmospheric muons. Low values of the likelihood ratio supports the alternative hypothesis of a down-going muon, where as higher values indicate an up-going muon track.

- **Log-likelihood ratio of the split Bayesian reconstruction to the SPE-32 reconstruction** $\log(L_{bayesian1}) + \log(L_{bayesian2}) - \log(L_{SPE32})$: The split Bayesian likelihood ratio compares the hypothesis of a single up-going muon track with the alternative hypothesis of two down-going muon tracks reconstructed with the Bayesian prior defined in eq. 8.21. The two muons were reconstructed either by splitting the DOMs by their geometry or their trigger time as discussed in section 8.2.4. This observable is constructed to reject mis-reconstructed coincident atmospheric muons. As in the single muon case, low values support the alternative hypothesis of two down-going atmospheric muons where as higher values indicate an up-going muon track.

- **minimum zenith angle of a split two muon reconstruction using a geometry splitting** $\theta_{splitgeo}$: Two muons are reconstructed by using the geometry of the triggered DOMs in the event to split them into two groups as discussed in section 8.2.4. The SPE PDF with 16 iterations is used in reconstructing the two muon tracks. This observable requires both reconstructions to pass a

reconstructed zenith angle threshold.

- **minimum zenith angle of a split two muon reconstruction using a time splitting** $\theta_{splittime}$: Two muons are reconstructed by using the trigger time of the DOMs in the event to split them into two groups as discussed in section 8.2.4. The SPE PDF with 16 iterations is used in the reconstruction. This observable requires both reconstructions to pass a reconstructed zenith angle threshold.

- **Number of DOMs with direct photoelectrons,** $NDir$: The number of Čerenkov photons arriving between -15 and $+75$ ns of their expected un-scattered photon arrival times from a reconstructed track is known as the number of direct photons, or $NDir$. More direct photons would decrease the chance of a mis-reconstructed track. $NDir$ is calculated with respect to the MPE likelihood reconstruction.

- **Direct length of the MPE reconstructed track,** $LDir$: The number of direct photons, $NDir$, are projected back on to the reconstructed track. The direct length, $LDir$, is the maximum separation distance between these projected photons.

- **Smoothness of the MPE reconstructed track,** $SDir$: The number of direct photons, $NDir$, are projected back on to the reconstructed track. The smoothness, $SDir$, is a measurement of how uniformly distributed these projected photons are along the reconstructed track. Smoothness runs between -1 and 1. Positive values of smoothness indicate that the projected photons cluster at the beginning of the track, where as negative values of smoothness indicate

there are more at the end of the track. A smoothness that is close to 0 indicates a uniformly distributed distribution of projected Čerenkov photons.

9.3 Final Event Sample

Observable and Selection Criteria
$\theta_{MPE} > 90°$
$\frac{\log(L_{MPE})}{(N_{ch}-5)} < 8$ OR $\frac{\log(L_{MPE})}{(N_{ch}-2.5)} < 7.1$
$\sigma_{MPE} < 3°$
$\log(L_{Bayesian}/L_{SPE32}) > 25$ for $\cos(\theta_{MPE}) < -0.2$
$\log(L_{Bayesian}/L_{SPE32}) > (75\cos(\theta_{MPE}) + 40)$ for $\cos(\theta_{MPE}) > -0.2$
$\log(\frac{L_{Bayesian1}+L_{Bayesian2}}{L_{SPE32}}) > 35$
$\theta_{splittime} > 80°$
$\theta_{splitgeo} > 80°$
$NDir > 5$
$LDir > 240$
$\|SDir\| < 0.52$

Table 9.2: Summary of the analysis level cuts applied to the IceCube data to derive the final event sample for the analysis.

A summary of the analysis level cuts applied to the IceCube data in order to obtain the final neutrino sample is given in table 9.2. The passing rates after successive purity cuts for data and monte carlo for the down-going atmospheric muon background, atmospheric neutrinos, and a hypothetical astrophysical E^{-2} flux are given in Table 9.3. Although these cuts are designed to reject the down-going atmospheric muon background, a subset of these quality criteria are observables dealing with track quality and can be used to select well-reconstructed atmospheric muons. An example dE_{reco}/dX distribution of such high quality atmospheric muons for one day of 40-string data is shown in fig. 9.3.
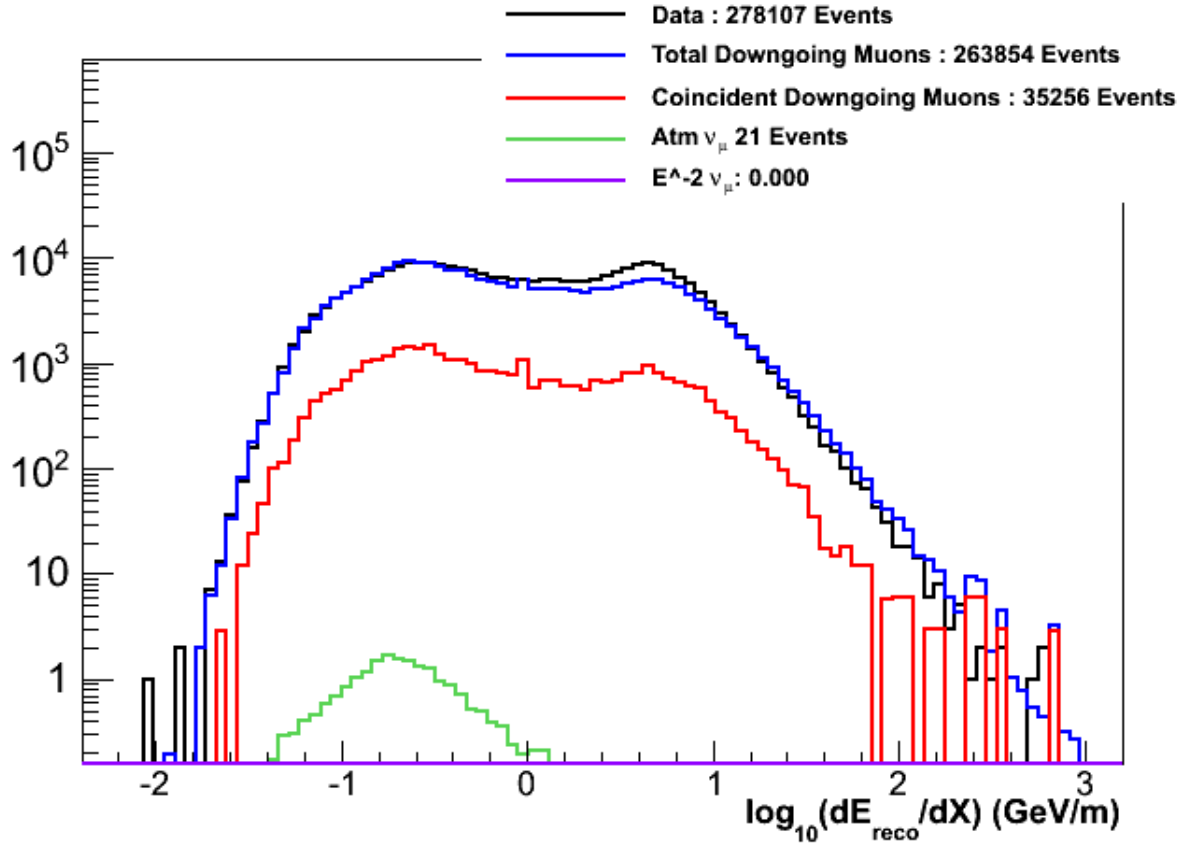
Figure 9.3: Distributions comparing data to simulation for one day of IceCube data for well-reconstructed atmospheric muons. From Table 9.2, the quality cuts on σ_{MPE}, L_{MPE}, $NDir$, $LDir$, and $SDir$ are appied. Mis-reconstructed down-going muons are removed from these plots. Shown is the total sum of Corsika atmospheric muon simulation from single and coincident atmospheric muons, simulated atmospheric ν_μ, and a hypothetical astrophysical E^{-2} ν_μ flux.
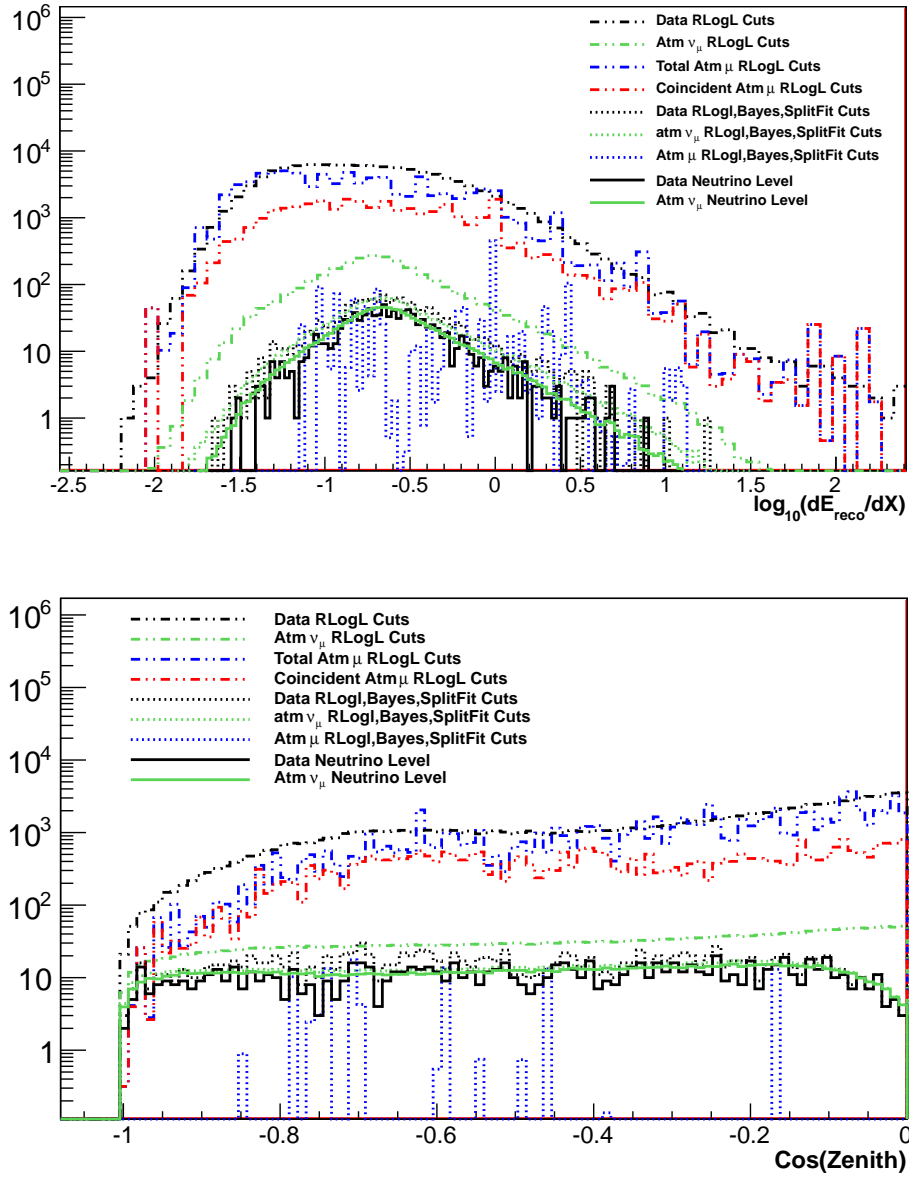
Figure 9.4: dE_{reco}/dX and $\cos(\theta)$ for data, atmospheric muon simulation, and atmospheric neutrino simulation demonstrating the progression from filter level to analysis level. Each set of curves show the dE_{reco}/dX and $\cos(\theta)$ distributions after several stages of quality cuts.

Quality Parameter	Data	Total Atm. μ	Coincident μ	Atm. ν_μ	$E^{-2}\ \nu_\mu$
$\theta_{MPE} > 90°$	19211340	24557460	14318580	7290	100.0%
$\log(L_{MPE})$	675820	365570	89283	3473	69%
σ_{MPE}	114305	83913	32615	2985	50%
$\log(L_{Bayes}/L_{SPE32})$	22981	21842	18920	2195	48.7%
$\log(\frac{L_{Bayes1}+L_{Bayes2}}{L_{SPE32}})$	3550	1925	1436	1490	46.0%
$\theta_{splittime}$	1794	253	188	1284	41.1%
$\theta_{splitgeo}$	1425	94	80	1229	39.3%
$NDir$	1273	61	48	1195	38.7%
$LDir$	1099	43	38	1153	36.9%
$SDir$	1001	0	0	1111	35.1%

Table 9.3: Summary of the passing rates for data, atmospheric muon monte carlo, atmospheric neutrino monte carlo, and a hypothetical astrophysical $E^{-2}\ \nu_\mu$ flux after successive applications of purity cuts. The quality parameter for the purity cut is shown; the cut for each quality parameter is defined in Table 9.2. The passing rate for $E^{-2}\ \nu_\mu$ is quoted as a percentage. Adhering to the blindness procedure, the cuts were derived from the 30 day burn sample as discussed in the text.

We are left with 12877 candidate neutrino events below the horizon for the Ice-Cube 40 string data set after all analysis level cuts have been applied. The selection criteria is designed to reject the large amounts of down-going atmospheric muons while keeping as many neutrino events as possible resulting in an essentially pure (99.9%) event sample. These cuts were designed in particular to maximize the retention efficiency of the simulated E^{-2} astrophysical neutrino flux, which is 35.1% for this analysis. Appendix A contains a discussion on the cut progression for this analysis. A summary of the event selection progression in the dE_{reco}/dX and $\cos(\theta)$ distributions are shown in Fig. 9.4. Event displays for the four highest reconstructed dE/dX events are contained in Appendix B. The distributions of our primary observables and track quality variables at the final analysis level for the full year of the IceCube 40-string data set are shown in figs. 9.5 - 9.9. We note an 8% deficit of atmospheric neutrino

Monte Carlo below data at the horizontal region between 90 and 97 degrees in zenith angle.

9.4   Neutrino Effective Area

The effective area of a neutrino telescope such as IceCube is the area $A_{eff}(E, \theta, \phi)$ of a detector that would have a 100% neutrino detection efficiency. The low interaction cross section of the neutrino makes this effective area much smaller than the physical cross section of the detector. The total number of detected events is given by:

$$N_{events} = \int dE_\nu \ d\Omega \ dt \ \Phi_\nu(E_\nu, \theta, \phi) A_{eff}(E, \theta, \phi) \tag{9.1}$$

This quantity summarizes the efficiency of a particular analysis, which includes the efficiency of the analysis level cuts and physical effects like the absorption due to the Earth. For a detailed discussion of the calculation of the neutrino effective area, see Appendix B of [63]. Fig. 9.11 shows the effective area as a function of energy for this analysis in different zenith angle ranges. Tables of the neutrino effective area for the energies and zenith angle ranges shown in Fig. 9.11 are tabulated in Appendix C for easy reference.
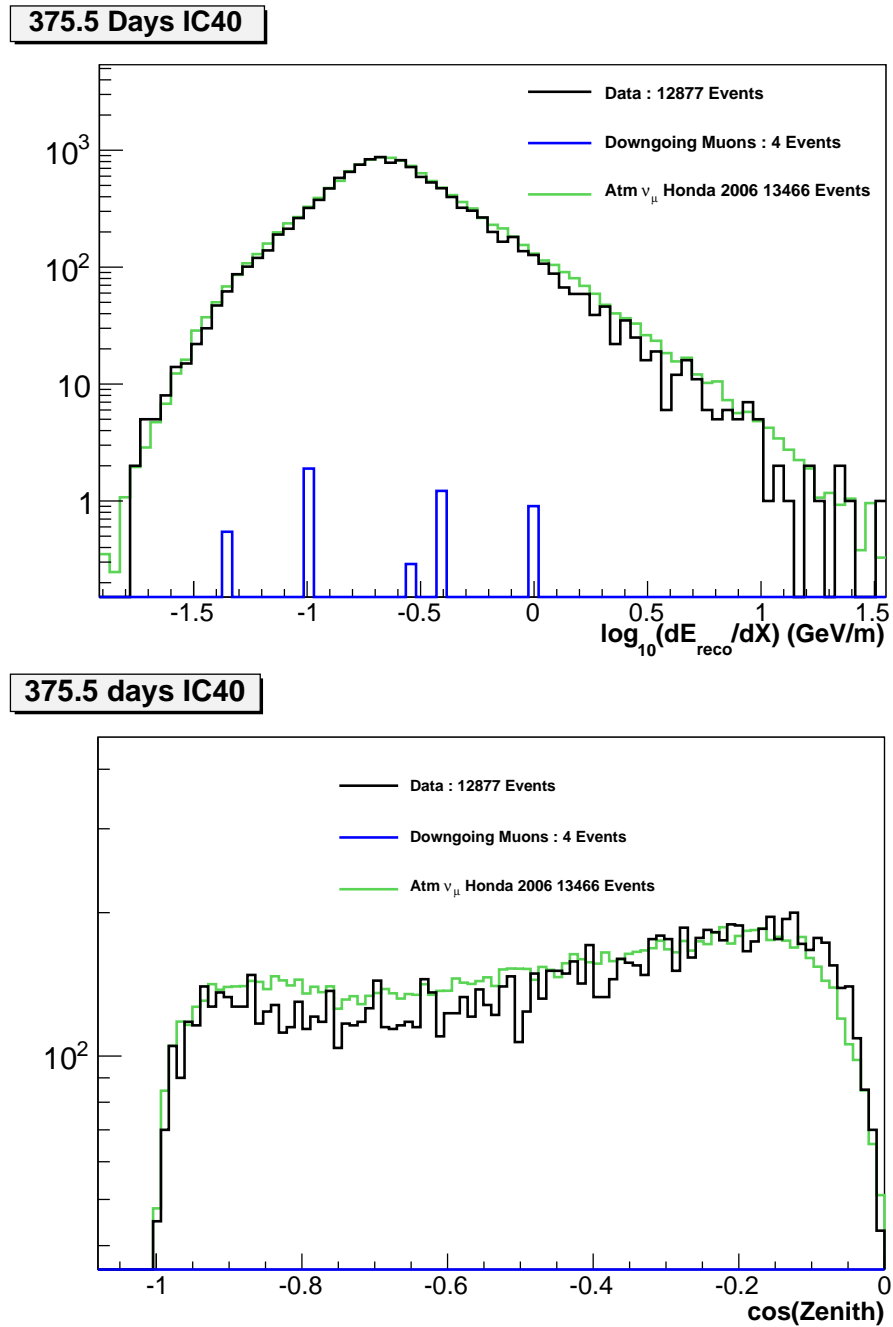
Figure 9.5: dE_{reco}/dX and $\cos(\theta)$ for data and atmospheric neutrino simulation after all quality cuts have been applied.
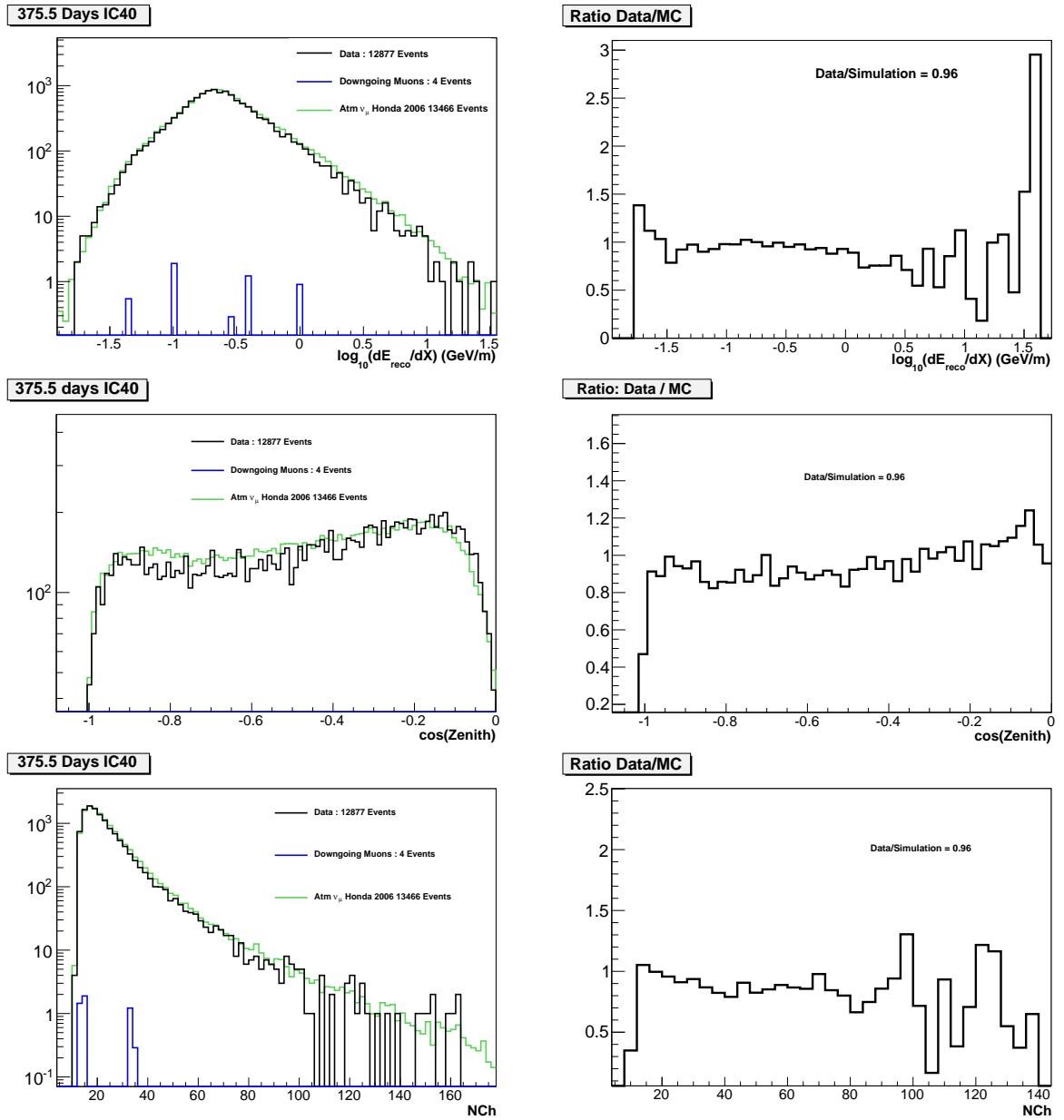
Figure 9.6: Physics observables for data and atmospheric neutrino simulation after all quality cuts have been applied.
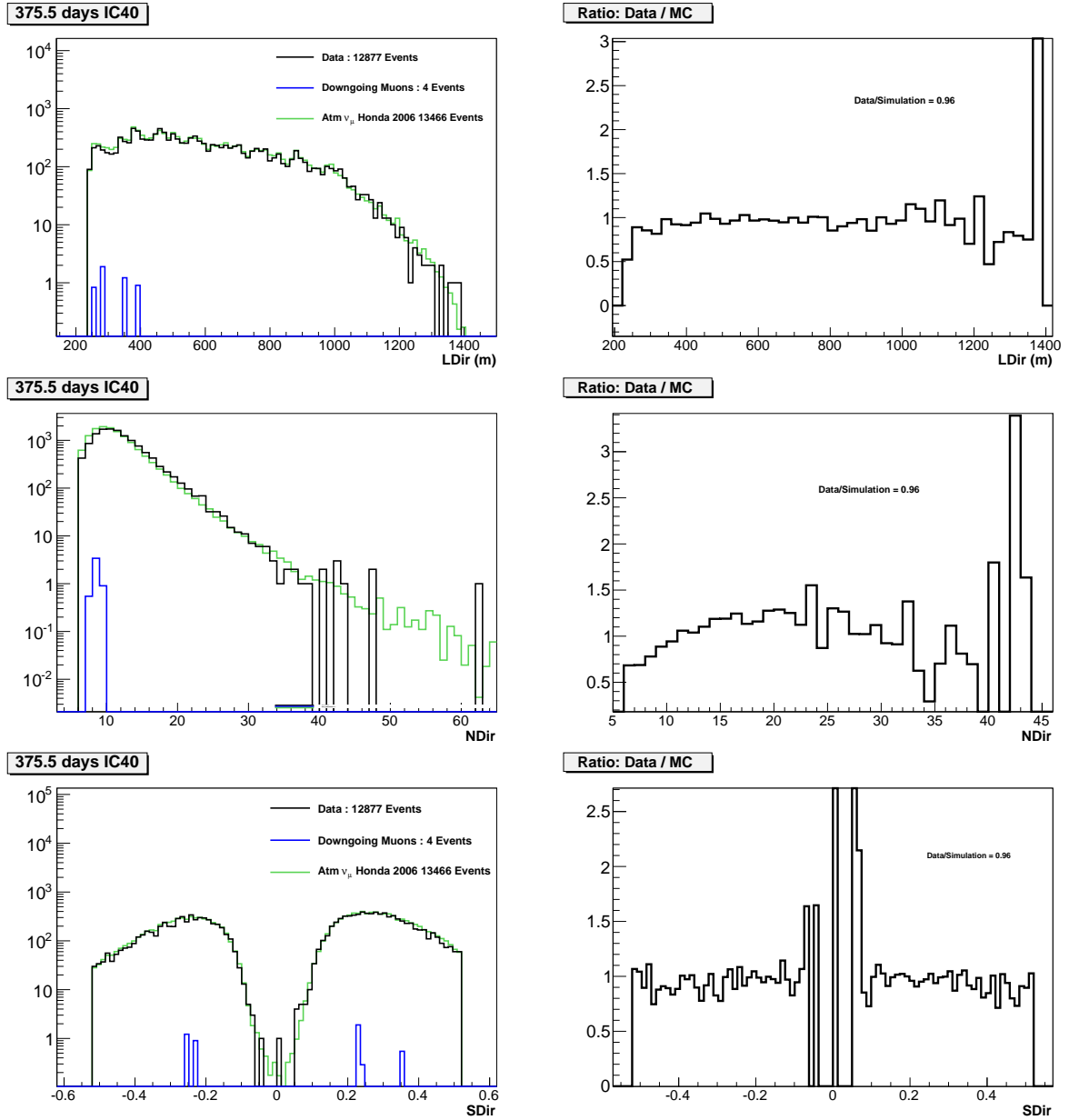
Figure 9.7: Direct hit track quality variables for data and atmospheric neutrino simulation after all quality cuts have been applied.

99
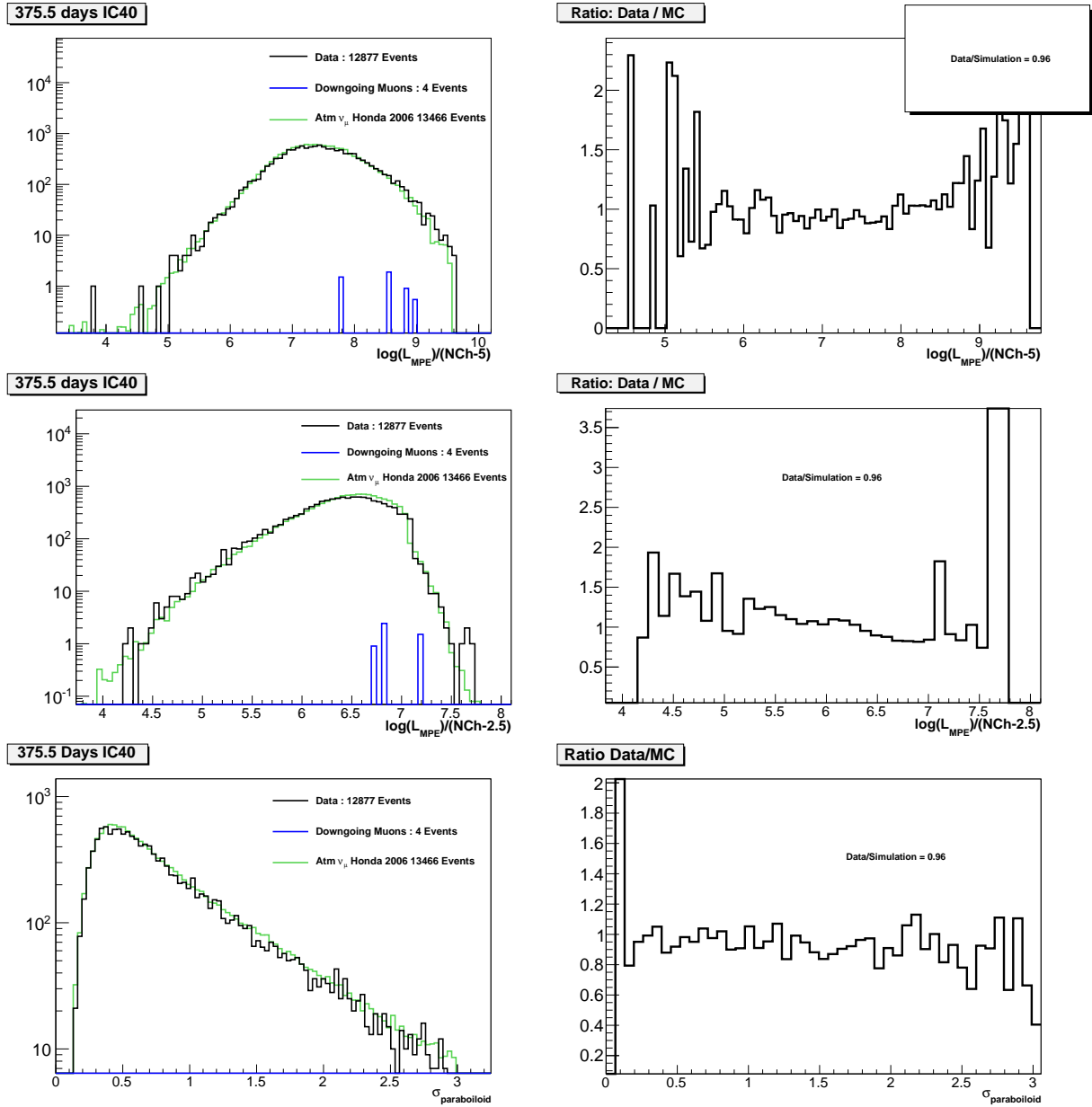
Figure 9.8: Log-likelihood track quality variables for data and atmospheric neutrino simulation after all quality cuts have been applied.
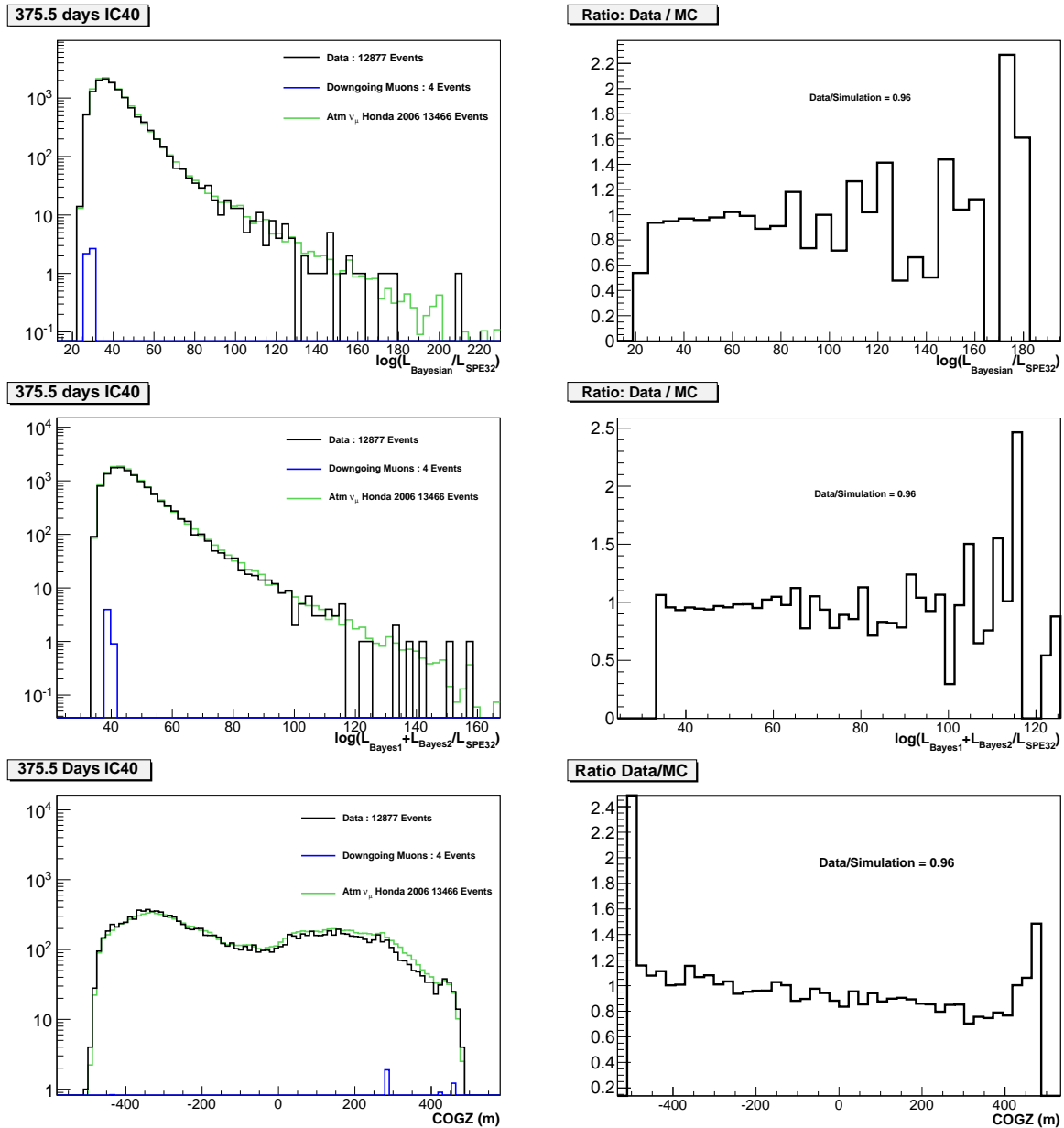
Figure 9.9: likelihood-ratio track quality variables and the Z coordinate of the Center of Gravity of the captured charge for data and atmospheric neutrino simulation after all quality cuts have been applied.
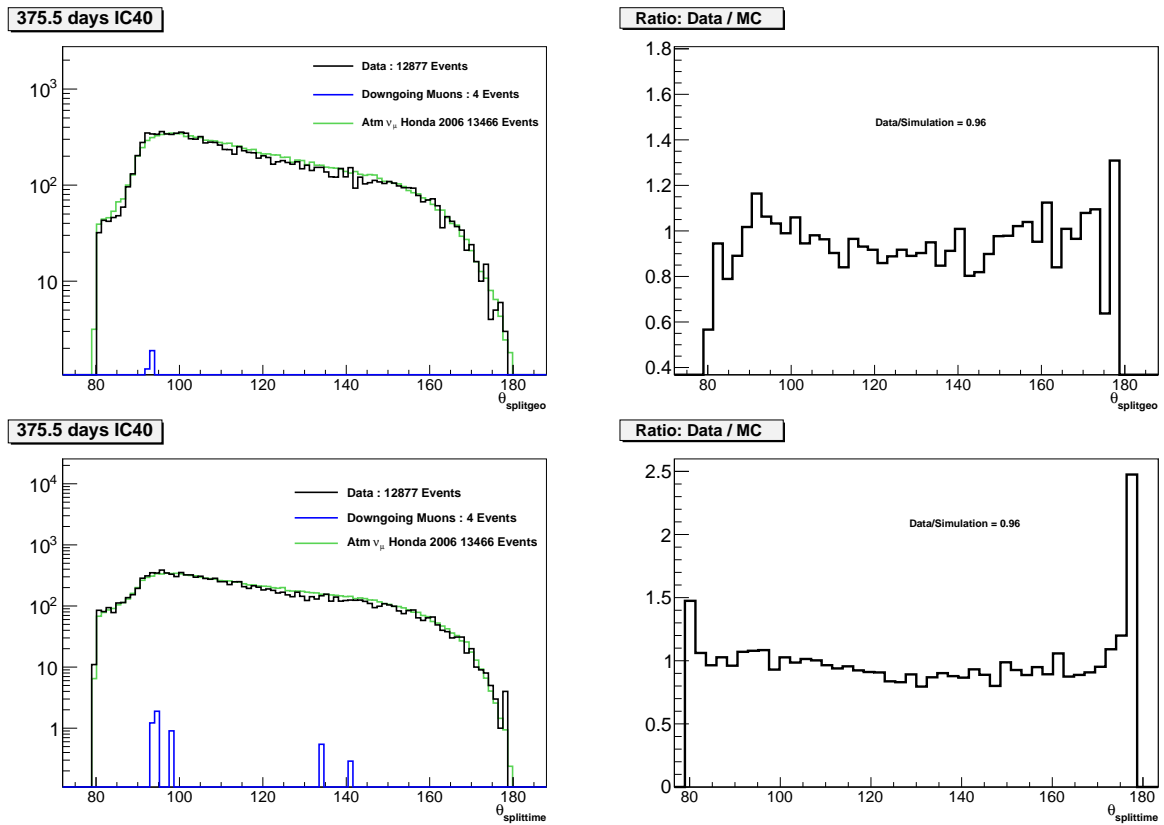
Figure 9.10: Minimum zenith angles of the split fits for data and atmospheric neutrino simulation after all quality cuts have been applied.
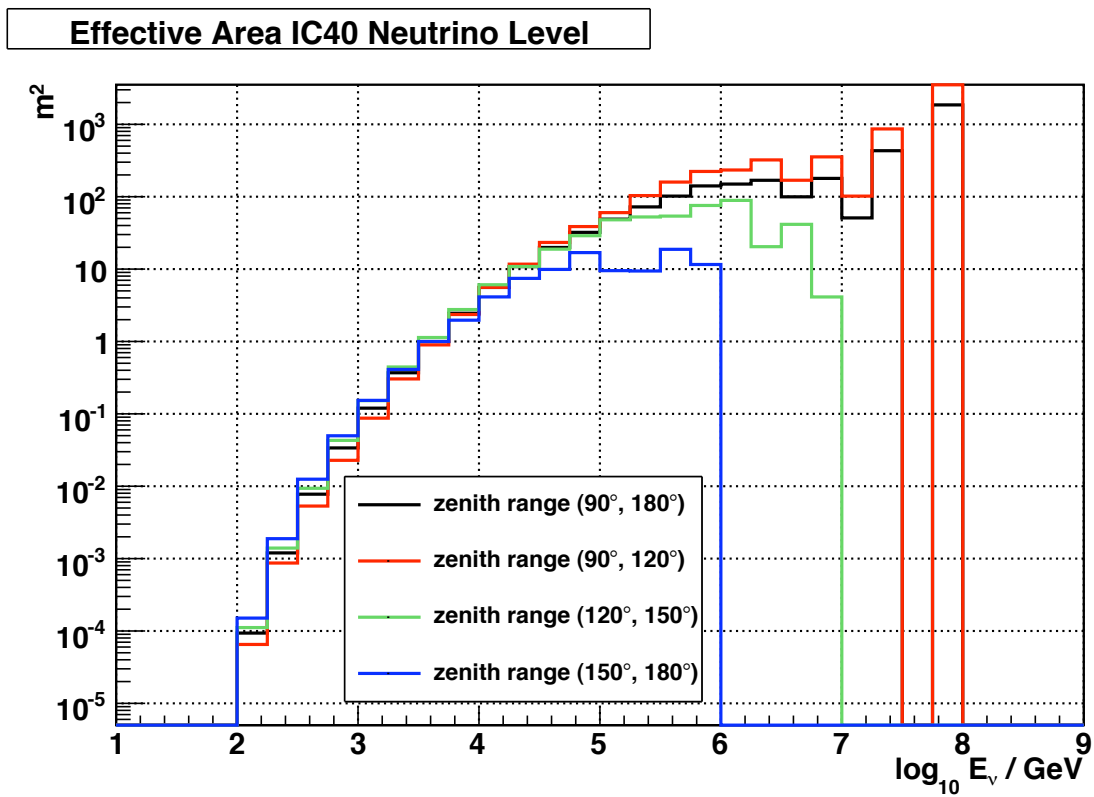
Figure 9.11: Effective area for ν_μ as a function of the true neutrino energy in intervals of the true zenith angle of the neutrino. The angle averaged area is represented by the solid black line.

Chapter 10

Analysis Method

As discussed in chap. 2, evidence for a diffuse astrophysical ν_μ flux would manifest as a hardening of the atmospheric neutrino spectrum in the high energy tail of the energy distribution. The energy of the primary neutrino is not measured in the detector, however, since IceCube only measures the energy loss of the through-going muon. We use the Photorec muon dE/dX reconstruction described in sec. 8.4 for the energy observable in the final analysis.

The simulated energy response of the IceCube 40-string detector to the Honda *et al.* conventional atmospheric neutrino flux [31], the Sarcevic *et al.* prompt atmospheric neutrino flux [33], and a hypothetical astrophysical E^{-2} flux is shown in fig. 10.1. The simulated energy response is shown for the true simulated neutrino energy of events that pass the analysis level purity cuts. The simulated dE_{reco}/dX distribution of this same event sample is shown in fig. 10.2.

10.1 Maximum Likelihood Technique

The goal of this analysis is to quantify how the observed energy distribution of the data is described by the different hypotheses of conventional atmospheric neutri-
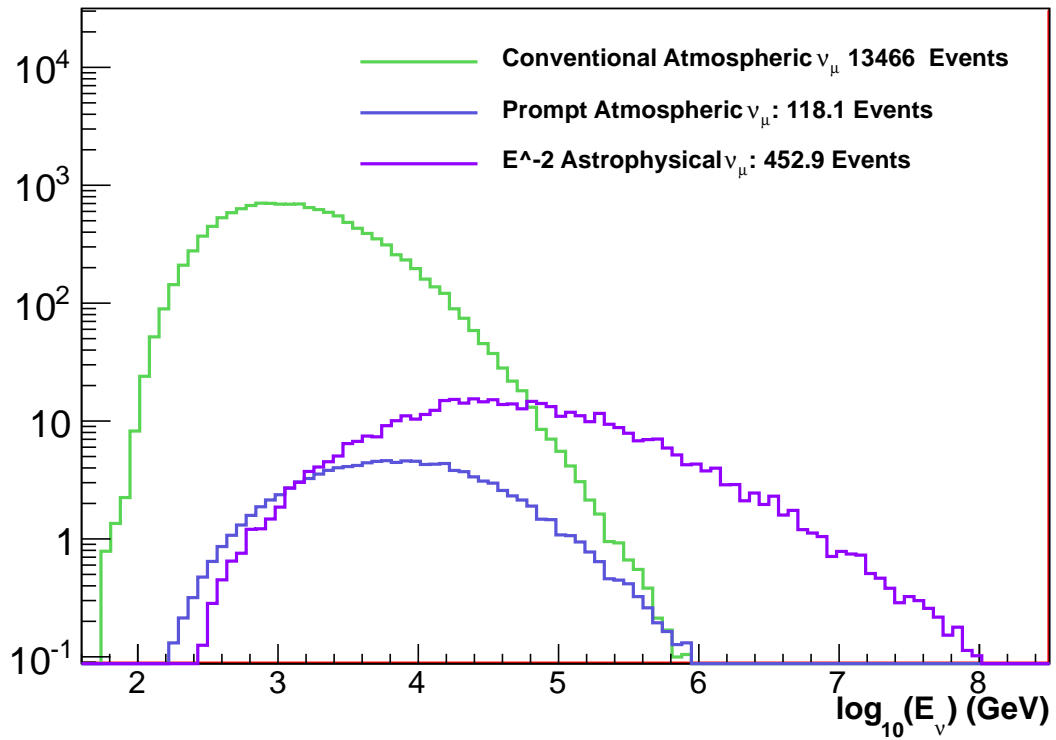
Figure 10.1: Simulated $\nu_\mu + \bar{\nu}_\mu$ energy distribution of the final event sample assuming the Honda input spectrum for conventional atmospheric ν_μ, the Sarcevic Standard model for prompt atmospheric ν_μ, and an astrophysical E^{-2} flux with a normalization of $N = 1.0^{-7} \frac{\text{GeV}}{\text{cm}^2 \text{ s sr}}$.
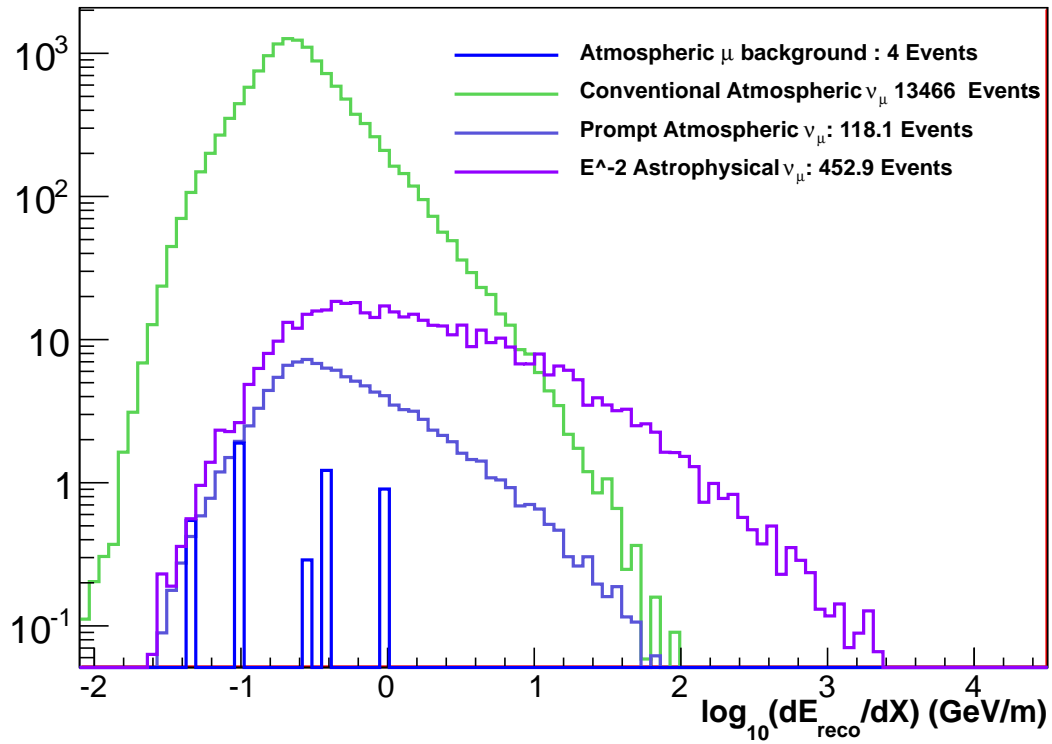
Figure 10.2: Simulated Reconstructed muon energy loss distribution of the final event sample assuming the Honda input spectrum for conventional atmospheric ν_μ, the Sarcevic Standard model for prompt atmospheric ν_μ, and an astrophysical E^{-2} flux with a normalization of $N = 1.0^{-7} \frac{\text{GeV}}{\text{cm}^2 \text{ s sr}}$.

nos, prompt atmospheric neutrinos, and astrophysical neutrinos. A reliable analysis method is needed to determine the contributions from these respective components while incorporating the various sources of systematic uncertainty described in the next chapter. This method should also allow us to construct confidence intervals to determine if a background only hypothesis of atmospheric neutrinos is favored or if the data demonstrates evidence of astrophysical neutrinos.

This chapter describes a frequentist method of using a likelihood function to define central confidence intervals that incorporates systematic errors. This method is an extension of the frequentist approach described by G. Feldman and R. Cousins in [64] and is currently being applied to a wide variety of physics analyses, an example of which is the study of neutrino oscillations [65].

10.1.1 Likelihood Function

A test statistic is needed in order to compare the observed dE/dX distribution for different combinations of the various hypotheses discussed above which are described by physics parameters θ_r. The two physics parameters in this analysis are the absolute normalization of the prompt atmospheric ν_μ flux (since the prompt flux has yet to be measured) and the normalization of a hypothetical astrophysical E^{-2} ν_μ flux. With the dE/dX distribution binned in N bins, we first define a Poisson likelihood function analogous to eq. 8.9:

$$L(\{n_i\}|\{\mu_i(\theta_r)\}) = \prod_{i=1}^{N} \frac{e^{-\mu_i}}{n_i!} \mu_i^{n_i} \tag{10.1}$$

where n_i is the observed event count in the ith bin and μ_i is the expected

event count in the ith bin. The expectation μ_i is the sum of the contributions from conventional atmospheric neutrinos, prompt atmospheric neutrinos, and astrophysical neutrinos. Neglecting sources of systematic uncertainty for the moment, μ_i is defined as:

$$\mu_i = \mu_{c,i} + \mu_{p,i} + \mu_{a,i} \tag{10.2}$$

$$\mu_i = \mu_c p_{c,i} + \mu_p p_{p,i} + \mu_a p_{a,i}$$

where the subscripts c, p, and a stand for conventional atmospheric neutrinos, prompt atmospheric neutrinos, and astrophysical neutrinos respectively. The expected event count in the ith bin for the atmospheric and astrophysical neutrinos is a multiplication of the total expected event count by the PDF of the physics parameter in question. As an example, the term $\mu_a p_{a,i}$ multiplies the total expected number of astrophysical neutrino events by the PDF in the ith bin giving $\mu_{a,i}$. Taking the negative logarithm of eq. 10.1 gives:

$$-2\log L(\{n_i\}|\{\theta_r\}) = 2\sum_{i=1}^{N}(\mu_i - n_i \log \mu_i + \log n_i!) \tag{10.3}$$

The likelihood ratio of two hypotheses H_0 and H_1 is a test statistic that compares the probability that the two hypotheses would give rise to the observed data. Using eq. 10.3 to take the likelihood ratio of hypothesis H_0 to hypothesis H_1 gives:

$$-2\log \frac{L_0}{L_1} = 2\sum_{i=1}^{N}\left(\mu_{0,i} - \mu_{1,i} + n_i \log \frac{\mu_{1,i}}{\mu_{0,i}}\right) \tag{10.4}$$

where $\mu_{1,i}$ is the expected event count from the hypothesis H_1 in the ith bin and

$\mu_{0,i}$ is the expected event count from the hypothesis H_0 in the ith bin. The additional factor of 2 in eq. 10.3 arises because Wilks's theorem states that, in the asymptotic regime, a likelihood ratio approaches a χ^2 distribution with the number of degrees of freedom equal to the number of parameters described by θ_r [66].

The likelihood ratio in our analysis is constructed to compare an alternative hypothesis at some physics point θ_r to the hypothesis that best describes the data. The hypothesis that best describes the data is the value of θ_r that minimizes the negative log-likelihood (thereby maximizing the probability) and is denoted by $-2 \log \hat{L} = -2 \log L(\hat{\theta}_r)$. Our test statistic is the likelihood ratio of a point in physics space θ_r to the likelihood of the best fit value:

$$R = -2 \log \frac{L(\theta_r)}{\hat{L}} \tag{10.5}$$

This test statistic allows us to construct confidence intervals for our physics parameters θ_r.

10.1.2 Confidence Intervals

When an observable is reconstructed from the data, one wants to determine the physically allowed hypotheses and construct confidence intervals for the physics parameters θ_r. In this analysis, we wish to construct confidence intervals for the prompt atmospheric neutrino normalization and the astrophysical E^{-2} normalization from the observed dE/dX distribution. Wilks's theorem is often used to define confidence intervals with a χ^2 distribution. The likelihood ratio for the data $R_{data}(\theta_r)$ (eq. 10.5) is calculated at every point θ_r. The point is physically allowed if $R_{data}(\theta_r)$ is less than

some critical likelihood ratio value R_{crit} which is given by the χ^2 distribution. The physically allowed region for a given confidence level α is the set:

$$\{\theta_r\}_\alpha = \{\theta_r | R(\theta_r) < R_{crit}\} \tag{10.6}$$

$$R_{crit} = \chi^2(\alpha, k)$$

The chi-square distribution is a function of the confidence level α and the number degrees of freedom k. For two physics parameters and a 90% confidence level, $R_{crit} = 4.61$. The physically allowed region for θ_r is the region where $R_{data}(\theta_r) < 4.61$. This method of constructing confidence intervals is known as the *global scan* method.

The χ^2 approximation has several disadvantages as discussed in [64]. $R(\theta_r)$ can deviate from the χ^2 distribution by a significant amount if there is a region in the physics parameter space θ_r that has little affect on the observable or if there are large statistical fluctuations in the observable. This reduces the effective degrees of freedom of θ_r and confidence intervals constructed from the χ^2 distribution do not give proper coverage. This is especially true in this analysis since a search for an astrophysical ν_μ flux is dominated by the high energy tail of the atmospheric neutrino distribution which undergo large statistical fluctuations. One is therefore not in the asymptotic regime and the use of the χ^2 approximation is not appropriate. The approach outlined in [64] solves this problem and takes other issues into account in order to achieve proper frequentist coverage. The method entails calculating R_{crit} exactly using the following steps:

- Each point in the physics parameter space θ_r is scanned in order to calculate

the critical value of the likelihood ratio at confidence level α. (R_{crit} is now a function of the physics parameters, $R_{crit}(\theta_r)$.)

- For each point in θ_r, a number of Monte Carlo experiments are performed by sampling from the parent distribution $\{x|\theta_r\}$ to generate the experimental trial. The sampling can be achieved by selecting the total number of events N from a Poisson distribution with μ equal to the integral of the parent distribution and then sampling N times from the parent observable distribution to find the observables for the trial.

- The likelihood ratio R is calculated for each experimental trial. This gives a distribution of likelihood ratios that undergo only statistical variations.

- Once all experimental trials are performed at point θ_r, a confidence interval at confidence level α can be constructed. The critical value of the likelihood ratio R_{crit} of the point θ_r at confidence level α is given by:

$$\left(\int_0^{R_{crit}(\theta_r)} R_i(\theta_r) \right) / \left(\int_0^\infty R_i(\theta_r) \right) = \alpha \tag{10.7}$$

- The likelihood ratio from the data $R_{data}(\theta_r)$ is compared to $R_{crit}(\theta_r)$. The point is physically allowed if $R_{data}(\theta_r) < R_{crit}(\theta_r)$. The physically allowed region for a given confidence level α is the set of θ_r defined in eq. 10.6 using $R_{crit}(\theta_r)$ defined in eq. 10.7 instead of the χ^2 distribution.

10.2   Profile Likelihood

The method originally outlined in [64] does not take into account any source of systematic uncertainty. Statistically, a systematic error can be treated as a *nuisance parameter* which is a parameter not of immediate interest but must be accounted for in the analysis of the physics parameters. The classic example of a nuisance parameter is the variance σ^2 of a normal distribution when the mean μ is of primary interest. This changes the formulation of the likelihood function 10.3, which now becomes a function of not only the physics parameters θ_r, but also of the nuisance parameters θ_s.

In determining the physically allowed hypotheses in the final analysis, one needs to construct confidence regions in the physics parameter space described by θ_r while incorporating systematic errors parametrized by θ_s and maintaining proper frequentist coverage. This requires a modification to the Feldman-Cousins procedure used to calculate R_{crit} (eq. 10.7) outlined in the last section.

The incorporation of systematic errors into the construction of confidence intervals is an active area of research, and there is no general solution to the problem. The most general frequentist solution involves a Neyman construction of confidence intervals with the goal of covering the physics parameter of interest for every value of the nuisance parameters [67]. This method is computationally prohibitive, and there is not a general consensus on an ordering principle. The nuisance parameters could also be averaged over using a hybrid Bayesian-frequentist method for constructing confidence intervals which is summarized in [68].

The procedure used in this analysis uses the *profile likelihood* [69] as a test statistic in constructing confidence intervals. The profile likelihood is a an approximation

to the likelihood ratio that uses values for the nuisance parameters θ_s that fit the data the best at some physics point θ_r. This provides a worst case scenario for the values of θ_s while maintaining proper frequentist coverage for the values of the physics parameters. The profile likelihood is defined as:

$$R_p = -2 \log \frac{L(\theta_r, \hat{\hat{\theta}}_s)}{L(\hat{\theta}_r, \hat{\theta}_s)} \tag{10.8}$$

where the denominator is the global minimum to the likelihood function and the numerator is a conditional minimum of the likelihood function. The conditional minimum is found by fixing θ_r, but varying the nusiance parameters to find the values $\hat{\hat{\theta}}_s$ that minimize the likelihood function. The physics and nuisance parameters are both varied to find the global minimum of the likelihood with values $(\hat{\theta}_r, \hat{\theta}_s)$.

The profile likelihood is widely used in physics analyses in combination with the χ^2 approximation in the *MINOS* method in the MINUIT suite [70]. This analysis uses the suggestions of Feldman [71] to extend the Feldman-Cousins procedure described in the last section in order to use the profile likelihood to incorporate systematic errors in the non asymptotic regime. This method is often called the *profile construction* method. The key to the method is fixing the values of the nuisance parameters to the best fit value from the data, which makes $R_{crit,p}$ a function only of the physics parameters θ_r and not θ_s. The profile construction method is summarized below:

- The test statistic is the profile likelihood R_p defined in eq. 10.8.

- The profile likelihood for the data $R_{p,data}$ is calculated at each point θ_r. The numerator is a conditional minimum at $(\theta_r, \hat{\hat{\theta}}_s)$ and the denominator is the global

minimum at $(\hat{\theta}_r, \hat{\hat{\theta}}_s)$.

- $R_{p,crit}$ is calculated at the point θ_r by first performing a number of Monte Carlo experiments. Each Monte Carlo experiment is sampled from the parent distribution $\{x | \theta_r, \hat{\hat{\theta}}_s\}$ to generate the experimental trial. Note that $\hat{\hat{\theta}}_s$ is fixed from the fit to the data.

- The profile likelihood R_p is calculated for each experimental trial, giving a distribution of profile likelihood values.

- Once all experimental trials are performed at point θ_r, $R_{p,crit}$ at confidence level α can be calculated using eq. 10.7.

- The profile likelihood from the data $R_{p.data}(\theta_r)$ is compared to $R_{p,crit}(\theta_r)$. The hypothesis is physically allowed if $R_{p,data}(\theta_r) < R_{p,crit}(\theta_r)$ for a given confidence level α.

- The above procedure is repeated for every value of θ_r.

- The set of all allowed hypotheses gives the physically allowed region at confidence level α.

The profile construction method described in this chapter allows us to reliably search for a diffuse astrophysical ν_μ flux while taking into account the various sources of systematic uncertainty described in the next chapter. The same methodology is also used to search for evidence of an atmospheric prompt ν_μ flux and to reconstruct the conventional atmospheric ν_μ spectrum.

Chapter 11

Systematic Errors

Systematic errors represent uncertainties in fundamental quantities that lead to unknown variations in the observables x that do not randomly vary from measurement to measurement. These quantities can describe uncertainties in the underlying physics such as the absolute normalization of the flux of conventional atmospheric neutrinos or detector effects such as the absolute sensitivity of the DOMs. It is important to accurately model the sources of systematic uncertainty in order to determine how they affect the measured result. A proper treatment of systematic errors is critical for this analysis since the observed energy distribution is quite sensitive to various sources of systematic uncertainty. Reliable modeling of the systematic errors allows their incorporation into the final analysis as nuisance parameters. This enables the use of the profile construction method discussed in sec. 10.2, which results in confidence intervals that approximately have proper frequentist coverage for the physics parameters of interest as discussed in [71].

11.1 Conventional Atmospheric Neutrino Flux

One of the largest sources of systematic uncertainty is the overall normalization of the conventional atmospheric neutrino flux. The baseline model for conventional atmospheric neutrinos used in this analysis is the model derived by Honda *et al.* [31]. The uncertainty in the absolute normalization of the atmospheric neutrino flux from this model is $\pm 25\%$. Fig 11.1 compares the conventional atmospheric flux prediction from Honda *et al.* to another atmospheric neutrino prediction from Barr *et al.* [30].
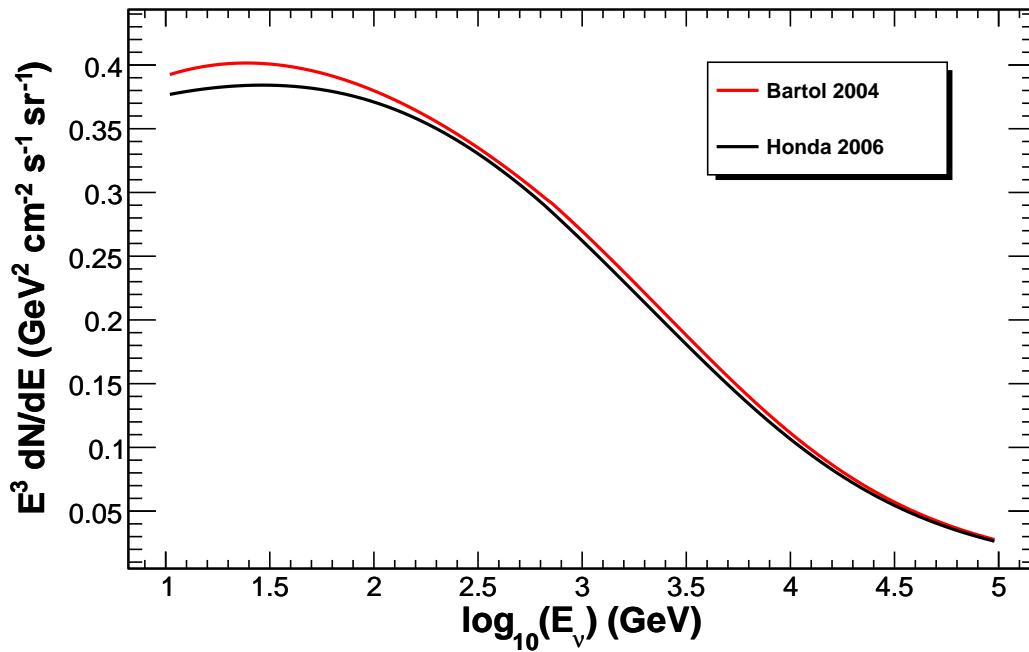
Figure 11.1: Predicted conventional atmospheric neutrino fluxes averaged over zenith angle and multiplied by E^3 to enhance features.

A major source of systematic uncertainty affecting only the conventional atmospheric neutrino flux is the relative contribution from pions and kaons to the total flux. The general dependence of the π/K ratio is shown in fig. 11.2. This source

of systematic uncertainty mainly affects the zenith angle distribution of atmospheric neutrinos and therefore is not incorporated into this analysis.
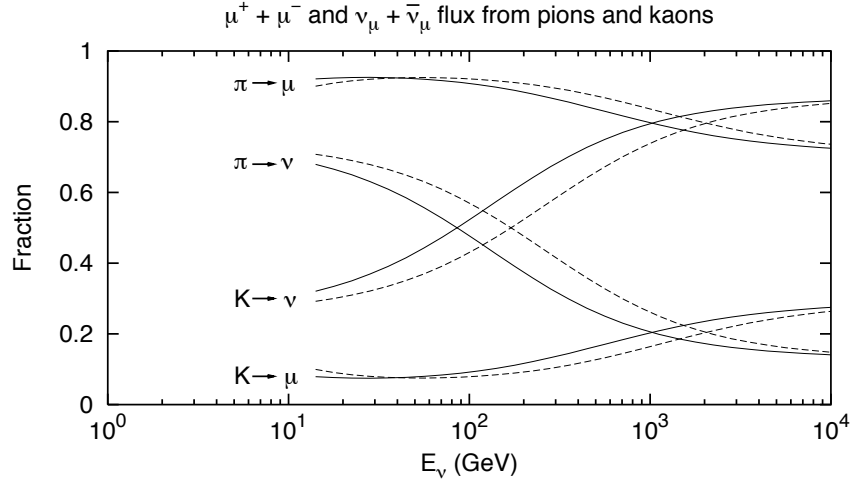
Figure 11.2: Relative contribution from pions and kaons to atmospheric muons and muon neutrinos. Solid is vertical, dashed is 60°. Taken from [72].

11.2   Prompt Atmospheric Neutrino Flux

The Honda *et al.* conventional atmospheric neutrino model only considers neutrinos produced from charged pion and kaon decay. At high energies, charmed mesons such as D^+, D^-, D_s and others can be produced. These charmed mesons decay almost immediately, which is why the atmospheric neutrino flux from the decay of charmed mesons is often called the prompt atmospheric neutrino flux. The prompt component is a critical source of systematic uncertainty since it is predicted to contribute to the atmospheric neutrino flux at high energies, which is also the signal region for this analysis.

This particular source of systematic uncertainty is also a challenge since the prompt component of the atmospheric neutrino flux has yet to be measured and the theoretical uncertainties in the normalization are large. Fig. 11.3 shows the range of predictions from a variety of models. The Naumov RQPM (Recombination Quark Parton Model) [34] is a non-pertubative calculation of the atmospheric neutrino flux from charmed decay and provides a conservative prediction for the prompt component. The Sarcevic *et al.* model [33] uses a perturbative QCD approach that incorporates results from HERA data in the calculation to predict a range of possible prompt atmospheric neutrino fluxes. The Martin *et al.* model [35] is another perturbative QCD model that predicts a normalization lower than the other models. The baseline model used in this analysis is the standard prediction from Sarcevic *et al.*. The uncertainty in the model is shown in Fig 11.3, where the higher prediction is 25% higher than the standard calculation and the lower prediction is 44% lower than the standard calculation.

11.3   Primary Cosmic Ray Slope

The uncertainty in the spectral slope of the primary cosmic ray spectrum leads to an uncertainty in the spectral slope of the atmospheric neutrino flux. Although the spectral shapes of the conventional and prompt components of the atmospheric neutrino flux are predicted to be different, a change in the primary cosmic ray spectral slope would change both components by the same amount. The uncertainty in the primary cosmic ray spectrum can be estimated by considering the uncertainty in the spectral slopes of cosmic ray protons (which comprise 79% of the flux) and of helium nuclei (15% of the flux). Gaisser *et al.* [73] estimates the spectral slope uncertainty for
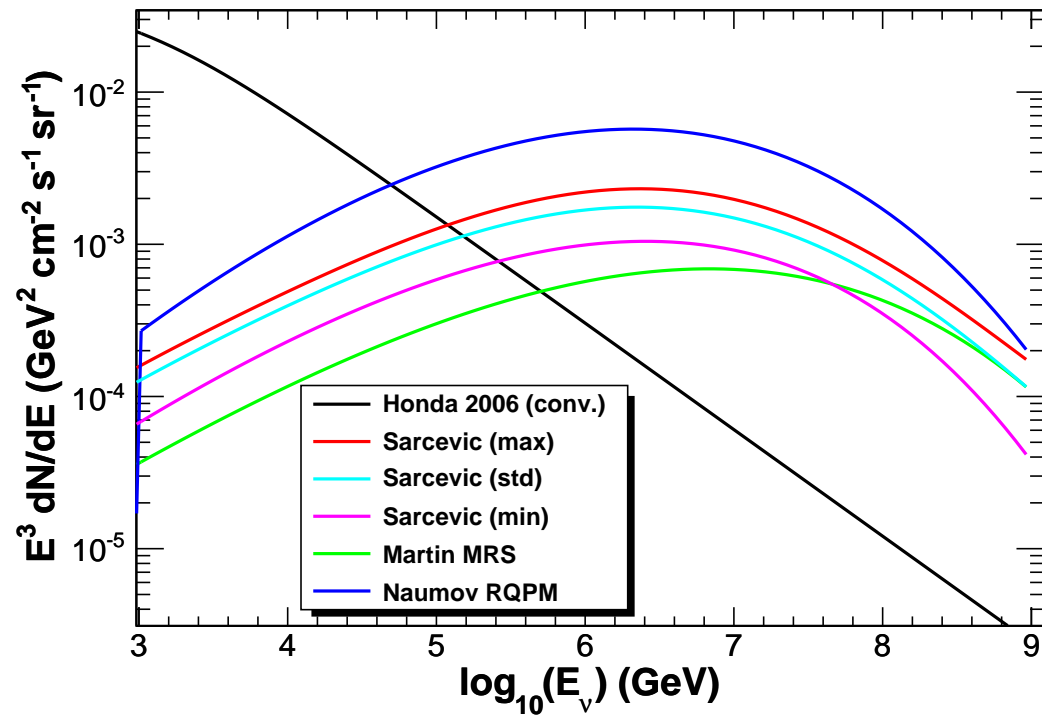
Figure 11.3: Predicted prompt atmospheric neutrino fluxes averaged over zenith angle and multiplied by E^3 to enhance features. The Honda 2006 model is shown for comparison.

protons to be ± 0.01 and for helium nuclei to be ± 0.07. Scaling the individual spectral index uncertainties by the fraction of the total flux for the respective component gives an uncertainty in the primary cosmic ray spectral slope of ± 0.03. The effect of this uncertainty on the reconstructed dE/dX distribution is shown in fig. 11.4.
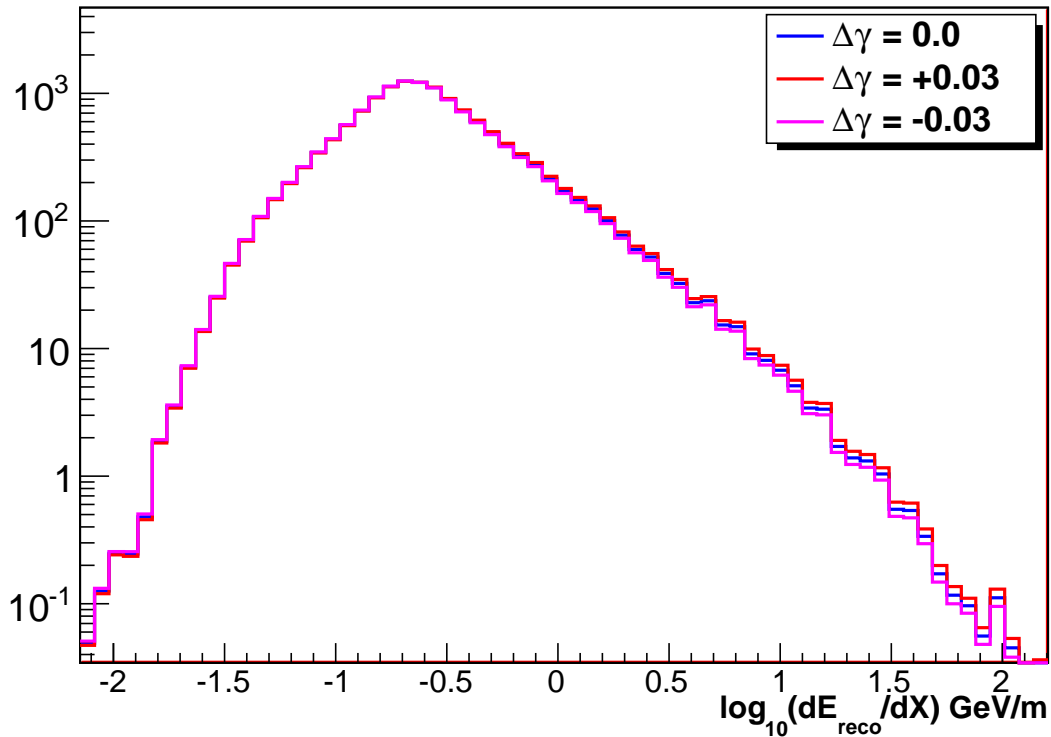
Figure 11.4: The simulated effect of the cosmic ray slope uncertainty $\Delta\gamma$ on the observed dE/dX distribution for atmospheric neutrinos.

11.4 Digital Optical Module Sensitivity

One of the main sources of systematic uncertainty in the response of the IceCube detector is the uncertainty in the absolute sensitivity of the digital optical module. This uncertainty has a large effect on the overall event rate; a change in the absolute

sensitivity of 1% for example leads to a corresponding 2% change in the event rate. The uncertainty is quantified in [74], which is measured to be $\pm 7.7\%$. The absolute sensitivity is further reduced by a shadowing effect from the main cable and the magnetic shield in the DOM [75], which reduces the sensitivity by 6.96%. The simulated effect of the uncertainty in the absolute DOM sensitivity is shown in fig. 11.5.
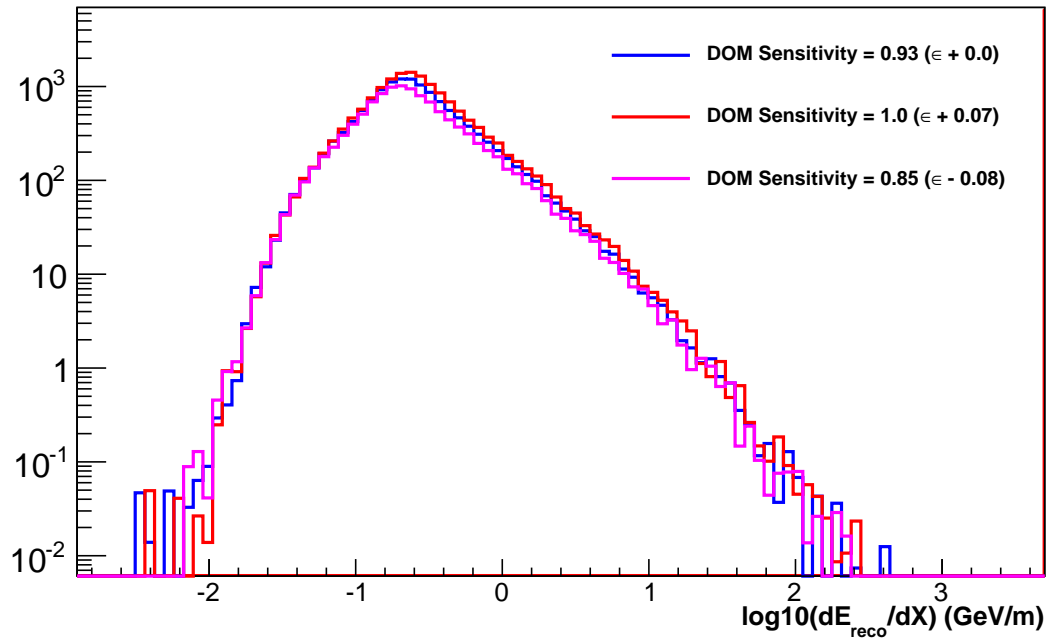
Figure 11.5: The simulated effect of the uncertainty in the DOM sensitivity ϵ on the observed dE/dX distribution for atmospheric neutrinos. The DOM sensitivity is reduced by 6.96% due to the shadowing effects described above, giving a central value for the absolute sensitivity of 0.93.

11.5 Ice Properties

The other main source of systematic uncertainty due to the response of the IceCube detector is the uncertainty in the measured properties of the glacial ice at the South Pole. The uncertainty in the measured scattering and absorption coefficients

affects not only the overall event rate, but also the shape of the reconstructed energy distribution. This analysis incorporates the latest developments in the South Pole Ice Model (or SPICE model) described in [50]. The measured uncertainty in the scattering and absorption coefficients of the south pole ice is measured to be $\pm 10\%$ at a flasher LED wavelength of 405 nm. The simulated effect of the uncertainty in the scattering and absorption is shown in fig. 11.6.
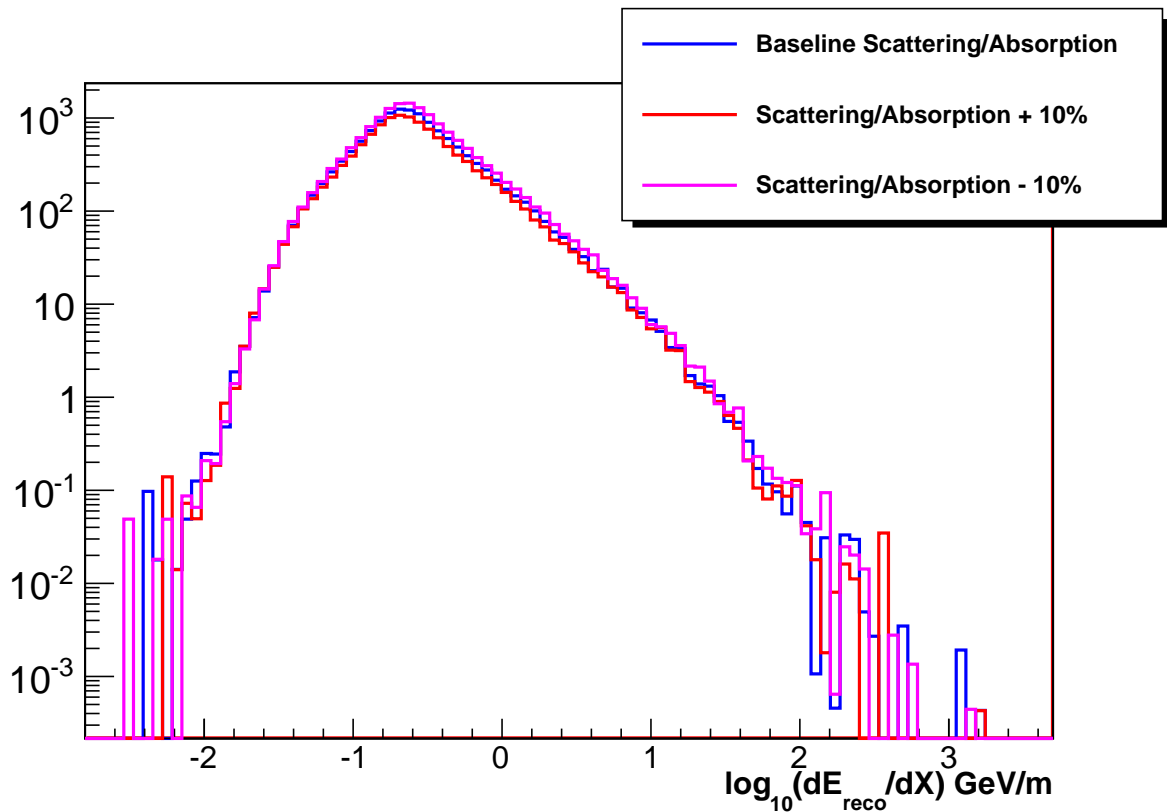
Figure 11.6: The simulated effect of the uncertainty in the ice properties on the observed dE/dX distribution for atmospheric neutrinos. The uncertainty in the ice properties are described by the effective scattering coefficient b_e and the absorption coefficient a measured at a LED wavelength of 405 nm.

11.6 Other Sources of Systematic Uncertainty

There are other sources of systematic uncertainties in the underlying physics and detector response that are relatively minor compared to the sources discussed above, but are summarized here.

11.6.1 Neutrino Interaction Cross Section and Muon Energy Loss

At the TeV energy scale, the uncertainties in the deep inelastic neutrino cross section and the muon energy loss cross sections are quite small. The uncertainty in the charged current, deep-inelastic neutrino-nucleon cross section was calculated in [76] to be $\pm 3\%$ using the parton distribution function error tables from [37] and the error calculation prescription in [77]. The 3% uncertainty in the cross section corresponds to a 3% uncertainty in the overall neutrino event rate since the effective area (eq. 9.1) is a linear function of the neutrino cross section. The uncertainty in the muon energy loss cross sections is estimated from [39] to be 1%. This has a negligible effect on the total event rate and the observed dE_{reco}/dX distribution as shown in fig. 11.7.

11.6.2 Tau neutrino-induced Muons

For the atmospheric neutrino background, ν_τ-induced muons are negligible since mass-induced oscillations are unimportant above the energy threshold of the IceCube detector which is about 100 GeV. For astrophysical neutrinos, however, the models considered in ch. 2 predict a flavor ratio at the source of $\nu_\mu : \nu_e : \nu_\tau = 2 : 1 : 0$, which oscillates to a flavor ratio of $\nu_\mu : \nu_e : \nu_\tau = 1 : 1 : 1$ at Earth. The ν_τ flux can interact, generating a τ daughter lepton which subsequently decays to a muon. The branching ratio of $\tau \to \mu \nu_\mu \nu_\tau$ is 17% [27] and these muons need to be taken into account when
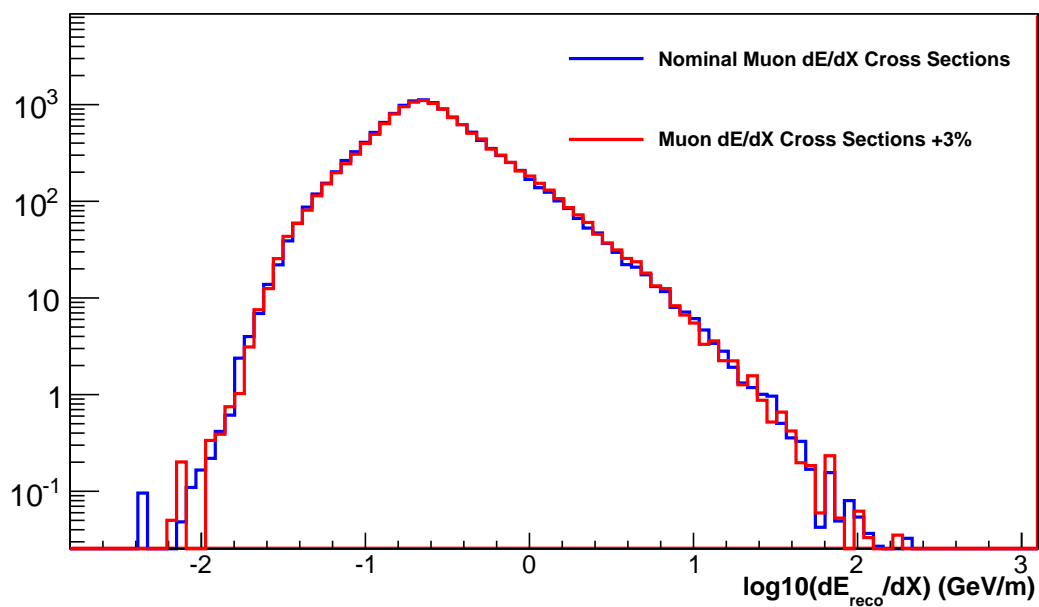
Figure 11.7: The simulated effect of the uncertainty in the muon energy loss cross sections on the observed dE/dX distribution for atmospheric neutrinos. The ionization, photo-nuclear, bremsstrahlung, and pair-production cross sections were varied in the simulation.

quoting an all-flavor limit for astrophysical neutrinos.

To estimate the flux, we generate a sample of tau neutrinos with the neutrino generator package and weight them to an E^{-2} spectrum with an astrophysical normalization of $N = 1.0^{-7}$ GeVcm^{-2}s^{-1}sr^{-1}. The simulated energy distribution of the ν_τ contribution is shown in fig. 11.8. The number of ν_τ induced muons at our final purity level is 59 events compared with the expectation from ν_μ of 452 events at this normalization. The simulated zenith and dE_{reco}/dX distributions of the ν_τ contribution is shown in Fig. 11.8.

11.6.3 Rock Density

The uncertainty in the density of the bedrock under the polar ice is 10% [78]. This provides a negligible difference in the atmospheric neutrino event rates of < 0.1%, since the increase in the neutrino interaction probability is offset by a corresponding decrease in the range of the muon.

11.6.4 Background Contamination

The background contamination in the final event sample is estimated to be less than 1% , and is therefore a negligible source of systematic uncertainty in the analysis. This is estimated from the mis-reconstructed atmospheric muon background that survive the analysis level cuts.

11.7 Summary and Final Analysis Parameters

With the previously discussed sources of systematic uncertainty parameterized as nuisance parameters, the profile likelihood construction method discussed in ch. 10.2
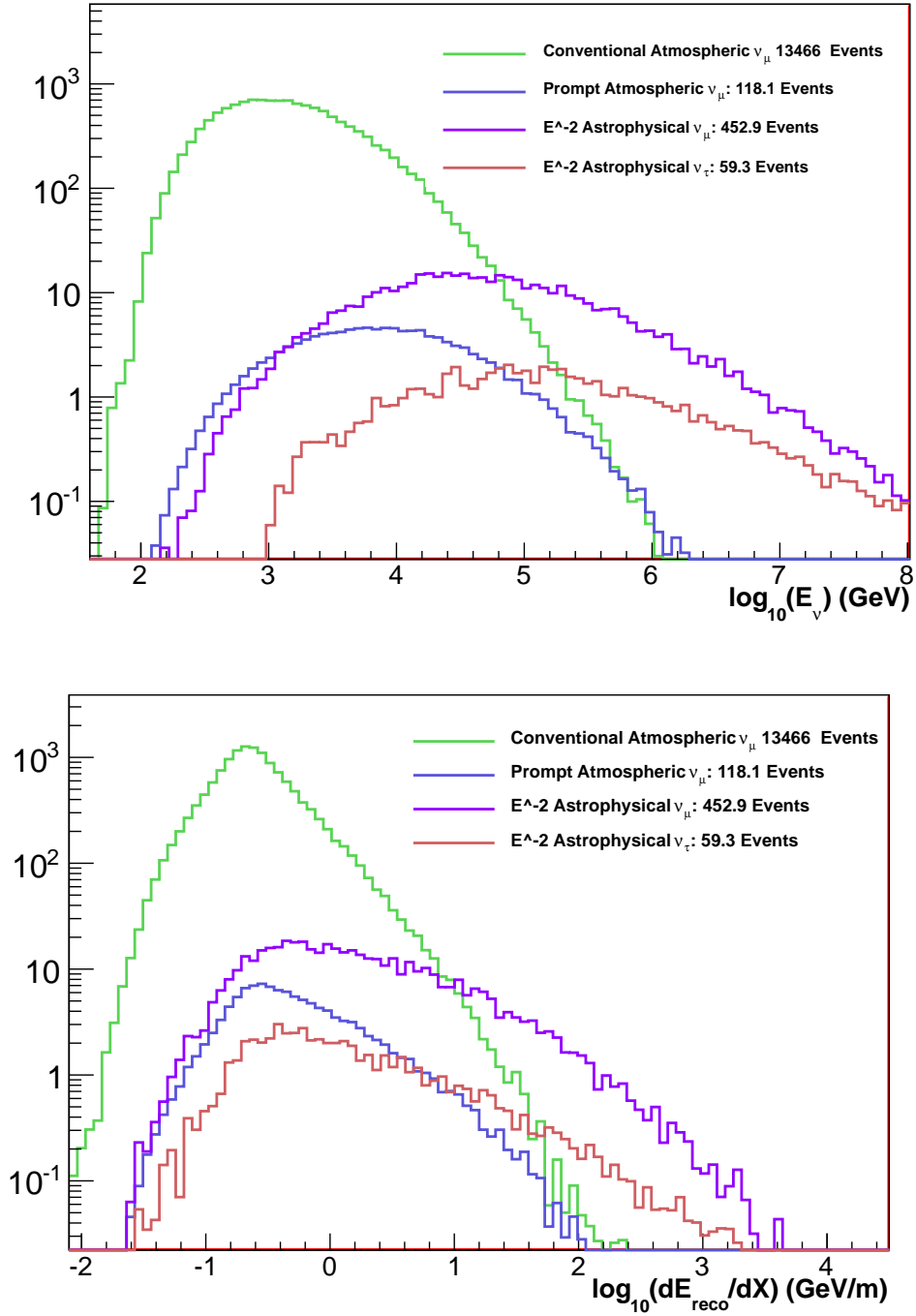
Figure 11.8: Simulated contribution of the $\nu_\tau + \bar{\nu}_\tau$ contribution to the energy distribution of the final muon event sample assuming an astrophysical E^{-2} flux with a normalization of $N = 1.0^{-7} \ GeV \, cm^2 s^{-1} sr^{-1}$. The top plot shows the MC neutrino energy, and the bottom plot shows the simulated dE_{reco}/dX distribution of the muon.

can be used. The sources of systematic uncertainty and their corresponding nuisance parameters are summarized in Table 11.1.

Table 11.1: Summary of Nuisance Parameters

Systematic Uncertainty	Nuisance Parameter	Magnitude
Conventional Atmospheric ν_μ Normalization	$1 + \alpha_c$	$\pm 25\%$
Prompt Atmospheric ν_μ Normalization	$1 + \alpha_p$	$-44\%, +25\%$
Cosmic Ray Spectral Slope	$\Delta\gamma$	± 0.03
Detector Efficiency	ϵ	$\pm 8.3\%$
Scattering Coefficient	$b(405)$	$\pm 10\%$
Absorption Coefficient	$a(405)$	$\pm 10\%$

The conventional and prompt atmospheric neutrino fluxes are parametrized as:

$$\Phi_c = (1 + \alpha_c) \left(\frac{E}{E_{median}} \right)^{\Delta\gamma} \Phi_{Honda} \tag{11.1}$$

$$\Phi_p = (1 + \alpha_p) \left(\frac{E}{E_{median}} \right)^{\Delta\gamma} \Phi_{Sarcevic} \tag{11.2}$$

$1 + \alpha_c$ and $1 + \alpha_p$ describe the deviation in the absolute normalization of the conventional and prompt atmospheric neutrino fluxes respectively from the reference atmospheric neutrino models. The models from Honda *et al* and Sarcevic *et al* are used as the reference models for the conventional and prompt atmospheric neutrino fluxes. The uncertainty in the primary cosmic ray slope, $\Delta\gamma$, changes the shape of the predicted atmospheric neutrino flux. This is modeled by introducing an energy dependent weight $(E/E_{median})^{\Delta\gamma}$ where E_{median} is the median neutrino energy at final cut level. The median energy is 1.17 TeV for the conventional atmospheric neutrino prediction and 7.24 TeV for the prompt atmospheric neutrino prediction.

The detector efficiency, ϵ, affects the overall event rate in the IceCube detector. The magnitude of this systematic error combines in quadrature the systematic uncertainties in the absolute DOM sensitivity, the neutrino interaction cross section, and the muon energy loss cross sections giving an allowed range of $\pm 8.3\%$.

The scattering and absorption coefficients $b(405)$ and $a(405)$ are implemented as discrete nuisance parameters in the analysis. This is facilitated by generating a set of neutrino MC simulations for a range of allowed values for the scattering and absorption coefficients, which are summarized in Table 11.2.

Table 11.2: Simulated range of scattering and absorption coefficients

$b_e(405)$	$a(405)$
baseline	baseline
+10%	+10%
−10%	−10%
+10%	−10%
−10%	+10%

The primary goal of the analysis is the search for evidence of diffuse astrophysical muon neutrinos. The main physics parameter in this search is the normalization of a hypothetical E^{-2} spectrum:

$$\Phi_a = N_a E^{-2} \tag{11.3}$$

Where N_a has units of $\mathrm{GeV}^{-1}\mathrm{cm}^{-2}\mathrm{s}^{-1}\mathrm{sr}^{-1}$. Other astrophysical models are also considered in the analysis and are tested in the next chapter. The primary analysis also includes the absolute normalization of the prompt atmospheric neutrino flux as a physics parameter. The likelihood function therefore has two physics parameters and

five nuisance parameters:

$$L(\theta_r, \theta_s) = L\left(N_a, 1 + \alpha_p, 1 + \alpha_c, \Delta\gamma, \epsilon, b_e(405), a(405)\right) \tag{11.4}$$

The profile likelihood construction can also be used to determine the conventional atmospheric neutrino flux. This analysis promotes the deviation in the conventional atmospheric flux and the uncertainty in the primary cosmic ray spectral slope to physics parameters, giving a likelihood with two main physics parameters and four nuisance parameters:

$$L(\theta_r, \theta_s) = L\left(1 + \alpha_c, \Delta\gamma, 1 + \alpha_p, \epsilon, b_e(405), a(405)\right) \tag{11.5}$$

The likelihood function depends on the total expected number events defined in eq. 10.2. The total expected number of events from atmospheric and astrophysical neutrinos is a convolution of the neutrino fluxes with the effective area defined in eq. 9.1:

$$\mu_c = \int dE_\nu \, d\Omega \, dt \, A_{eff}(E, \theta, \phi) \, (1 + \alpha_c) \left(\frac{E}{1.17 \ TeV}\right)^{\Delta\gamma} \Phi_{Honda}(E_\nu, \theta, \phi)$$

$$\mu_p = \int dE_\nu \, d\Omega \, dt \, A_{eff}(E, \theta, \phi) \, (1 + \alpha_p) \left(\frac{E}{7.24 \ TeV}\right)^{\Delta\gamma} \Phi_{Sarcevic}(E_\nu, \theta, \phi) \tag{11.6}$$

$$\mu_a = \int dE_\nu \, d\Omega \, dt \, A_{eff}(E, \theta, \phi) \, N_a E^{-2}$$

These components are scaled by the uncertainty in the detector efficiency, ϵ, which linearly changes the event expectation. During the minimization, the physics

and nuisance parameters are allowed to vary, with each nuisance parameter constrained within the range defined in Table 11.1. Nuisance parameters that have gaussian constraints to restrict their range requires a modification to eq. 10.3:

$$-2\log L(\{n_i\}|\{\theta_r\}) = 2\sum_{i=1}^{N}(\mu_i - n_i\log\mu_i + \log n_i!) + \sum_{j=1}^{N_s}\frac{(\theta_{s,j} - \theta_{s0,j})^2}{\sigma_{s,j}^2} \qquad (11.7)$$

where N_s denotes the number of nuisance parameters. The scattering and absorption coefficients are discrete nuisance parameters in the analysis, so they are allowed to vary by incorporating the generated neutrino MC simulation sets defined in Table 11.2. The minimization terminates when the point is found in the likelihood space that minimizes eq. 11.7, thereby providing the best fit values of all the physics and nuisance parameters to the data. Confidence regions for the physics parameters of interest are defined using the profile construction method in ch. 10.2.

The sensitivity of the profile construction analysis to a diffuse flux of astrophysical muon neutrinos is calculated by considering the median 90% upper limit obtained over an ensemble of simulated experiments with no true signal. The sensitivity of the analysis to a diffuse astrophysical ν_μ flux is 1.22×10^{-8} $\frac{\text{GeV}}{\text{cm}^2\text{ s sr}}$. The discovery potential of the analysis is defined by finding the strength a hypothetical astrophysical ν_μ flux required to obtain a 5σ discovery in 90% of simulated experiments in the ensemble. The E^{-2} astrophysical normalization required for such a discovery is 6.1×10^{-8} $\frac{\text{GeV}}{\text{cm}^2\text{ s sr}}$. Further information about the calculation of the sensitivity and discovery potential of this analysis is given in Appendix D.

Chapter 12

Results

12.1 Final dE_{reco}/dX Distribution and Fit Results

The final data sample was analyzed with the profile likelihood construction method described in ch. 10. We find no evidence for an astrophysical neutrino flux or a prompt component of the atmospheric neutrino flux. The fitted dE_{reco}/dX distribution is shown in fig. 12.1 and the best fit values of the analysis parameters to the data are summarized in Table 12.1.

Table 12.1: Fit Results

Parameter	Best Fit Value	Error Range
$1 + \alpha_c$	0.96	± 0.096
$1 + \alpha_p$	0	0.73 (90% U.L.)
$\Delta\gamma$	-0.026	± 0.012
ϵ	$+2\%$	± 0.09
$b_e(405), a(405)$	Baseline Ice Model	$\pm 10\%$
N_a	0	$8.9 \times 10^{-9} \; \frac{\text{GeV}}{\text{cm}^2 \text{ s sr}}$ (90% U.L.)
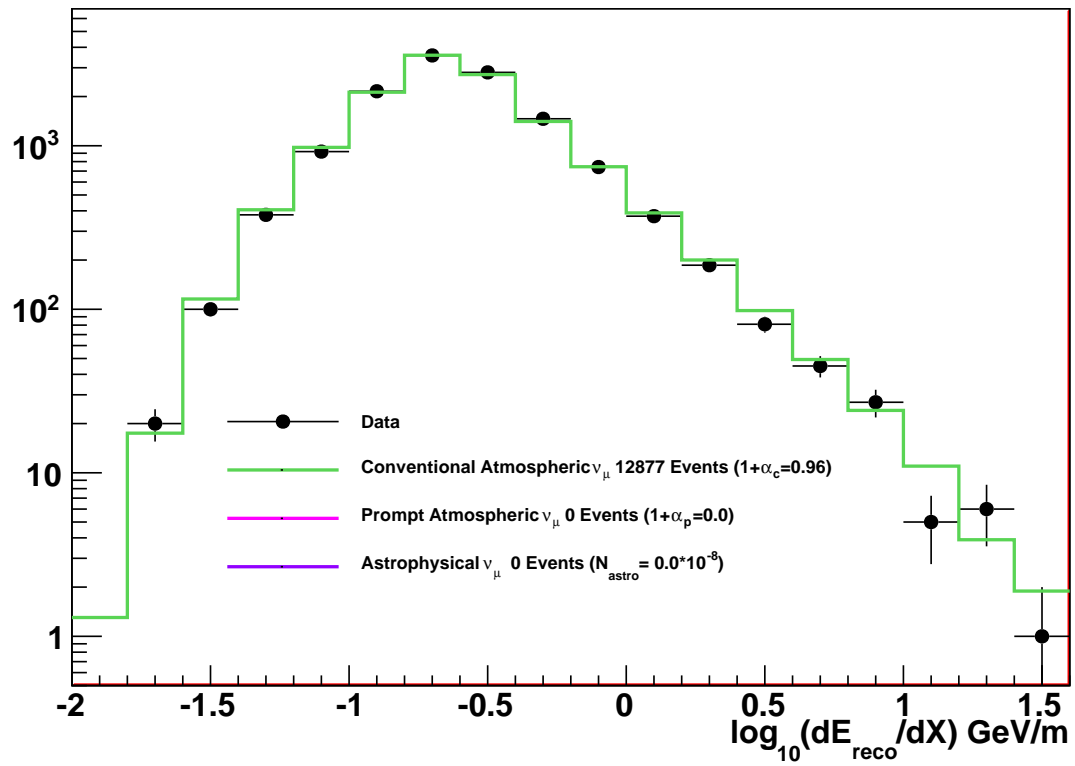
Figure 12.1: The fitted muon energy loss distribution of the final event sample is shown. The best fit to the data consists only of conventional atmospheric ν_μ, and no evidence is found for a prompt atmospheric ν_μ flux or an astrophysical E^{-2} ν_μ flux.

12.2   Upper Limits on Astrophysical Neutrino Fluxes

12.2.1 $\Phi_{\nu_\mu} = N_a E^{-2}$

There is no evidence in the IceCube 40-string data set for astrophysical neutrinos with a E^{-2} spectrum, nor is there any evidence for prompt atmospheric neutrinos predicted by the standard theoretical calculation from Sarcevic *et al* [33]. The allowed regions for the astrophysical normalization N_a corresponding to an E^{-2} ν_μ flux and prompt atmospheric neutrinos are shown in fig. 12.2. The most conservative upper limit for N_a at 90% confidence level is obtained from fig. 12.2 by finding the point on the 90% *C.L.* boundary along the null hypothesis of no prompt atmospheric neutrinos. The 90% upper limit on a hypothetical astrophysical $\Phi_{\nu_\mu} = N_a E^{-2}$ flux at Earth with systematic uncertainties included is $N_a^{90\%} = 8.9 \times 10^{-9}$ GeVcm^{-2}s^{-1}sr^{-1}. The result is valid from the energy range 34.7 TeV to 6.9 PeV. We note that the observed upper limit is quite below the expected analysis sensitivity of the analysis of 1.22×10^{-8} GeVcm^{-2}s^{-1}sr^{-1}. This 90% upper limit on an astrophysical ν_μ flux is compared to other ν_μ limits and flux models in fig. 12.3.

The energy range is determined from MC simulation studies of the analysis sensitivity, which was calculated to be 1.22×10^{-8} GeVcm^{-2}s^{-1}sr^{-1}. A high energy cutoff on the neutrino energy was introduced until the sensitivity of the analysis decreased by five percent, providing the high energy end of the energy range. The same procedure was done by introducing a lower energy cut on the neutrino energy until the sensitivity of the analysis also changed by five percent. This provides the lower end of the energy range.

Since astrophysical neutrinos are predicted to have a flavor ratio at Earth of
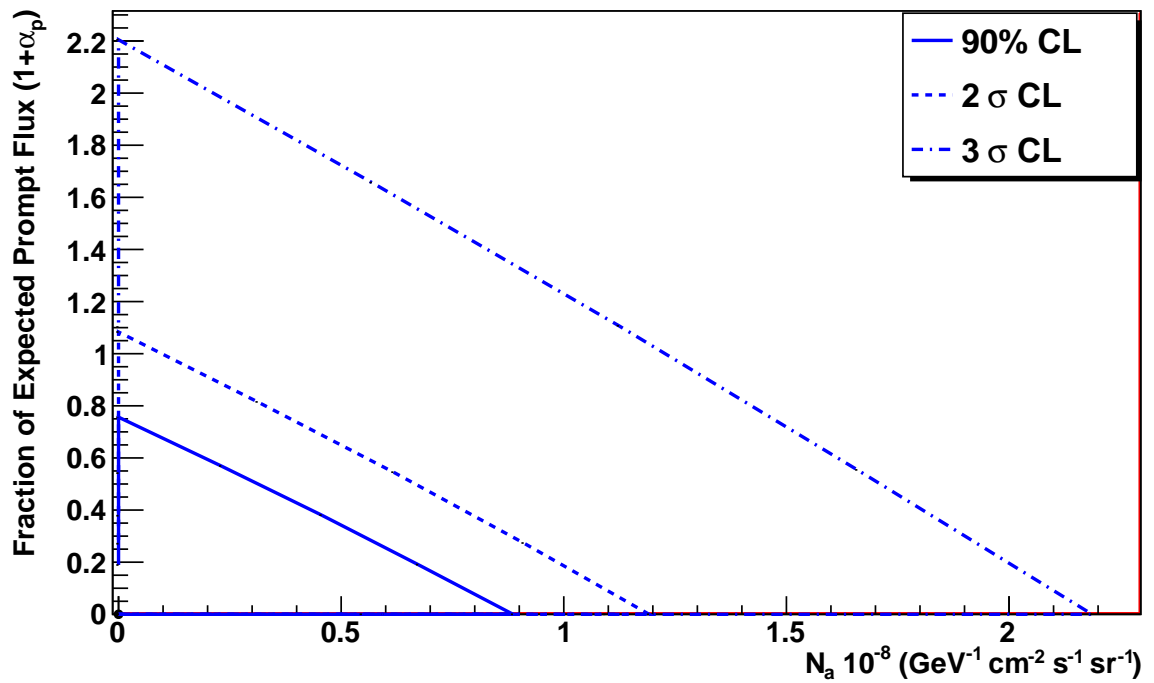
Figure 12.2: Allowed regions for astrophysical muon neutrinos with an E^{-2} spectrum and prompt atmospheric neutrinos at 90%, 2σ, and 3σ confidence level. The lines indicate the boundary of the allowed region at the stated confidence level. The area to the left of the boundary is allowed while the area to the right of the boundary is excluded. The best fit point is shown as the black dot at the origin. Systematic uncertainties are included in the calculation of these exclusion regions.
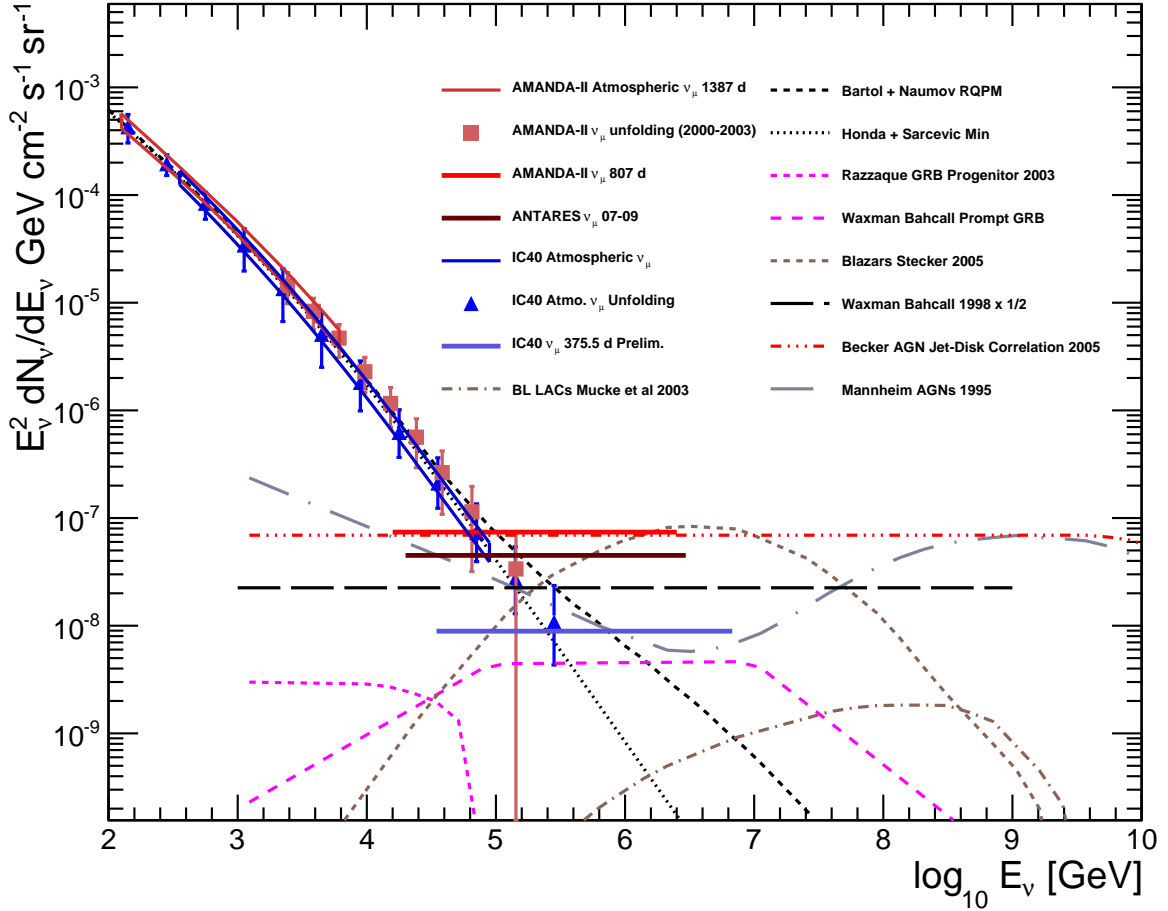
Figure 12.3: Upper limits on an astrophysical ν_μ flux with an E^{-2} spectrum are shown along with theoretical model predictions of diffuse astrophysical muon neutrinos from different sources. Measurements of the atmospheric neutrino spectrum are also shown along with theoretical atmospheric neutrino flux models. The astrophysical E^{-2} ν_μ upper limits shown are the 3 year AMANDA-II limit [79], the ANTARES 3 year limit [80], and the current work. The atmospheric ν_μ measurements shown are the AMANDA-II Atmospheric ν_μ forward folding measurement [81], the AMANDA-II unfolding measurement [82], the IceCube 40-string unfolding measurement [83] and the current work.
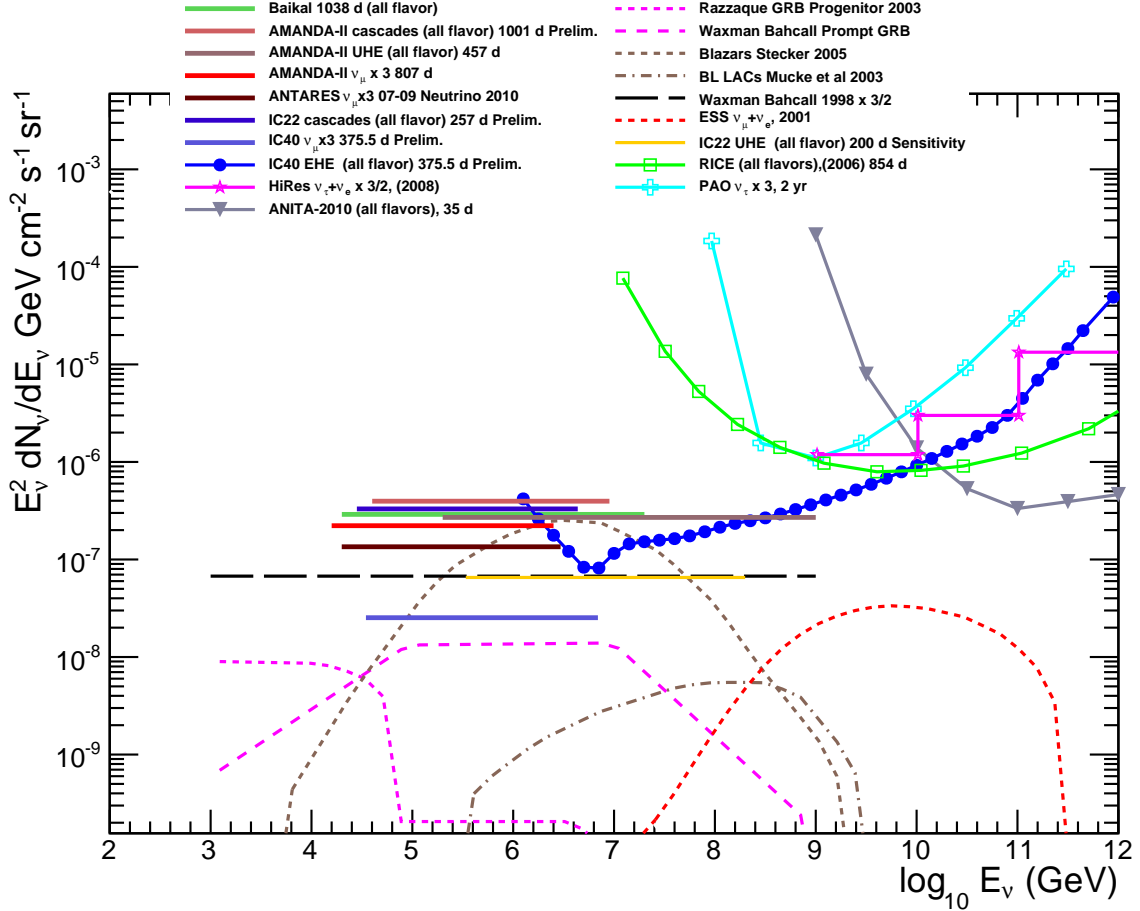
Figure 12.4: Upper limits on an all-flavor astrophysical neutrino flux are shown along with various predictions for a diffuse astrophysical neutrinos from different sources. The integral upper limits on an astrophysical E^{-2} flux shown are the 5 year AMANDA-II cascade search, [84], the AMANDA-II upper limit on ultra high energy astrophysical neutrinos, [85], the 3-year AMANDA-II ν_μ limit multiplied by 3 [79], the ANTARES 3-year limit on ν_μ multiplied by 3 [80], the IceCube 22-string cascade search [86], the IceCube 22-string ultra high energy sensitivity [87], and the current work. The differential 90% upper limits on an astrophysical neutrino flux have all been normalized to one entry per energy decade. The differential upper limits shown are from the Radio Ice Cherenkov Experiment (RICE) [88], the Pierre Auger Observatory's upper limit on ν_τ multiplied by 3[89], the HiRes experiment [90], the Antarctic Impulsive Transient Antenna (ANITA) [91], and the IceCube 40-string extremely high energy result [92].

$\nu_e : \nu_\mu : \nu_\tau = 1 : 1 : 1$, we take into account the contribution of astrophysical ν_τ to the muon flux at the IceCube detector discussed in ch. 11 when deriving an all-flavor 90% upper limit on astrophysical neutrinos. This results in a 90% upper limit on all flavors of astrophysical neutrinos of 2.53×10^{-8} GeVcm^{-2}s^{-1}sr^{-1}, which is 5.5% lower than multiplying the single flavor limit by a factor of 3. The all-flavor 90% upper limit on astrophysical neutrinos from this analysis is compared to other all-flavor limits and flux models in fig. 12.4.

12.2.2 Other Models of Astrophysical Neutrino Fluxes

Astrophysical neutrino models that do not predict an E^{-2} spectrum were tested in the analysis. The models are shown in fig. 12.3 and were discussed in ch. 2. Of the models considered, this analysis is sensitive to the blazar model derived by Stecker [93], the AGN neutrino model derived by Mannheim [20], and the radio galaxy neutrino model from Becker, Biermann, and Rhode [94]. The simulated energy distributions of these models for the 40-string configuration of IceCube are shown in figs. 12.5 - 12.7. These models are all rejected at the 5σ confidence level. The analysis also rules out the Waxmann-Bahcall upper bound [22] at a 3σ confidence level. The upper limits on astrophysical ν_μ for the different models are summarized in table 12.2. The upper limits for the models are expressed in terms of the model rejection factor [95], which in the context of this analysis is the fraction of the model rejected at the stated confidence level. As in the E^{-2} case discussed above, the contribution of ν_τ to the muon flux changes the all flavor astrophysical neutrino limits. The all-flavor upper limits on astrophysical neutrinos are summarized in table 12.3.
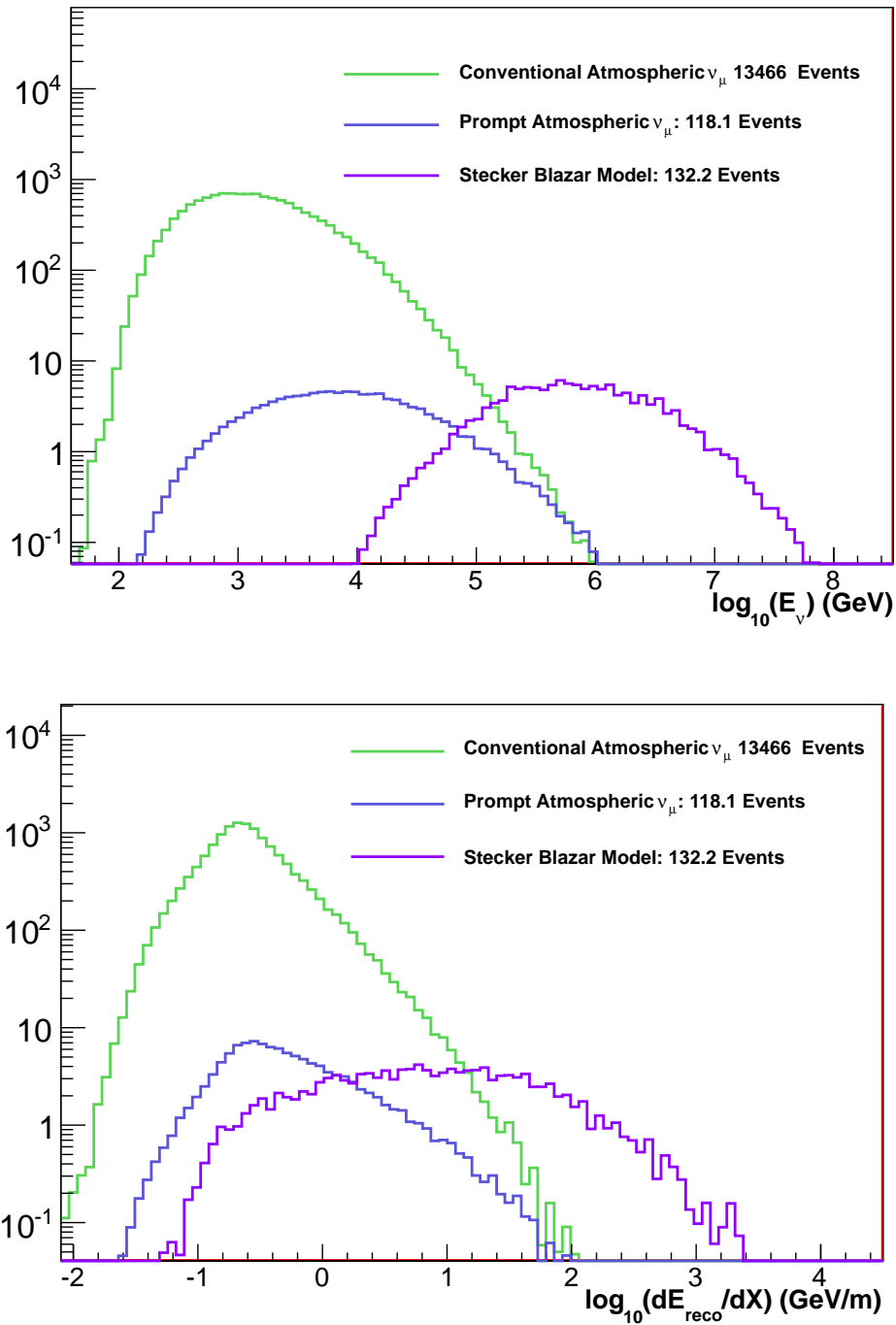
Figure 12.5: Simulated contribution of astrophysical ν_μ from the blazar model derived by Stecker to the energy distribution of the final muon event sample. The top plot shows the MC neutrino energy, and the bottom plot shows the simulated dE_{reco}/dX distribution of the muon.
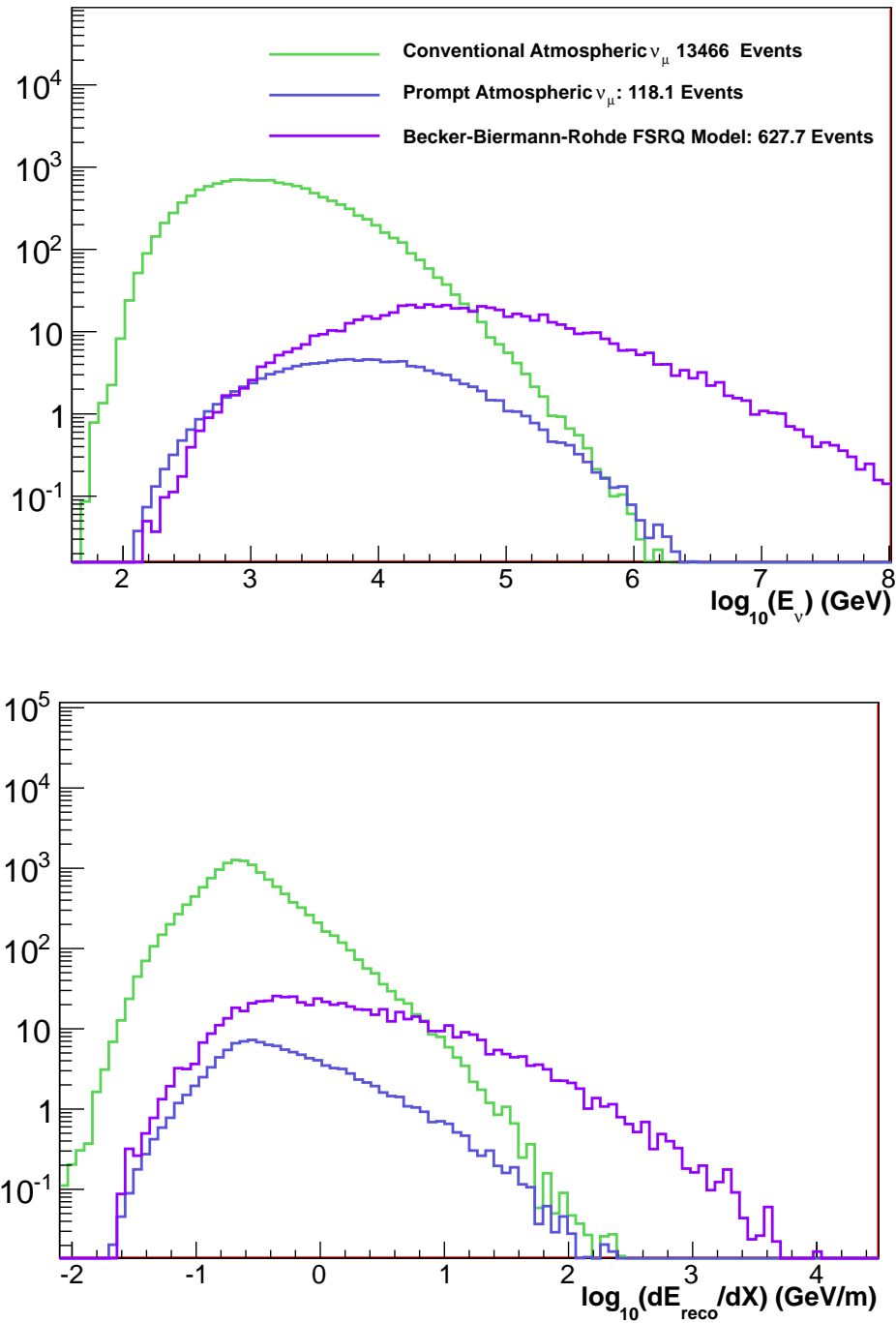
Figure 12.6: Simulated contribution of astrophysical ν_μ from the radio galaxy model derived by Becker, Biermann, and Rohde to the energy distribution of the final muon event sample. The top plot shows the MC neutrino energy, and the bottom plot shows the simulated dE_{reco}/dX distribution of the muon.
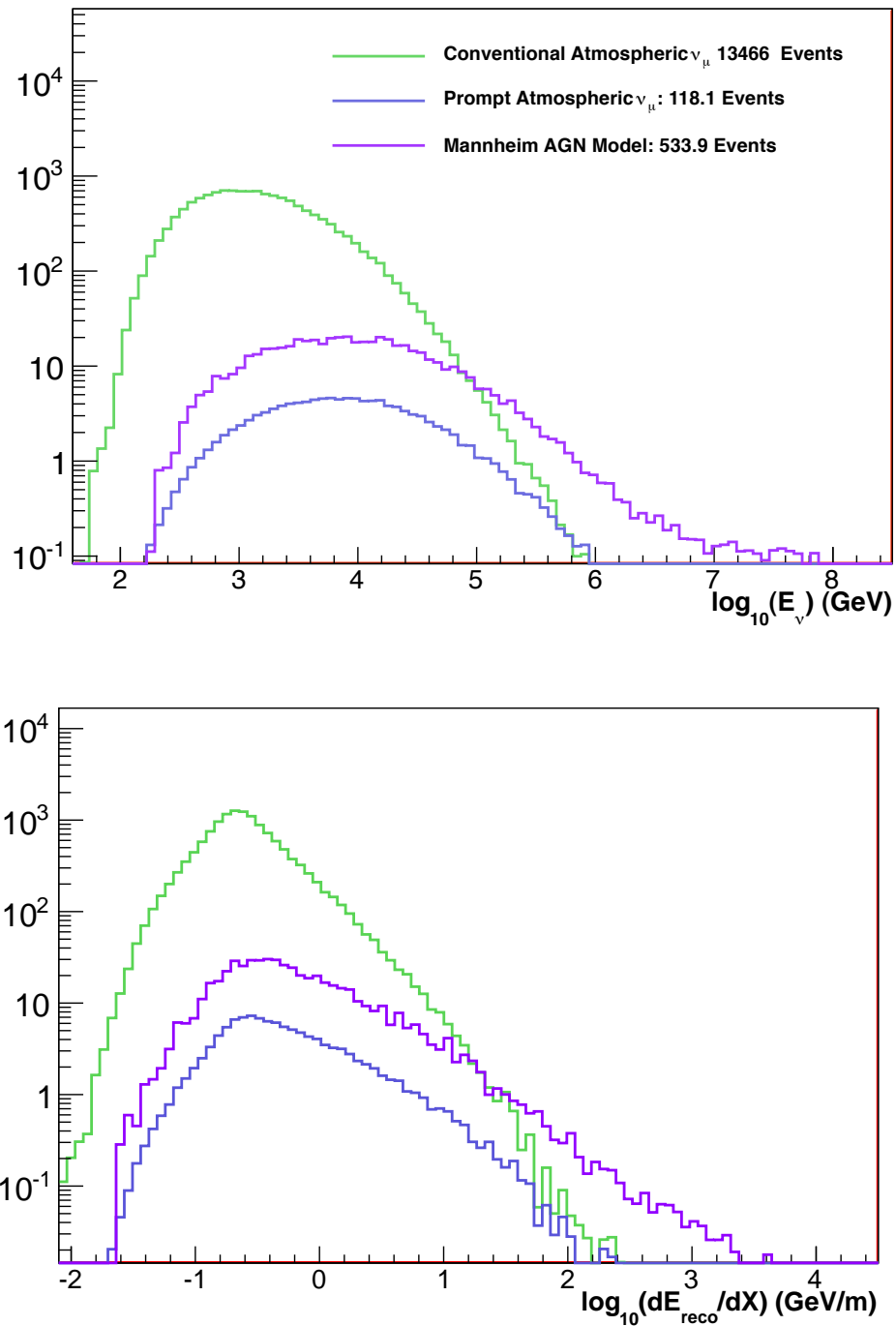
Figure 12.7: Simulated contribution of astrophysical ν_μ from the AGN model derived by Mannheim to the energy distribution of the final muon event sample. The top plot shows the MC neutrino energy, and the bottom plot shows the simulated dE_{reco}/dX distribution of the muon.

Table 12.2: Upper Limits for Astrophysical ν_μ for different Astrophysical Models

Model	90%	95%	3σ	5σ
$E^{-2} \left(\frac{GeV}{cm^2\ s\ sr} \right)$	0.89×10^{-8}	1.2×10^{-8}	2.2×10^{-8}	4.0×10^{-8}
W-B Upper Bound	0.4	0.53	0.97	1.78
Stecker Blazar Model	0.1	0.14	0.32	0.42
BBR FSRQ neutrino model	0.02	0.04	0.09	0.12
Mannheim AGN model	0.02	0.03	0.14	0.2

Table 12.3: All-flavor $(\nu_\mu + \nu_e + \nu_\tau)$ Upper Limits for Astrophysical Neutrinos for different Astrophysical Models

Model	90%	95%	3σ	5σ
$E^{-2} \left(\frac{GeV}{cm^2\ s\ sr} \right)$	2.53×10^{-8}	3.41×10^{-8}	4.25×10^{-8}	11.36×10^{-8}
W-B Upper Bound	0.38	0.50	0.92	1.69
Stecker Blazar Model	0.09	0.13	0.29	0.38
BBR FSRQ neutrino model	0.019	0.038	0.086	0.11
Mannheim AGN model	0.019	0.029	0.135	0.18

12.3 Measurement of the Atmospheric Neutrino Flux

There is no evidence for astrophysical neutrinos in our final event sample, and therefore the final neutrino distribution is interpreted as a flux of atmospheric muon neutrinos in the context of the standard model. The profile construction method is used to perform a forward-folding fit of the atmospheric neutrino flux as described in ch. 11.7 to determine the normalization and any change in shape from the reference atmospheric neutrino flux model considered. We test the hypothesis with the reference flux from Honda *et al* for the conventional flux and Sarcevic *et al* for the prompt flux:

$$\Phi_c\left(E, \theta, \phi\right) = \left(1 + \alpha_c\right) \left(\frac{E}{E_{median}}\right)^{\Delta\gamma} \Phi_{Honda}\left(E, \theta, \phi\right) \qquad (12.1)$$

$$\Phi_p\left(E, \theta, \phi\right) = \left(1 + \alpha_p\right) \left(\frac{E}{E_{median}}\right)^{\Delta\gamma} \Phi_{Sarcevic}\left(E, \theta, \phi\right) \qquad (12.2)$$

There is no evidence for prompt atmospheric neutrinos in the data. The best fit result of the atmospheric neutrino flux is of the form:

$$\Phi_{bestfit}\left(E, \theta, \phi\right) = \left(0.96\right) \left(\frac{E}{1.17\ TeV}\right)^{-0.027} \Phi_{Honda}\left(E, \theta, \phi\right) \qquad (12.3)$$

The allowed regions of $(1 + \alpha_c)$ and $\Delta\gamma$ are shown in fig. 12.8. These allowed regions can be translated into a range of fluxes that can be compared to the reference flux model and other measurements of the atmospheric neutrino flux. Every point on the 90% boundary in fig. 12.8 corresponds to a different allowed atmospheric neutrino flux. The envelope formed from this set of fluxes provides the 90% error band of the measured atmospheric neutrino flux. The measured atmospheric neutrino flux along with this 90% error envelope are compared to the calculation from Honda *et al* and other measurements of the atmospheric neutrino flux in fig. 12.9. Also shown in fig. 12.9 is the atmospheric neutrino unfolding analysis discussed in [83]. The unfolding analysis makes no prior assumption regarding the shape of the atmospheric neutrino spectrum, where as this work fits the deviation in the normalization and spectral index of the model calculated by Honda *et al.* [31]. The effect of this differing prior assumption of the flux in the two analyses is a different allowed error band in the measurement of the atmospheric neutrino spectrum.

The energy range of the atmospheric neutrino flux measurement is valid from 332.4 GeV to 83.7 TeV. This energy range is derived from the lowest and highest values of the reconstructed muon energy loss in the data. The median neutrino energy
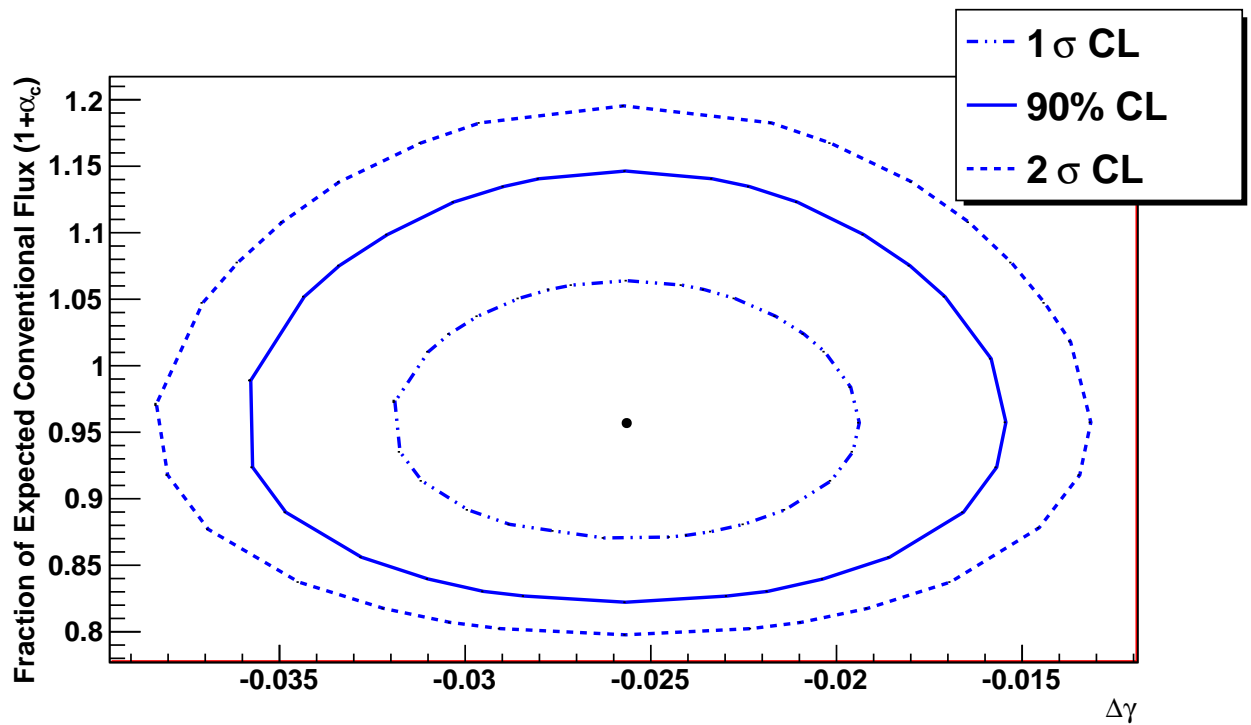
Figure 12.8: 1σ, 90%, and 95% allowed regions for the normalization $(1 + \alpha_c)$ and the change in spectral index $(\Delta\gamma)$ of the conventional atmospheric neutrino flux relative to Honda *et al* [31]. The lines indicate the allowed boundaries at the stated confidence level. The region enclosed by the boundary are allowed and the region outside the boundary is excluded.
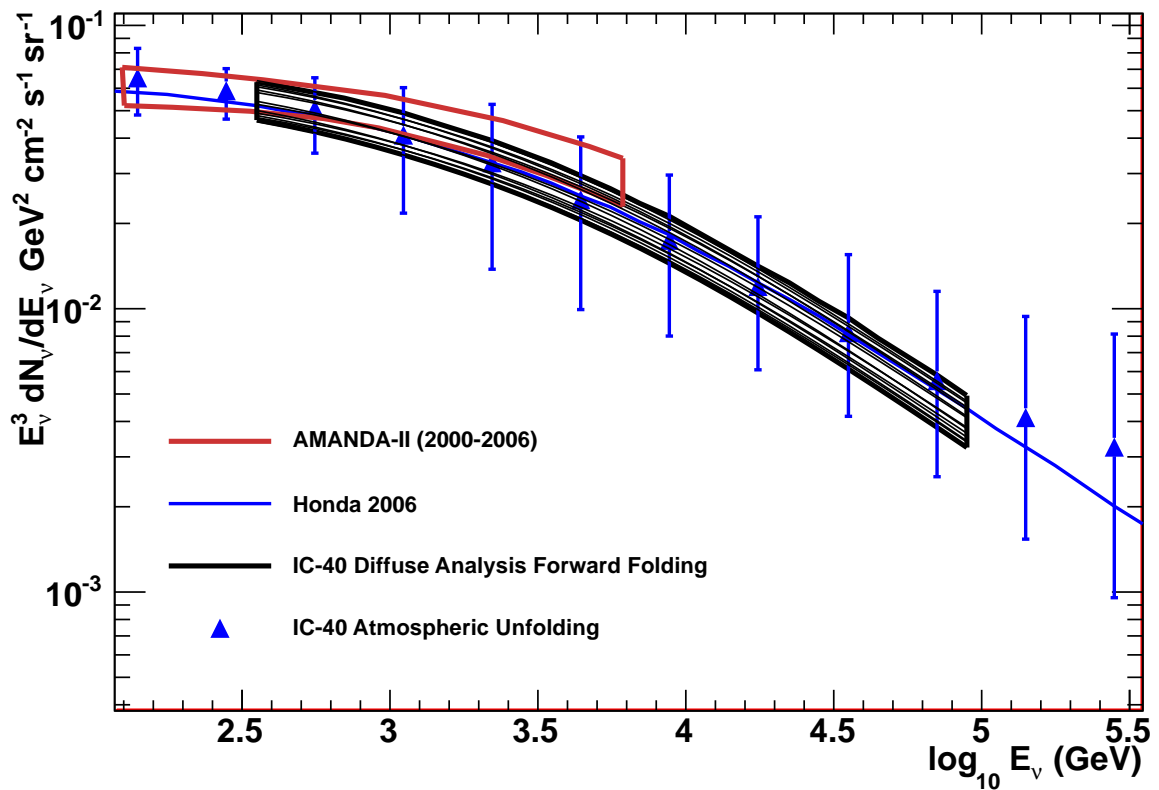
Figure 12.9: Angle-averaged $\nu_\mu + \bar{\nu}_\mu$ measurements of the atmospheric neutrino flux and the model prediction from Honda *et al* [31]. The fluxes are multiplied by E^3 to enhance features. The black set of curves is this work, the blue triangles are from the atmospheric unfolding analysis discussed in [83], and the brown band is the forward folding result discussed in [81].

for the reference atmospheric neutrino flux for the lowest dE_{reco}/dX value in the data

provides the lower end of the energy range, and the median neutrino energy for the

highest dE_{reco}/dX value in the data provides the higher end of the energy range.

12.4   Upper Limits on Prompt Atmospheric Neutrinos

The result of this analysis shows no evidence for a prompt component to the

atmospheric neutrino flux. Hypotheses other than the reference model from Sarcevic

et al are shown in fig. 11.3 and were tested in this analysis. The results of the prompt

model tests are summarized in table 12.4. Like the astrophysical model tests described

above, the upper limits on prompt atmospheric neutrinos are expressed in terms of

the model rejection factor. The standard calculation from Sarcevic *et al* which is used

as the reference flux in this analysis is rejected at 90% confidence level.

Table 12.4: Upper Limits on Prompt Atmospheric Neutrinos for different Models

Model	90%	95%	3σ
Sarcevic (Minimum)	1.25	1.8	3.6
Sarcevic (Standard)	0.73	1.1	2.2
Sarcevic (Maximum)	0.53	0.85	1.89
Naumov RQPM	0.2	0.41	0.87

Chapter 13

Conclusions and Outlook

13.1 Summary of Results

We have set the field's most stringent limit on astrophysical muon neutrinos from unresolved sources. The 90% upper limit on an astrophysical flux with an E^{-2} spectrum is 8.9×10^{-9} GeVcm^{-2}s^{-1}sr^{-1}, valid from the energy range of 34.7 TeV to 6.9 PeV. Several optimistic astrophysical neutrino production models are rejected at a 5σ confidence level. We have also set stringent limits on the prompt component of the atmospheric neutrino flux, constraining the models to the predictions calculated with perturbative quantum chromodynamics and rejecting the standard prediction from Sarcevic *et al.* [33] at a 90% confidence level. Finally, we have measured the atmospheric muon neutrino flux from 332.4 GeV to 83.7 TeV and find a fit result that is slightly lower than the calculation from the Honda *et al.* [31]. The result is consistent with other measurements made of the atmospheric neutrino flux with the IceCube detector and its predecessor, AMANDA.

13.2 Discussion and Outlook

The stringent 90% upper limit on a diffuse astrophysical flux of muon neutrinos reported by this analysis along with the rejection of the models from Stecker, Mannheim, Waxmann-Bachall, and Becker-Biermann-Rhode implies that the partially completed IceCube detector is not yet sensitive enough to discover astrophysical neutrinos from unresolved sources and the actual astrophysical neutrino flux is not close to the upper bound reported by the optimistic models ruled out by this work. The full 86-string array will be completed during the 2010-2011 summer construction season at the South Pole. An astrophysical E^{-2} ν_μ flux at the 90% limit derived by this work will take three years of the full IceCube array for a 5σ discovery.

This time scale for discovery can be made shorter by an improved understanding of the various sources of systematic uncertainty and considering new analysis techniques. It is particularly difficult to disentangle a potential diffuse astrophysical neutrino signal from a possible prompt component to the atmospheric neutrino flux. With a proper measurement of the prompt component of the atmospheric neutrino flux, the time scale for discovery becomes more tractable. Analyses dedicated to the study of leptons from the decay of charmed mesons would also yield a better understanding of the physics of air showers and atmospheric neutrinos. Other strategies other than using atmospheric ν_μ to search for the prompt component involve a thorough investigation of the down-going muon flux and a measurement of the atmospheric neutrino spectrum from ν_e. The former analysis takes advantage of the large statistics of the down-going atmospheric muon flux to analyze differences in the zenith angle and energy observable dependence between muons from the decay of charmed

mesons and the decay of pions and kaons. Pioneering analysis work was done with the AMANDA detector [96], and IceCube provides improved statistics of high energy atmospheric muons. The measurement of the atmospheric ν_e flux has an advantage that the transition energy from conventional ν_e to prompt ν_e occurs at an order of magnitude lower in energy than in ν_μ. (See fig. 13.1)
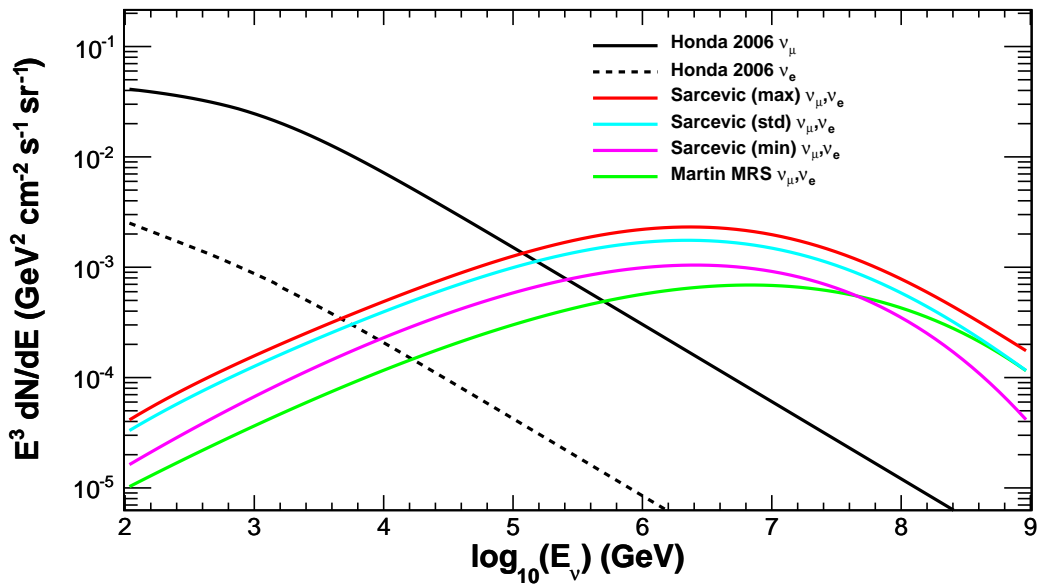
Figure 13.1: Predicted prompt atmospheric neutrino fluxes averaged over zenith angle and multiplied by E^3 to enhance features. The Honda 2006 model expectations for ν_μ and ν_e are shown for comparison. The calculations of the prompt component of the atmospheric neutrino flux predict the same contribution from ν_μ and ν_e, where as the conventional atmospheric flux from ν_e is an order of magnitude below the flux from ν_μ.

The event selection in this analysis used the Earth as a filter to remove the large down-going atmospheric muon background. An improved simulation of atmospheric muons would allow a diffuse astrophysical ν_μ search to incorporate the down-going region in the analysis. In particular, the horizontal region is particularly sensitive to

the primary cosmic ray composition. We note that our final zenith distribution in Fig. 9.5 shows an eight percent deficit of atmospheric neutrino Monte Carlo below data at the horizontal region between 90 and 97 degrees in zenith angle. Although this discrepancy does not affect our limit on astrophysical ν_μ or our reconstructed atmospheric neutrino spectrum, understanding the origin of the discrepancy is important for future work. In order to explain the deficit, a possible physics scenario has been suggested [83] which involves high Δ_{M^2} oscillations of $\bar{\nu}_\mu$ which would lead to a deficit of up-going muon anti-neutrinos.

Although this analysis focuses on ν_μ, IceCube is sensitive to all flavors of neutrinos. As the detector grows, reconstruction methods mature, and the understanding of the various sources of systematic uncertainty improve, it would be possible to combine event topologies from different neutrino flavors in a multi-flavor analysis. A simultaneous search for neutrinos of all flavors from unresolved astrophysical sources would be significantly more sensitive than an analysis focusing exclusively on a single neutrino flavor.

As the IceCube neutrino observatory explores new territory in neutrino astronomy with a completed detector and improved analysis techniques, the experiment has a high potential for discovery. IceCube is in position to usher in a new era of particle astrophysics and contribute to multi-messenger astronomy with a new window into the universe.

Bibliography

[1] E. Clements, "New tools forge new frontiers," *Symmetry Magazine* **August** (2008) .

[2] Y. Fukuda *et al.*, "Measurements of the solar neutrino flux from super-kamiokande's first 300 days," *Phys. Rev. Lett* **81** (1998) 1158.

[3] J. Yang *et al.*, "Constraints on cosmology and neutrino physics from big bang nucleosynthesis," *Astrophys. J* **227** (1979) 697.

[4] K. Hirata *et al.*, "Observation of a neutrino burst from the supernova sn 1987a," *Phys. Rev. Lett* **58** (1987) 1490.

[5] P. Krastev and A. Smirnov, "Global analysis with sno: Torward the solution of the solar neutrino probem," *Phys. Rev. D* **65** (2002) 073022.

[6] W. Pauli in *Rapports du Septieme Conseil de Physique Solvay*. Gauthier-Villars, Paris, 1934.

[7] F. Reines and C. Cowan, "Detection of the free neutrino," *Phys. Rev.* **92** (1953) 830.

[8] V. Hess, "The cosmic-ray spectrum: from the knee to the ankle," *Phys Z.* **13** (1912) 1804.

[9] T. K. Gaisser, *Particle Physics and Cosmic Rays.* Cambridge University Press, U.K., 1991.

[10] T. Gaisser, "The cosmic-ray spectrum: from the knee to the ankle," *J. Phys. Conf Ser.* **47** (2006) 15.

[11] J. Hoerandel, "Models of the knee in the energy spectrum of cosmic rays.," *Astropart. Phys..* **21** (2004) 241.

[12] P. Sokolsky, "Observation of the gzk cutoff by the hires experiment and the pierre auger observatory," *Mod. Phys. Lett.* **A23** (2008) 1290.

[13] J. Learned and K. Mannheim, "High energy neutrino astrophysics," *Ann. Rev. Nucl. Part. Science* **50** (2000) 679.

[14] M. Longair, *High Energy Astrophysics Vol. 2.* Cambridge University Press, 1981.

[15] J. P. Raachen in *American Institute of Physics Conference Series*, p. 41. 2000.

[16] H. Athar *et al.*, "Effects of neutrino mixing on high-energy cosmic neutrino flux," *Phys. Rev. D* **62** (2000) 103007.

[17] F. Stecker, "Note on high-energy neutrinos from active galactic nuclei cores," *Phys. Rev. D* **72** (2005) 107301.

[18] A. Mucke, "Bl lac objects in the synchrotron proton blazar model," *Astropart. Phys.* **18** (2003) 593.

[19] J. Becker *et al.*, "The diffuse neutrino flux from fr-ii radio galaxies and blazars: A source property based estimate," *Astropart. Phys.* **23** (2005) 355.

[20] K. Mannheim *Astropart. Phys* **3** (1995) 295.

[21] S. Razzaque and P. Meszaros, "Neutrino tomography of gamma ray bursts and massive stellar collapses," *Phys. Rev. D* **68** (2003) 083001.

[22] E. Waxman and J. Bahcall, "High energy neutrinos from astrophysical sources: An upper bound," *Phys. Rev. D.* **59** (1998) 023002.

[23] R. Engel *et al.*, "Neutrinos from propagation of ultrahigh energy protons," *Phys. Rev. D* **64** (2001) 093010.

[24] R. Alosio, "Ultra high energy neutrino signatures in top-down scenarios," in *Workshop on Exotic Physics with Neutrino Telescopes*. 2006.

[25] V. Barger *et al.*, "Indirect search for neutralino dark matter with high-energy neutrinos," *Phys. Rev. D* **65** (2002) 0705022.

[26] B. Louis *et al.*, "The evidence for oscillations," *Los Alamos Science* **25** (1997) 16.

[27] P. D. Group, *Particle Physics Booklet.* AIP, 2008.

[28] G. Thunman *et al. Astroparticle Phys.* **5** (1996) 309.

[29] T. K. Gaisser and M. Honda *Annu. Rev. Nucl. Part. Sci.* **52** (2002) 153.

[30] G. Barr *et al.*, "Three-dimensional calculation of atmospheric neutrinos," *Phys. Rev. D* **70** (2004) 023006.

[31] M. Honda *et al.*, "Calculation of the atmospheric neutrino flux using the interaction model calibrated with atmospheric muon data," *Phys. Rev. D* **75** (2007) 043006.

[32] C. Costa, "The prompt lepton cookbook," *Astropart. Phys.* **16** (2001) 193.

[33] I. Sarcevic *et al.*, "Prompt neutrino fluxes from atmospheric charm," *Phys. Rev. D* **78** (2008) 043005.

[34] G. F. A. Naumov and F. Villante *Phys. Lett. B* **510** (1989) 173.

[35] A. M. M. Ryskin and A. Stasto *Acta Phys. Polon. B* **34** (2003) 3273.

[36] A. Gazizov and M. Kowalski, "Anis: High energy neutrino generator for neutrino telescopes," *Comp. Phys. Comm* **172** (2005) 203. astro-ph/0406439.

[37] H. Lai *et al.*, "Global qcd analysis of parton structure of the nucleon: Cteq-5 parton distributions," *Eur. Phys. J* **C12** (2000) 375. hep-ph/9903282.

[38] A. Achterberg *et al.*, "First year performance of the icecube neutrino telescope," *Astropart. Physics* **26** (2006) 155.

[39] D. Chirkin and W. Rhode, "Propagating leptons through matter with muon monte carlo (mmc)," *Preprint* (2004) . hep-ph/0407075v2.

[40] P. Miocinovic, *Muon Energy Reconstruction in the Antarctic Muon and Neutrino Detector Array (AMANDA)*. PhD thesis, University of California at Berkeley, 2001.

[41] C. H. Wiebusch, *The Detection of Faint Light in Deep Underwater Neutrino Telescopes*. PhD thesis, Physikalische Institute, RWTH Aachen, 1995.

[42] R. Wischnewski, "The amanda-ii neutrino-telescope," in *Proceedings from TAUP2001, LNGS/Italy*. 2001. arXiv:astro-ph/0204268v1.

[43] C. Wiebusch, "Physics capabilities of the deepcore detector," in *Proceedings of the 31st International Cosmic Ray Conference, Lodz, Poland*. 2009. arXiv:0907.2263v1.

[44] T. Stanev, "Status, performance, and first results of the icetop array," *Nucl. Phys. Proc. Suppl* **196** (2008) 159. arXiv:0903.0576v1.

[45] R. Abbasi *et al.*, "The icecube data acquisition system: Signal capture, digitization, and timestamping.," *Nucl. Inst. Meth. A* **601** (2009) 294.

[46]

[47] M. Ackerman *et al.*, "Optical properties of deep glacial ice at the south pole," *J. Geophys. Res.* **D13203** (2006) 111.

[48] H. Yepes-Ramirez *et al.*, "Water absorption length measurement with the antares optical beacon system," *Nucl. Inst. Meth. A* (2010) . Article in Press, Corrected Proof.

[49] S. L. Miller, "Clathrate hydrates of air in antarctic ice," *Science* **165** (1969) 489.

[50] D. Chirkin, "Study of south pole ice transparency with icecube flashers." Icecube internal report, 2009.

[51] A. Olivas and others., "Icecube simulation documentation." http://wiki.icecube.wisc.edu/index.php/Simulation_Documentation_Wiki.

[52] D. Heck *et al.*, "Corsika: A monte carlo code to simulate extensive air showers," tech. rep., FZKA, 1998.

[53] Dziewonski and Anderson, "Preliminary reference earth model," *Phys. Earth Planet. Int.* **25** (1981) 297–356.

[54] J. Lundberg *et al.*, "Light tracking through ice and water - scattering and absorption in heterogenous media with photonics," *Nuclear Instrumentation and Methods* **A581** (2007) 619.

[55] NVIDIA, *OpenCL Programming Guide for the CUDA Architecture*, 2010. Tech. Manual.

[56] J. Ahrens *et al.*, "Muon track reconstruction and data selection techniques in amanda," *Nuclear Instrumentation and Methods* **A524** (2004) 169.

[57] D. Chirkin, "Feature extraction of icecube waveforms." Icecube internal report, 2007.

[58] J. Ahrens *et al.*, "Search for neutrino-induced cascades with the amanda detector," *Physical Review D* **67** (2003) 012003.

[59] P. Desiati, "Response of amanda-ii to cosmic ray muons," in *Proceedings of the 28th International Cosmic Ray Conference, Tsukuba, Japan*, p. 1373. 2003.

[60] J. V. Santen, "Markov-chain monte-carlo reconstruction for cascade-like events in icecube," Master's thesis, Humboldt University, 2010.

[61] M. Kowalksi, *Search for Neutrino Induced Cascades with the AMANDA-II detector*. PhD thesis, Universitat Bonn, 2004.

[62] T. Neunhoffer, "Estimating the angular resolution of tracks in neutrino telescopes based on a likelihood analysis," *Astroparticle Physics* **25** (2006) 220–225. astro-ph/0403367v1.

[63] J. Kelley, *Searching for Quantum Gravity with High-Energy Atmospheric Neutrinos and AMANDA-II*. PhD thesis, University of Wisconsin - Madison, 2008.

[64] G. Felman and R. Cousins, "Unified approach to the classical statistical analysis of small signals," *Phys. Rev. D.* **57** (1998) 3873–3889. arXiv:physics/9711021v2.

[65] M. Sanchez *et al.*, "Measurement of the l/e distributions of atmospheric neutrinos in soudan 2 and their interpretation as neutrino oscillations," *Phys. Rev. D.* **68** (2003) 113004. hep-ex/0307069.

[66] R. J. Barlow, *A Guide to the Use of Statistical Methods in the Physical Sciences*. Wiley, 1989.

[67] K. Cranmer, "Frequentist hypothesis testing with background uncertainty," in *Proceedings from PHYSTAT 2003*. 2003. arXiv:physics/0310108.

[68] R. Cousins and V. Highland, "Incorporating systematic uncertainties into an upper limit," *Nuclear Instrumentation and Methods* **320** (1992) 331.

[69] A. S. K. Ord and S. Arnold, *Kendall's Advanced Theory of Statistics*, vol. 2A. Arnold, 6th ed., 1999.

[70] F. James and M. Roos, "Minuit, a system for function minimization and. analysis of the parameter errors and correlations," *Comp. Phys. Comm.* **10** (1975) 343.

[71] G. J. Feldman, "Multiple measurements and parameters in the unified approach," in *Workshop on Confidence Intervals, Fermilab.* 2000. http://www.hepl.harvard.edu/ feldman/Journeys.pdf.

[72] T. Gaisser, "Atmospheric neutrino fluxes," in *XXth International Conference on Neutrino Physics and Astrophysics. Munich, Germany.* 2002. hep-ph/0209195v1.

[73] T. Gaisser *et al.* in *Proceedings of the 27th International Cosmic Ray Conference, Hamburg Germany.* 2001.

[74] R. Abbasi *et al.*, "Calibration and characterization of the icecube photomultiplier tube," *Nuclear Instrumentation and Methods* **618** (2010) 139.

[75] A. Karle and T. Makuluni, "Optical transmission and sensitivity data of icecube digital optical modules." Icecube internal report, 2007.

[76] A. Achterberg *et al.*, "Five years of searches for point sources of astrophysical neutrinos with the amanda-ii neutrino telescope," *Phys. Rev. D* **75** (2007) 102001.

[77] J. Pumplin *et al.*, "New generation of parton distributions with uncertainties from global qcd analysis," *Journal Of High Energy Physics* **07** (2002) .

[78] W. Lowry, *Fundamentals of Geophysics.* Cambridge University Press, 1997.

[79] A. Achterberg *et al.*, "Multiyear search for a diffuse flux of muon neutrinos with amanda-ii," *Phys. Rev. D* **76** (2007) 042008.

[80] S. Biagi, "Search for a diffuse flux of muon neutrinos with the antares telescope." Seminar at neutrino 2010 athens, greece, 2010.

[81] R. Abbasi *et al.*, "Determination of the atmospheric neutrino flux and searches for new physics with amanda-ii," *Phys. Rev. D* **79** (2009) 102005.

[82] R. Abbasi *et al.*, "The energy spectrum of atmospheric neutrinos between 2 and 200 tev with the amanda-ii detector," *Astropart. Phys.* **34** (2010) 48.

[83] W. Huelsnitz, *Search for Quantum Gravity with IceCube and High-Energy Atmospheric Neutrinos*. PhD thesis, University of Maryland, 2010.

[84] R. Abbasi *et al.*, "Search for neutrino-induced cascades with five years of amanda data." In Preparation, 2010.

[85] M. Ackermann *et al.*, "Search for ultra high energy neutrinos with amanda-iir," *Astrophysical Journal.* **675** (2008) 1014.

[86] R. Abbasi *et al.*, "First search for atmospheric and extraterrestrial neutrino-induced cascades with the icecube detector." In Preparation. To be submitted to Phys. Rev. D, 2010.

[87] S. Grullon, "Searching for high energy diffuse astrophysical muon neutrinos with icecube," in *Proceedings from the Lake Louise Winter Institute*. 2010. arXiv:physics/1005.4962v4.

[88] I. Kravchenko *et al.*, "Rice limits on the diffuse ultrahigh energy neutrino flux," *Phys. Rev. D.* **73** (2006) 082002.

[89] J. Abraham *et al.*, "Limit on the diffuse flux of ultrahigh energy tau neutrinos with the surface detector of the pierre auger observatory," *Phys. Rev. D.* **79** (2009) 102001.

[90] R. Abbasi *et al.*, "An upper limit on the electron-neutrino flux from the hires detector," *Astrophysical Journal* **684** (2008) 790.

[91] P. Gorham *et al.*, "Observational constraints on the ultra-high energy cosmic neutrino flux from the second flight of the anita experiment," *Phys. Rev. D.* **82** (2010) 022004.

[92] R. Abbasi *et al.*, "Search for cosmogenic neutrinos with the icecube neutrino observatory." In Preparation. To be submitted to Phys. Rev. D, 2010.

[93] F. W. Stecker, "Note on high-energy neutrinos from active galactic nuclei," *Phys. Rev. D.* **72** (2005) 107301.

[94] J. B. P. Biermann and W. Rhode, "The diffuse neutrino flux from fr-ii radio galaxies and blazars: A source property based estimate," *Astropart. Phys* **23** (2005) 355.

[95] G. Hill and K. Rawlins, "Unbiased cut selection for optimal upper limits in neutrino detectors: the model rejection potential technique.," *Astropart. Phys* **19** (2003) 393.

[96] R. Ganugapati, *Measurements of Atmospheric Muons Using AMANDA with emphasis on the Prompt Component.* PhD thesis, University of Wisconsin - Madison, 2008.

Appendix A

Event Selection Progression

As discussed in ch. 9, this work followed a blindness procedure which used the burn sample (data taken during June 2008) to establish the final analysis level cuts. The observables used to separate neutrino like events from the down-going muon background events were summarized in ch. 9. A summary of the event selection criteria used to obtain a pure sample of candidate muon neutrino events was given in Table 9.2 and is shown again in Table A.1 for easy reference. The selection cuts were designed to reject the large amounts of down-going atmospheric muons while maximizing the retention efficiency of the simulated E^{-2} astrophysical neutrino flux, which is 35.1% at final purity level. This appendix summarizes the progression of the analysis cuts used to process the data from filter level to the final analysis level. The passing rates after successive purity cuts for data and monte carlo for the down-going atmospheric muon background, atmospheric neutrinos, and a hypothetical astrophysical E^{-2} flux were given in Table 9.3 and are summarized again in Table A.2 for easy reference. Distributions that show the agreement between data and Monte Carlo during each step of the event selection progression are shown in Fig. A.1 to Fig. A.10.

Observable and Selection Criteria
$\theta_{MPE} > 90°$
$\frac{\log(L_{MPE})}{(N_{ch}-5)} < 8$ OR $\frac{\log(L_{MPE})}{(N_{ch}-2.5)} < 7.1$
$\sigma_{MPE} < 3°$
$\log(L_{Bayesian}/L_{SPE32}) > 25$ for $\cos(\theta_{MPE}) < -0.2$
$\log(L_{Bayesian}/L_{SPE32}) > (75\cos(\theta_{MPE}) + 40)$ for $\cos(\theta_{MPE}) > -0.2$
$\log(\frac{L_{Bayesian1}+L_{Bayesian2}}{L_{SPE32}}) > 35$
$\theta_{splittime} > 80°$
$\theta_{splitgeo} > 80°$
$NDir > 5$
$LDir > 240$
$|SDir| < 0.52$

Table A.1: Summary of the analysis level cuts applied to the IceCube data to derive the final event sample for the analysis.

Quality Parameter	Data	Total Atm. μ	Coincident μ	Atm. ν_μ	$E^{-2}\ \nu_\mu$
$\theta_{MPE} > 90°$	19211340	24557460	14318580	7290	100.0%
$\log(L_{MPE})$	675820	365570	89283	3473	69%
σ_{MPE}	114305	83913	32615	2985	50%
$\log(L_{Bayes}/L_{SPE32})$	22981	21842	18920	2195	48.7%
$\log(\frac{L_{Bayes1}+L_{Bayes2}}{L_{SPE32}})$	3550	1925	1436	1490	46.0%
$\theta_{splittime}$	1794	253	188	1284	41.1%
$\theta_{splitgeo}$	1425	94	80	1229	39.3%
$NDir$	1273	61	48	1195	38.7%
$LDir$	1099	43	38	1153	36.9%
$SDir$	1001	0	0	1111	35.1%

Table A.2: Summary of the passing rates for data, atmospheric muon monte carlo, atmospheric neutrino monte carlo, and a hypothetical astrophysical $E^{-2}\ \nu_\mu$ flux after successive applications of purity cuts. The quality parameter for the purity cut is shown; the cut for each quality parameter is defined in Table 9.2. The passing rate for $E^{-2}\ \nu_\mu$ is quoted as a percentage. Adhering to the blindness procedure, the cuts were derived from the 30 day burn sample as discussed in the text.
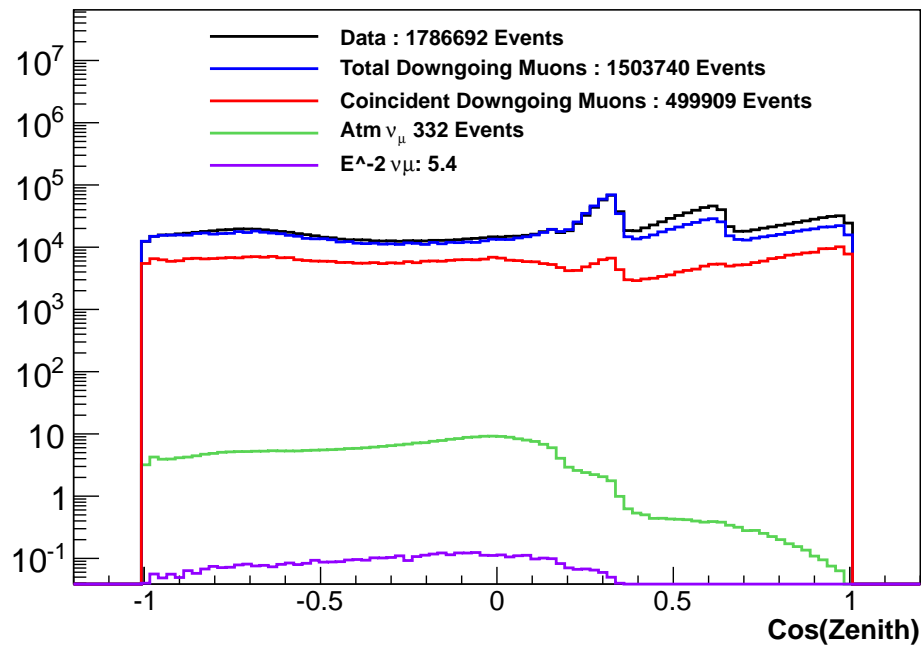
Figure A.1: $\cos(\theta_{MPE})$ distribution comparing data to simulation for one day of Ice-Cube data at filter level. Shown is the total sum of Corsika atmospheric muon simulation from single and coincident atmospheric muons, simulated atmospheric ν_μ, and a hypothetical astrophysical E^{-2} ν_μ flux. A selection of $\theta_{MPE} > 90°$ is made.
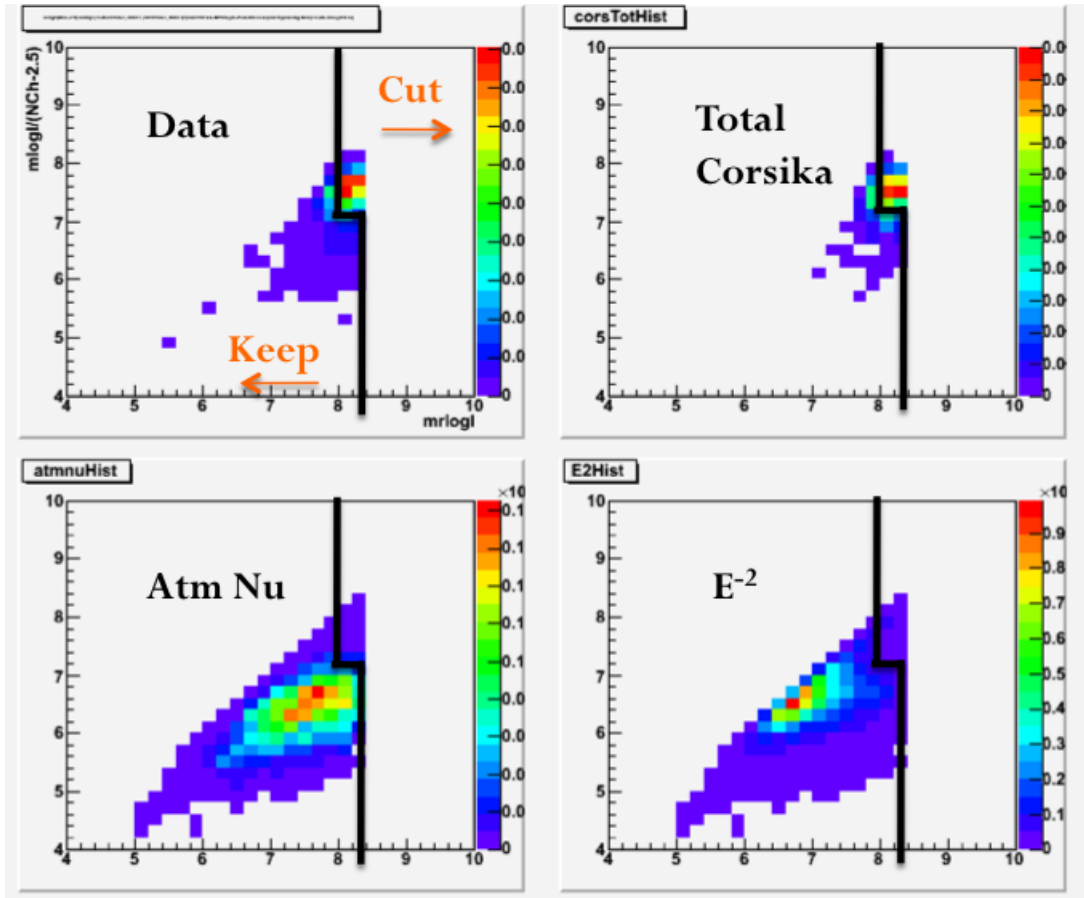
Figure A.2: A two-dimensional cut is made on two different definitions of the reduced log likelihood value of the MPE reconstruction for the IceCube burn sample, which is thirty days of data taken during June 2008. The y-axis shows the redefined reduced log likelihood and the x-axis shows the standard reduced log-likelihood. The selection shown is $\frac{\log(L_{MPE})}{(N_{ch}-5)} < 8$ OR $\frac{\log(L_{MPE})}{(N_{ch}-2.5)} < 7.1$
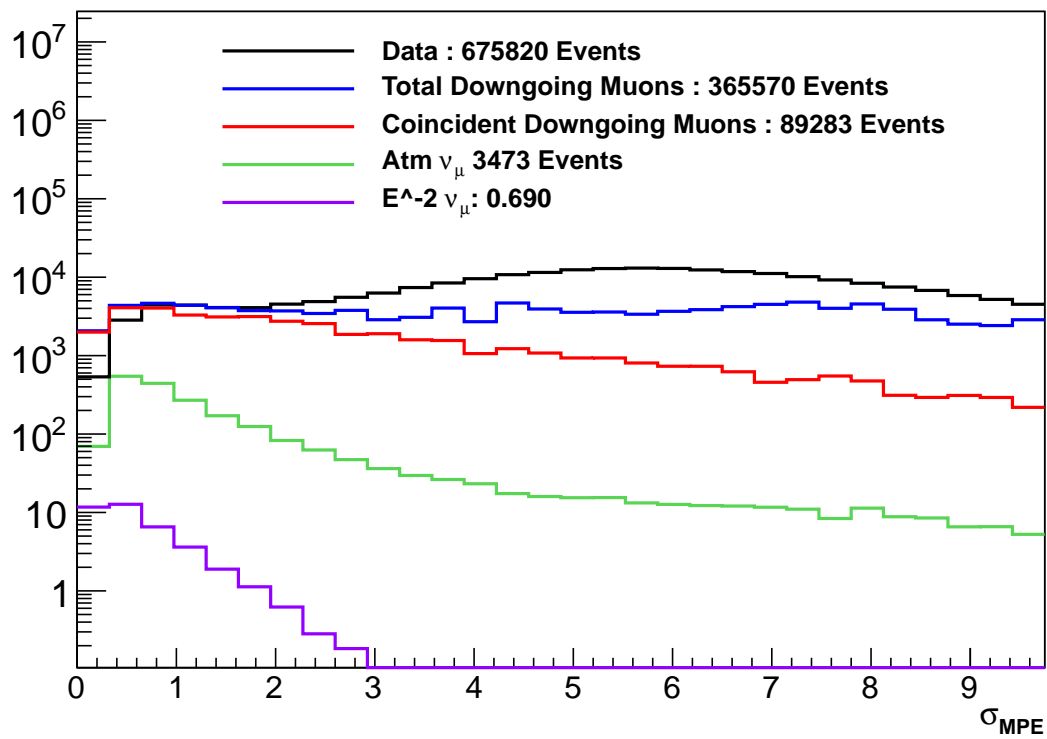
Figure A.3: A cut is made on the paraboloid sigma error estimate of the MPE reconstruction to select well-reconstructed muon tracks. The cut chosen is $\sigma_{MPE} < 3$
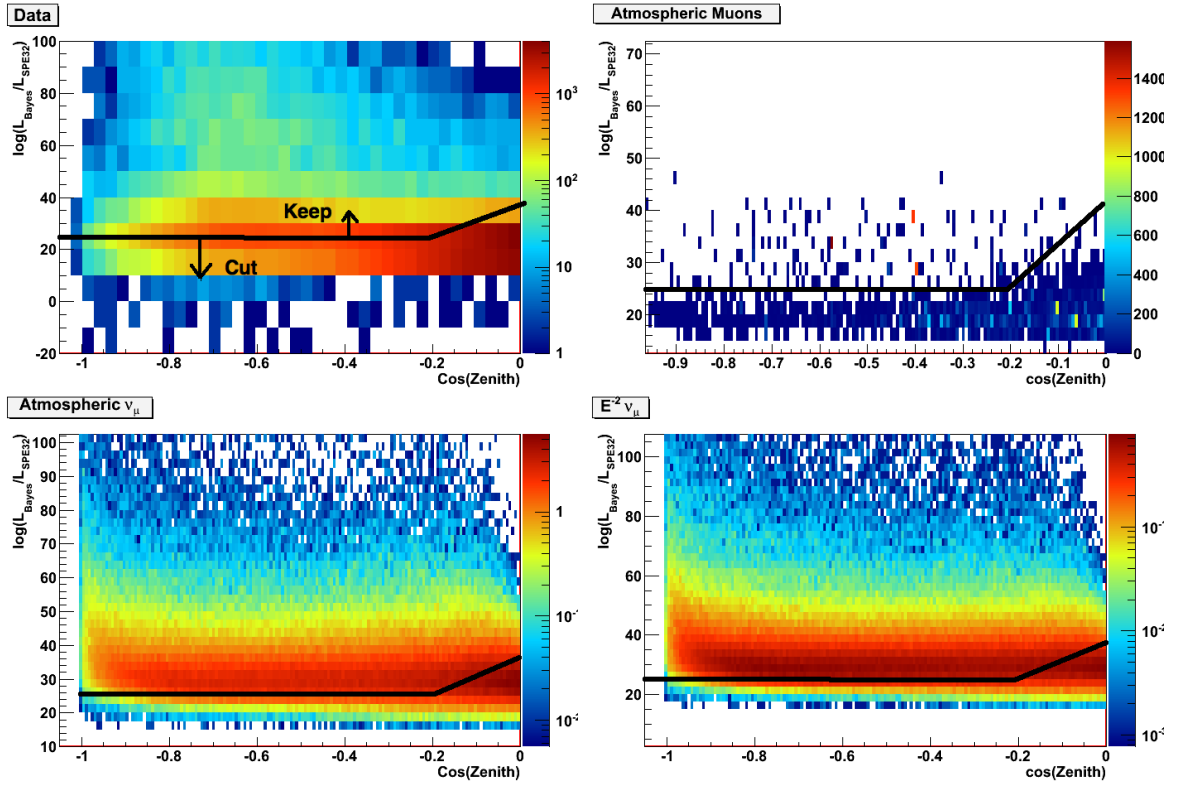
Figure A.4: A two-dimensional cut is made on the Bayesian likelihood ratio test statistic and the zenith angle. A tighter cut on the Bayesian likelihood ratio is needed to reject mis-reconstructed down-going muons near the horizon. The cut chosen is $\log(L_{Bayesian}/L_{SPE32}) > 25$ for $\cos(\theta_{MPE}) < -0.2$ and $\log(L_{Bayesian}/L_{SPE32}) > (75\cos(\theta_{MPE}) + 40)$ for $\cos(\theta_{MPE}) > -0.2$
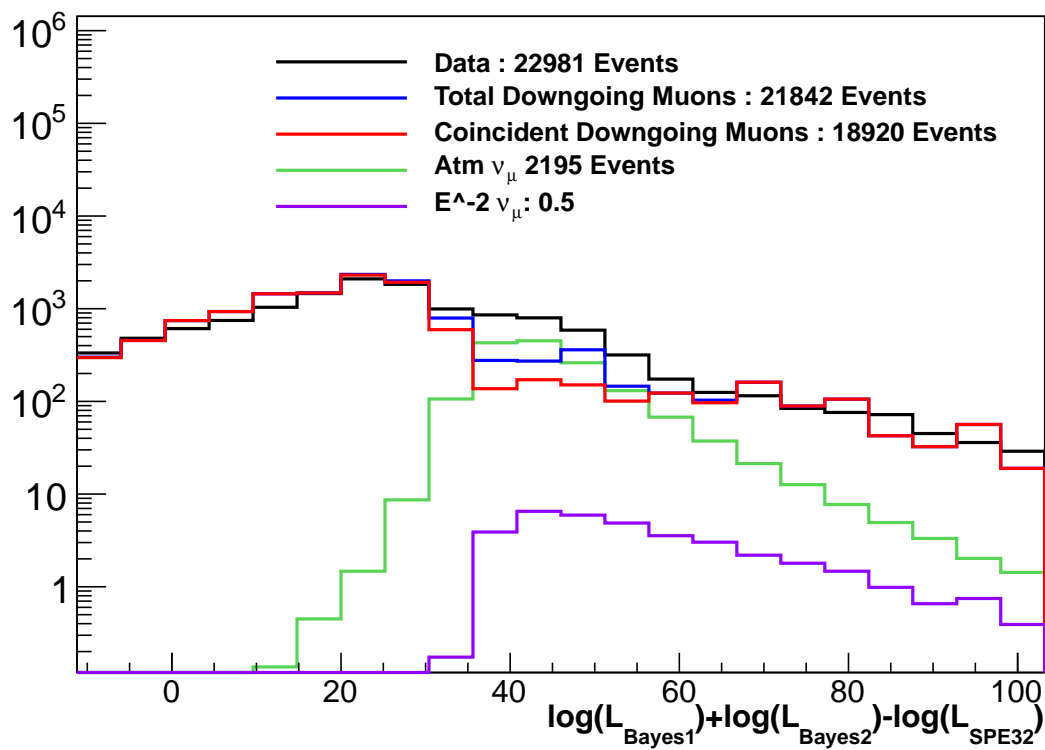
Figure A.5: A cut is made on the split Bayesian likelihood ratio test statistic. This cut is necessary to reject the mis-reconstructed coincident down-going muon background. The cut chosen is $\log(\frac{L_{Bayesian1}+L_{Bayesian2}}{L_{SPE32}}) > 35$
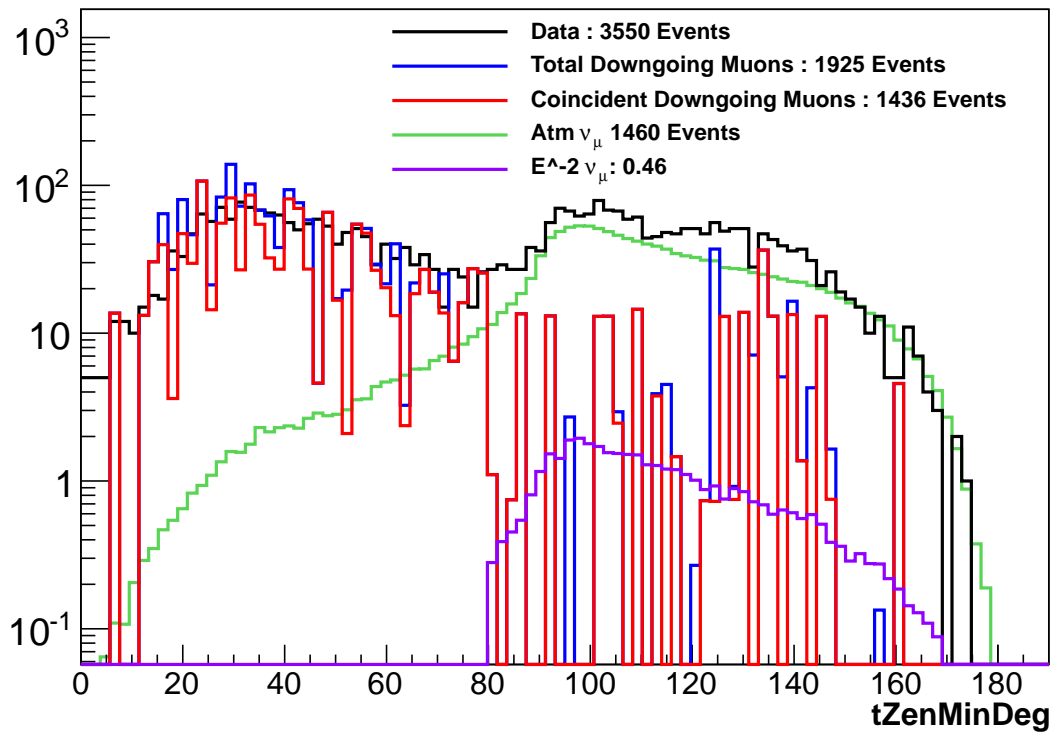
Figure A.6: A cut is made on $\theta_{splittime}$, the minimum zenith angle of a split two muon reconstruction using time splitting . The cut chosen is $\theta_{splittime} > 80°$
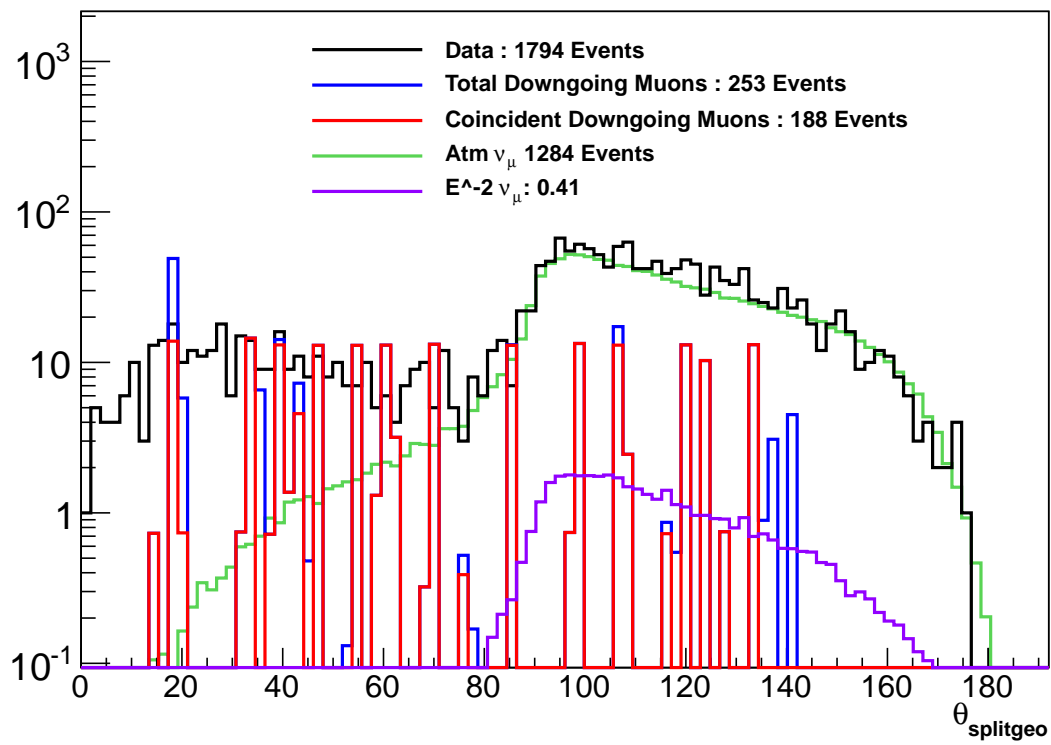
Figure A.7: A cut is made on $\theta_{splitgeo}$, the minimum zenith angle of a split two muon reconstruction using geometry splitting . The cut chosen is $\theta_{splitgeo} > 80°$
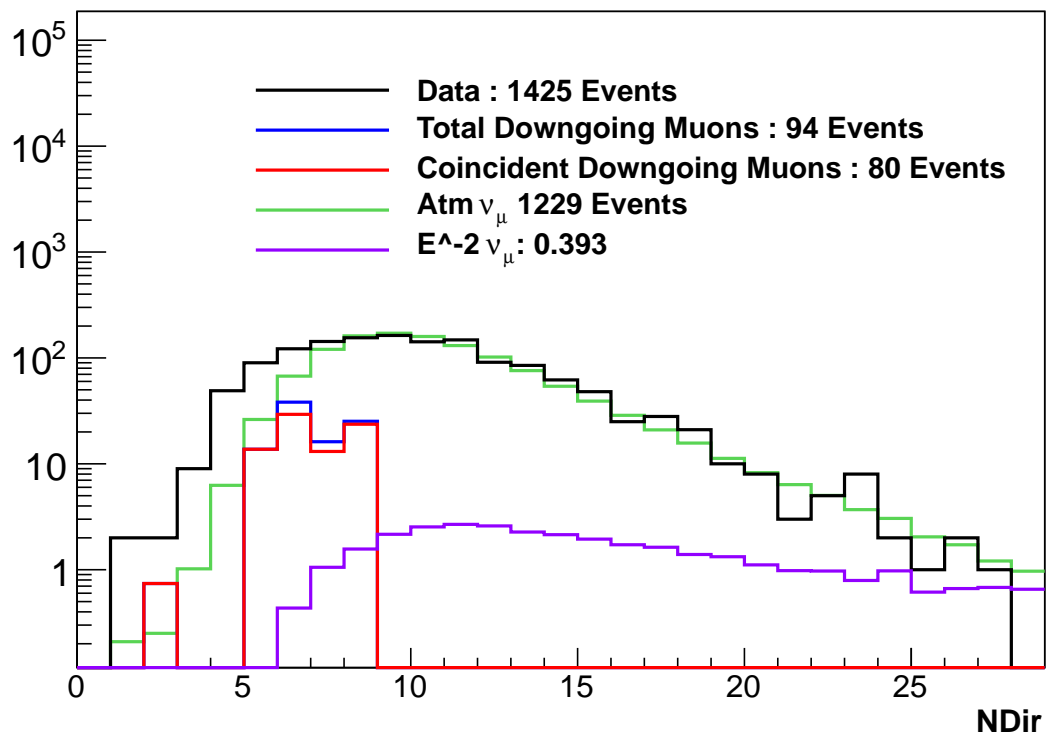
Figure A.8: A cut is made on NDir, the number of direct hits. The cut chosen is $NDir > 5$
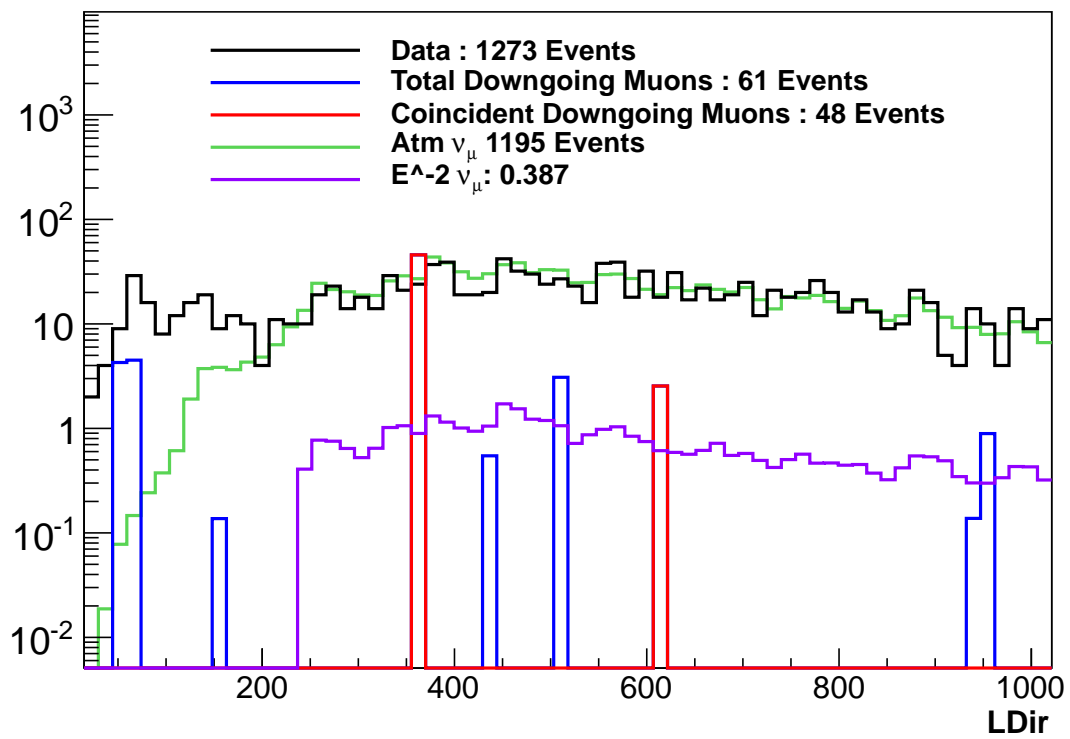
Figure A.9: A cut is made on LDir, the direct length. The cut chosen is $LDir > 240$ meters.
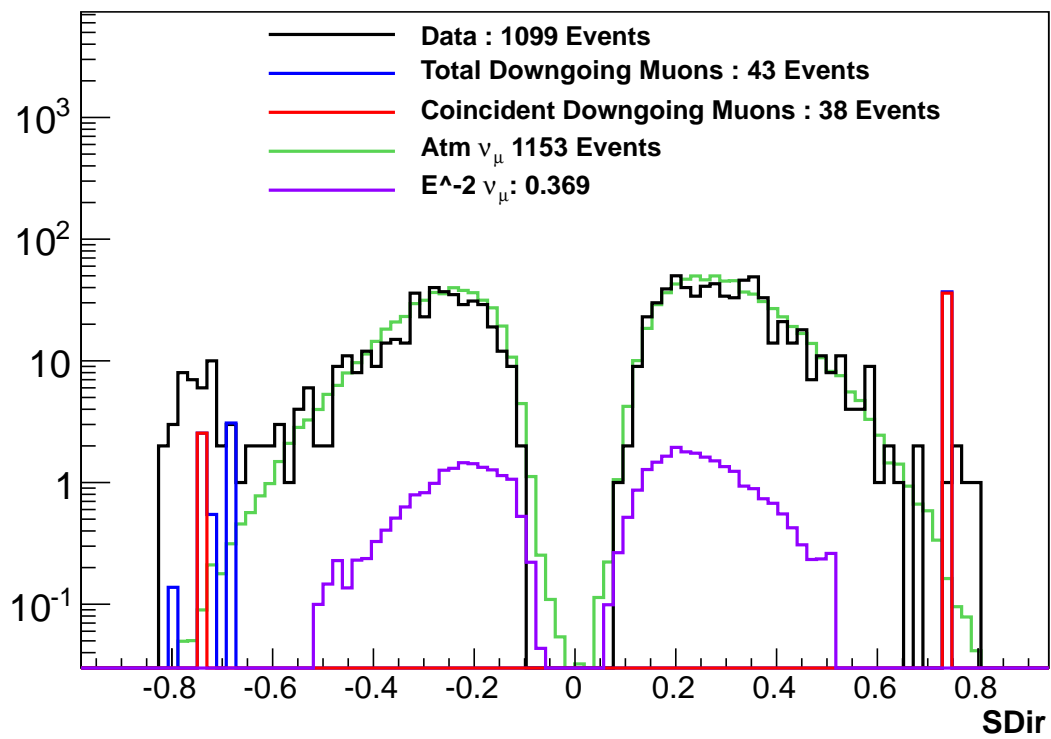
Figure A.10: A cut is made on SDir, the smoothness parameter. The cut chosen is $|SDir| < 0.52$

Appendix B

Candidate Neutrino Event Displays

Table B.1: The four highest energy events in the final analysis sample for the IceCube 40-string data set

dE_{reco}/dX	E_μ	NCh
17.78 GeV/m	88.7 TeV	158
21.41 GeV/m	103.2 TeV	125
22.39 GeV/m	107.1 TeV	206
42.65 GeV/m	185.7 TeV	109

The results of this analysis for the unblinded IceCube 40-string data set is consistent with a background only hypothesis of conventional atmospheric neutrinos. This appendix documents the four highest reconstructed energy events in the final analysis sample for the 40-string data set along with the corresponding event displays demonstrating the topology of these events. Table B.1 lists the four highest dE_{reco}/dX events, the corresponding muon energy, and the number of triggered DOMs. The event displays for these events are shown in Fig. B.1 through Fig. B.4. The timing of the arrival photons in the IceCube event display are represented by a color spectrum with red corresponding to earlier hit times and blue corresponding to later hit times. The MPE (ch. 8) reconstructed muon track is indicated by the red line.
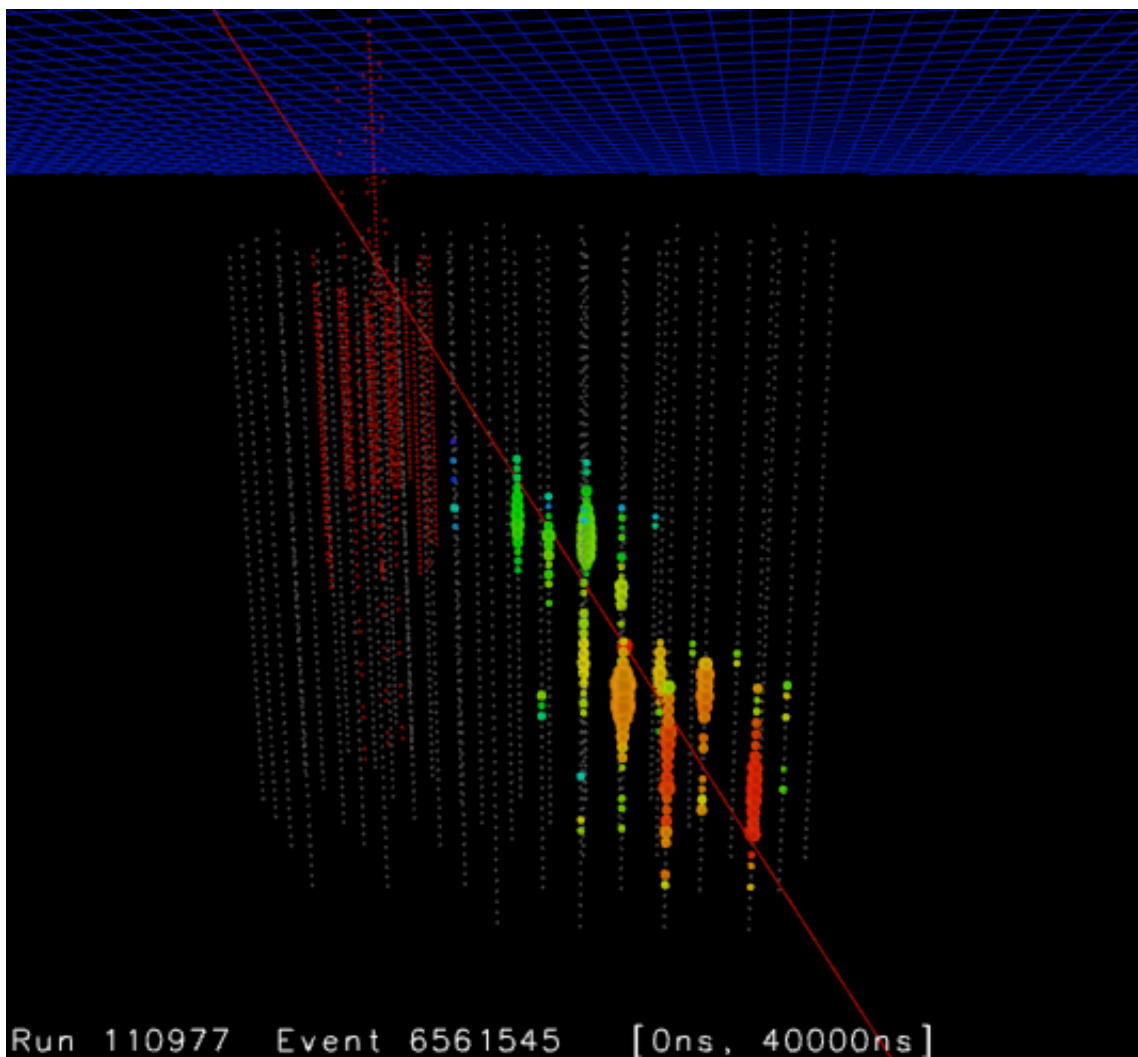
Figure B.1: Event display for a candidate neutrino event in the final IceCube 40-string event sample. The dE_{reco}/dX for this event is 17.78 GeV/m, which corresponds to a muon energy of 88.7 TeV.
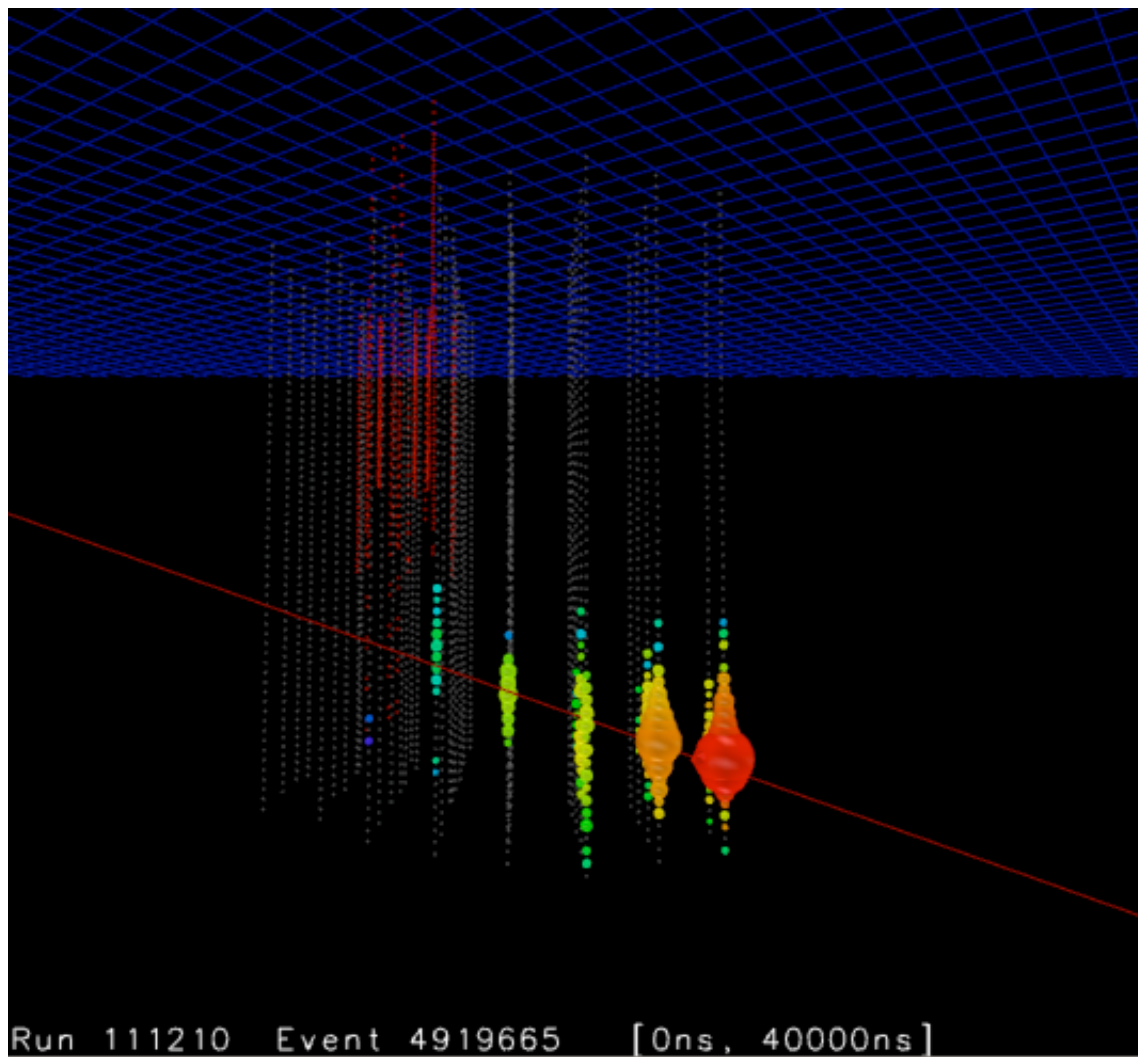
Figure B.2: Event display for a candidate neutrino event in the final IceCube 40-string event sample. The dE_{reco}/dX for this event is 21.4 GeV/m, which corresponds to a muon energy of 103 TeV.
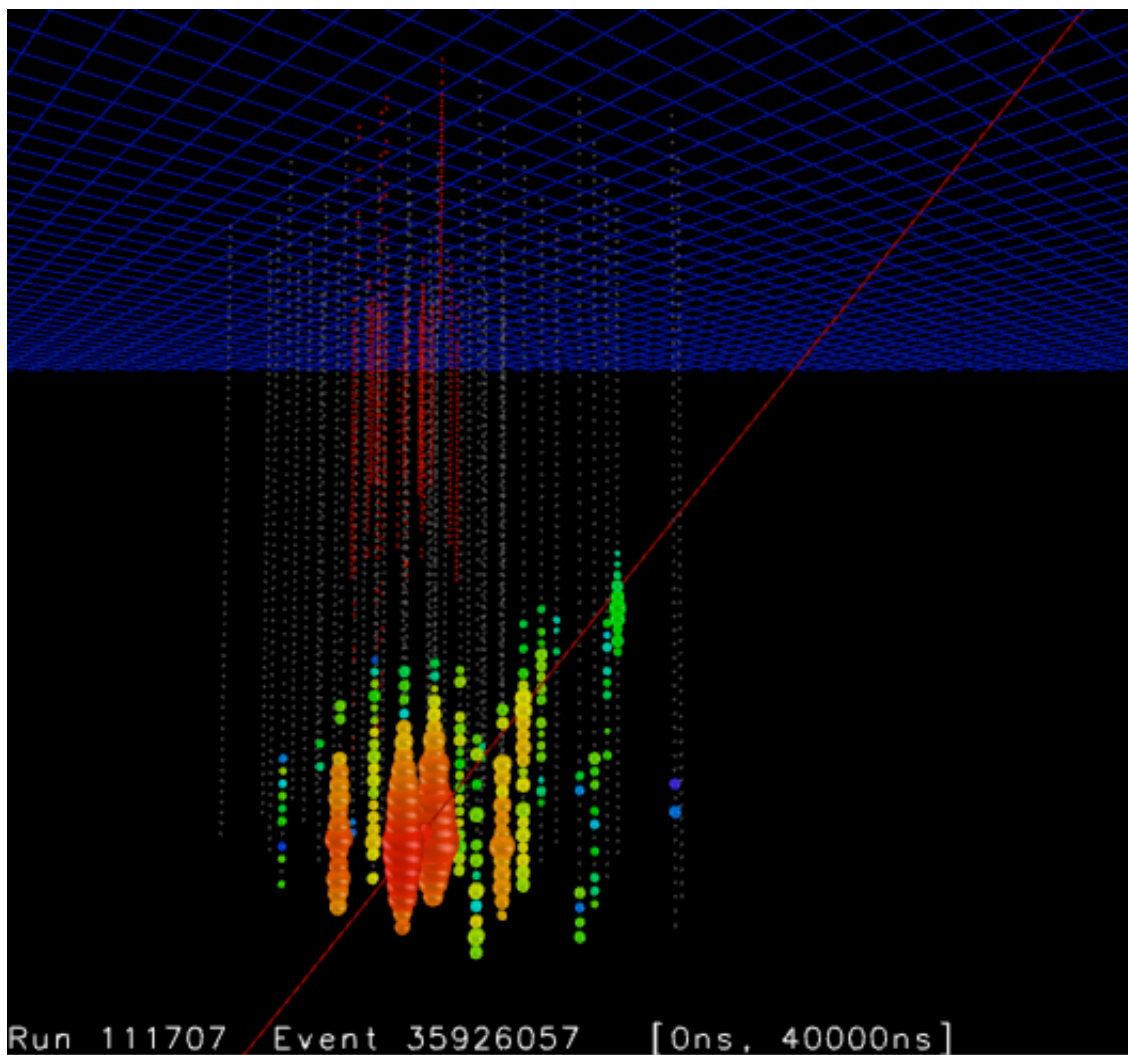
Figure B.3: Event display for a candidate neutrino event in the final IceCube 40-string event sample. The dE_{reco}/dX for this event is 22.39 GeV/m, which corresponds to a muon energy of 107 TeV.
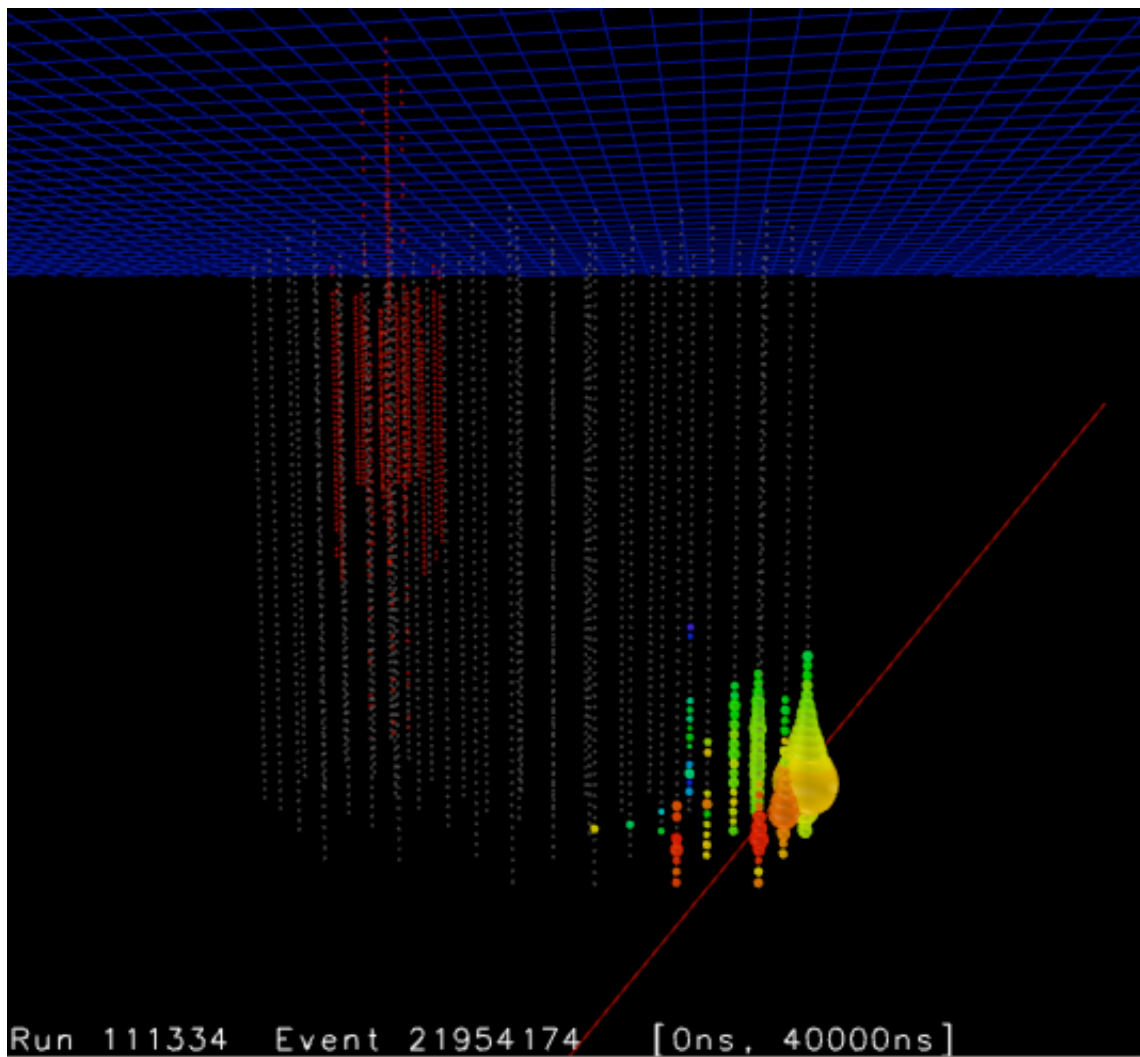
Figure B.4: Event display for a candidate neutrino event in the final IceCube 40-string event sample. The dE_{reco}/dX for this event is 42.65 GeV/m, which corresponds to a muon energy of 185.7 TeV.

Appendix C

Neutrino Effective Area Tables

This appendix has summary tables of the neutrino effective area discussed in Ch. 9 and shown in Fig. 9.11. Table C.1 lists the neutrino effective area in different zenith bands as a function of energy. Table C.2 lists the neutrino effective area over all up-going zenith bands as a function of energy.

Table C.1: Neutrino effective area for $\nu_\mu + \bar{\nu}_\mu$ in different zenith ranges

Energy	A_{eff} (cm^2)	A_{eff} (cm^2)	A_{eff} (cm^2)
$\log_{10}(E_\nu)$ (GeV)	$90° < \theta < 120°$	$120° < \theta < 150°$	$150° < \theta < 180°$
1.87	0.00786	0.0175	0.0316483
2.12	0.651	1.11	1.50653
2.37	8.68	13.9	18.8
2.62	53.2	93.6	125
2.87	227	430	497
3.12	871	1521	1535
3.37	3036	4440	4107
3.62	8967	11343	9990
3.87	23583	27610	19680
4.12	55937	60781	41273
4.37	116966	108570	74411
4.62	233420	188563	98948
4.87	386720	289126	169012
5.12	602700	479723	95173
5.37	1.04×10^6	525077	94141
5.62	1.59×10^6	539513	187518
5.87	2.23×10^6	756785	115723
6.12	2.33×10^6	889516	0
6.37	3.22×10^6	203947	0
6.62	1.68×10^6	415063	0
6.87	3.55×10^6	41212	0
7.12	1.02×10^6	0	0
7.37	8.64×10^6	0	0
7.62	0	0	0
7.87	3.71×10^7	0	0

Table C.2: Neutrino effective area for $\nu_\mu + \bar{\nu}_\mu$ over all zenith ranges

$\log_{10}(E_\nu)$ (GeV)	A_{eff} (cm^2)
1.87	0.0145
2.12	0.935
2.37	11.9
2.62	77.6
2.87	338
3.12	1198
3.37	3693
3.62	9974
3.87	24534
4.12	55745
4.37	108192
4.62	198985
4.87	321831
5.12	489692
5.37	722931
5.62	1.02×10^6
5.87	1.41×10^6
6.12	1.49×10^6
6.37	1.68×10^6
6.62	996327
6.87	1.79×10^6
7.12	509358
7.37	4.32×10^6
7.62	0
7.87	1.85×10^7

Appendix D

Analysis Sensitivity and Astrophysical ν_μ Discovery Potential

Table D.1: Analysis Sensitivity and Astrophysical ν_μ Discovery Potential

Sensitivity	Discovery Potential for $E^{-2}\ \nu_\mu$
$1.22 \times 10^{-8}\ \frac{\text{GeV}}{\text{cm}^2\ \text{s}\ \text{sr}}$	$6.1 \times 10^{-8}\ \frac{\text{GeV}}{\text{cm}^2\ \text{s}\ \text{sr}}$

As discussed in ch. 9, a blindness procedure was followed in order to prevent any inadvertent tuning of the purity cuts that would bias the analysis. The blindness criteria for the IceCube 40-string dataset allowed the use of the burn sample (data taken during June 2008) for the development the analysis level purity cuts. Two important considerations for an analysis to quantify before unblinding the relevant data set is how sensitive the analysis is to the signal flux in question and what the threshold is for a 5σ discovery. This establishes a context for the unblinded results of the analysis.

The sensitivity is defined as the median 90% upper limit obtained over an ensemble of simulated experiments with no true signal. The ability of the analysis to establish a 5σ discovery claim, also known as the *discovery potential*, is defined in this

work to be the strength a hypothetical astrophysical ν_μ flux required to obtain a 5σ discovery in 90% of simulated experiments in the ensemble. As quoted in Ch. 11, the sensitivity of this analysis to a diffuse flux of astrophysical ν_μ with an E^{-2} spectrum is 1.22×10^{-8} $\frac{\text{GeV}}{\text{cm}^2 \text{ s sr}}$ and the E^{-2} discovery potential is 6.1×10^{-8} $\frac{\text{GeV}}{\text{cm}^2 \text{ s sr}}$. These numbers are tabulated in Table D.1 for easy reference.

The procedure used to calculate the sensitivity of this analysis to an astrophysical E^{-2} ν_μ spectrum is outlined below:

- An ensemble of 1000 simulated experiments is performed with no true astrophysical ν_μ signal.

- For each Monte Carlo experiment, a simulated dE_{reco}/dX distribution is reconstructed.

- The profile construction method outlined in ch. 10 is performed on every Monte Carlo experiment in the ensemble.

- The analysis sensitivity is the median 90% upper limit obtained from the ensemble of Monte Carlo experiments.

The discovery potential of the analysis is calculated using a procedure similar to the definition of sensitivity . An ensemble of 1000 simulated experiments is also performed, but instead with an injected flux of astrophysical ν_μ. The discovery potential is the injected flux required for the profile construction method to report a 5σ discovery in at least 900 of the 1000 simulated experiments. The allowed regions for one of these simulated experiments along with the simulated dE_{reco}/dX distribution for the experimental trial are shown in Fig. D.1.
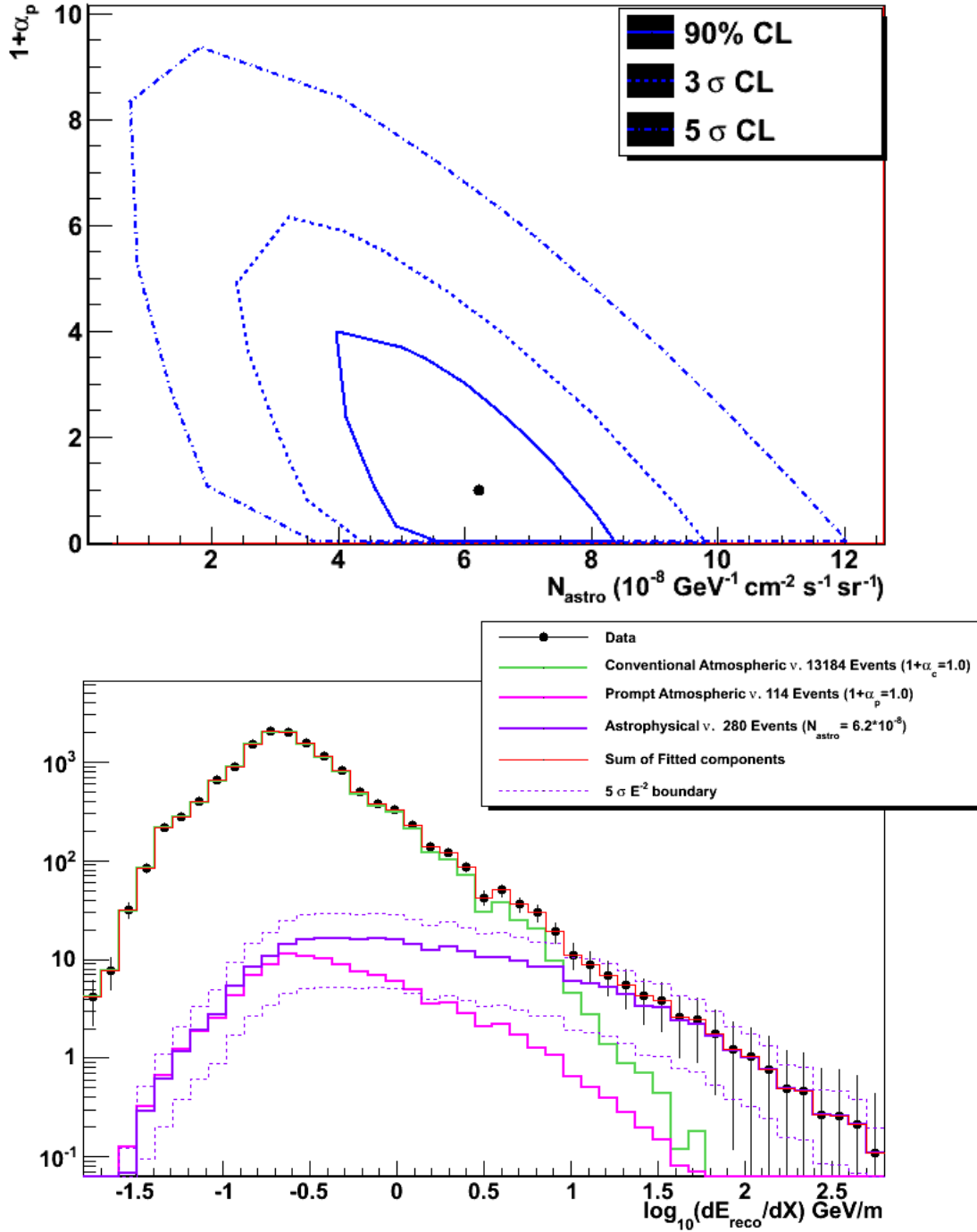
Figure D.1: IceCube 40-string E^{-2} ν_μ discovery potential. The top plot shows an example acceptance region from one of the simulated experiments in a MC ensemble used to calculate the discovery potential flux, which has a normalization of $N = 6.1 \times 10^{-8} \frac{\text{GeV}}{\text{cm}^2 \text{ s sr}}$. The bottom plot shows the dE_{reco}/dX distribution for the simulated experimental trial